Application of the discrete dipole approximation to radiation pressure calculations on dust-aggregates: An exploration

Martijn Frijlink

December 9, 2010

Contents

Chapter 1

Introduction

1.1 Radiation pressure on Interstellar and Circumstellar Matter

An important branch in astrophysics is the study of interstellar and circumstellar matter. The main topics are the study of interstellar and circumstellar nebulae and the formation of planetary bodies from the circumstellar nebulae. Important sources of observational data are the Infrared Space Observatory and the Very Large Telescope. This data is usually analyzed with radiative transfer theory, which assumes the matter making up the nebulae to have certain scattering-properties. These scattering properties depend on the chemistry and the shape of the scattering particles. The properties and dependencies of light scattering particles in general have been and still are subject of investigation, see e.g. [1, 2, 3].

The matter in the nebulae exists of fluffy and porous particles, [4]. These are thought to be aggregates of dust-grains. The formation of these aggregates has until now been studied taking into account merely coagulation, see e.g. [6, 7, 8]. Gravity becomes only important for kilometer-sized objects and is therefore neglected. Radiation pressure calculations on fluffy/porous particles and dust-aggregates have been done, [9, 10, 11, 12]. It is the goal of this research to address the influence of radiation pressure on dust coagulation.

Exact solutions to the problem of light scattering by a particular particle do exist for some mathematically convenient geometries, such as spheres (MIE-theory) and infinitely long cylinders. In 1909 Debye used MIE-theory to calculate radiation pressure on a sphere, [13]. For solving the Maxwell equations for arbitrary geometries, one has to rely on approximative or numerical techniques, see [3] for an extended overview. One such numerical technique for obtaining a solution in the frequency-domain, is the Discrete Dipole Approximation (DDA) [3, 14]; others are the Digitized Green's Function method (DGF), [3, 15], the Volume-Integral Equation Formulation

(VIEF), [3, 16] and the T-matrix method, [3, 17]. The DDA, DGF and VIEF are all discretizations of the integral form of the Maxwell equations, which makes them all examples of the general Method of Moments, [16]. These numerical methods do not require the scattering particle to have any special shape and are therefore well suited for treating dust-aggregates, which in general have a fractal-structure. Here the DDA will be used.

For solutions in the time-domain there is the Finite-Difference Time-Domain method, frequently used in engineering, [18].

1.2 Elastic Light Scattering

Studying elastic light scattering from a particle is done by considering a plane harmonic wave incident on the particle. The behavior of the scattered fields produced by other time-dependent incident radiation, can then afterwards be constructed by Fourier transformation, see Bohren and Huffmann [2]. This book offers a thorough and transparent description of scattering theory and its applications. This paragraph merely resumes chapter 3 of the book.

The grain-diameter d_{grain} for particles of interest is $0.01\,\mu m < d_{grain} < 0.2\,\mu m$, see [5, 19] for grains in the interstellar medium and [20] for grains in the solar system. The wave-length λ of the illuminating stellar light in the interval $0.2\,\mu m < \lambda < 0.8\,\mu m$. These ranges exclude the use of approximate theories like Rayleigh scattering ($\lambda \gg d$) or geometrical optics ($\lambda \ll d$). They even so prohibit Rayleigh-Gans theory, which requires the refractive index m to obey $|m-1| \ll 1$ and $kd|m-1| \approx 1$ with $k = \frac{2\pi}{\lambda}$ the wave-number. Read chapter 5,6 and 7 from [2] for a description of these approximations.

Before any calculations, exact or approximate, can be done, a suitable coordinate system has to be chosen. It is custom to choose the z-direction parallel to the direction of propagation of the incoming wave, see fig 1.1. In this diagram $\hat{e}_x$, $\hat{e}_y$ and $\hat{e}_z$ are the standard Cartesian unit vectors. The angles θ, ϕ together with the unit vectors $\hat{e}_r$, $\hat{e}_\phi$ and $\hat{e}_\theta$ define the standard spherical coordinate-system. For any scattering direction $\hat{e}_r$ the scattering plane is defined by $\hat{e}_r$ and $\hat{e}_z$.

The EM-fields, inside the particle, denoted by subscript 1, as well as outside the particle, subscript 2, must be solutions of the macroscopic Maxwell equations

$$\begin{aligned} \nabla \cdot \vec{E} &= 0, & (1.1)\\ \nabla \cdot \vec{H} &= 0, & (1.2)\\ \nabla \times \vec{E} &= i\omega\mu\vec{H}, & (1.3)\\ \nabla \times \vec{H} &= -i\omega\epsilon\vec{E}. & (1.4) \end{aligned}$$

Figure 1.1: scattering geometry; for an explanation of the symbols, see the text

The boundary-conditions imposed on the particle boundary (with $\hat{n}$ the unit-vector directed outward and normal to the particle surface), are

$$(\vec{E}_1 - \vec{E}_2) \times \hat{n} = 0,$$

$$(\vec{H}_1 - \vec{H}_2) \times \hat{n} = 0.$$

The outside field is the sum of the incident and scattered field;

$$\vec{E}_2 = \vec{E}_{sca} + \vec{E}_{inc} \tag{1.5}$$

$$\vec{H}_2 = \vec{H}_{sca} + \vec{H}_{inc} \tag{1.6}$$

with

$$\vec{E}_{inc}(\vec{r}) = \vec{E}_0 . e^{i(\vec{k}\cdot\vec{r}-\omega t)}$$

$$\vec{H}_{inc} = \hat{k} \times \vec{E}_{inc} \qquad (\hat{k} = \vec{k}/k)$$

The components parallel and perpendicular to the scattering plane of the incoming field, $E_{inc,\parallel}$ and $E_{inc,\perp}$ respectively and the scattered field, $E_{sca,\parallel}$ and $E_{sca,\perp}$ respectively, are related through the amplitude scattering matrix

$$\begin{pmatrix} E_{sca,\parallel} \\ E_{sca,\perp} \end{pmatrix} = \frac{e^{ik(r-z)}}{-ikr} \begin{pmatrix} S_2 & S_3 \\ S_4 & S_1 \end{pmatrix} \begin{pmatrix} E_{inc,\parallel} \\ E_{inc,\perp} \end{pmatrix}. \tag{1.7}$$

Experiments measuring these matrix elements are rather difficult. Experiments measuring the elements of the related Mueller-matrix pose slightly

less problems, [3]. The Mueller-matrix connects the four Stokes-parameters I, Q, U and V of the incoming and the scattered radiation. I is the power of the radiation measured directly by a detector. The other three parameters are constructed by taking the power of the radiation after it has passed through a particular polarizer. Each parameter is the difference in power transmitted by one pair of orthogonal polarizers. The Stokes-parameters of the incoming and scattered wave, collected in so called Stokes-vectors, $\mathbf{s}_{inc}$ and $\mathbf{s}_{sca}$ respectively, are connected through Mueller-matrix M

$$\mathbf{s}_{sca} = M\mathbf{s}_{inc},$$

$$\mathbf{s}_{inc} = \begin{pmatrix} I_{inc} \\ Q_{inc} \\ U_{inc} \\ V_{inc} \end{pmatrix}, \quad \mathbf{s}_{sca} = \begin{pmatrix} I_{sca} \\ Q_{sca} \\ U_{sca} \\ V_{sca} \end{pmatrix}, \quad M = \begin{pmatrix} S_{11} & S_{12} & S_{13} & S_{14} \\ S_{21} & S_{22} & S_{23} & S_{24} \\ S_{31} & S_{32} & S_{33} & S_{34} \\ S_{41} & S_{42} & S_{43} & S_{44} \end{pmatrix}.$$

With $\vec{E}_{sca}$ available, the second step is calculating

- the extinction cross-section C_{ext},
- the absorption cross-section C_{abs},
- the scattering cross-section C_{sca}
- and the asymmetry-parameter g.

The starting point for deriving these quantities is considering the flow of EM-energy across a spherical surface enclosing the particle. The (time-averaged) Poynting-vector on this surface A is

$$\begin{aligned} \vec{S} &= \frac{1}{2}\Re e(\vec{E}_2 \times \vec{H}_2^*) = \vec{S}_{inc} + \vec{S}_{ext} + \vec{S}_{sca} \qquad (1.8) \\ \vec{S}_{inc} &= \frac{1}{2}\Re e(\vec{E}_{inc} \times \vec{H}_{inc}^*) \\ \vec{S}_{ext} &= \frac{1}{2}\Re e(\vec{E}_{inc} \times \vec{H}_s^* + \vec{E}_s \times \vec{H}_{inc}^*) \\ \vec{S}_{sca} &= \frac{1}{2}\Re e(\vec{E}_{sca} \times \vec{H}_{sca}^*) \end{aligned}$$

- $\vec{S}_{inc}$: power inserted by the incoming wave
- $\vec{S}_{ext}$: interaction between scattered and incoming field
- $\vec{S}_{sca}$: power carried out by the scattered field.

Integrating over A one can write

$$\begin{aligned} W_{abs} &= -\int_A \vec{S} \cdot \hat{e}_r dA \qquad (1.9) \\ &= W_{inc} + W_{ext} - W_{sca}, \end{aligned}$$

$$W_{inc} = -\int_A \vec{S}_{inc} \cdot \hat{e}_r dA, \tag{1.10}$$

$$W_{ext} = -\int_A \vec{S}_{ext} \cdot \hat{e}_r dA, \tag{1.11}$$

$$W_{sca} = \int_A \vec{S}_{sca} \cdot \hat{e}_r dA. \tag{1.12}$$

If one assumes the medium surrounding the particle to be non-absorbing, W_{inc} vanishes. The absorption cross section is $C_{abs} \equiv W_{abs}/I_0$, with I_0 the magnitude of $\vec{S}_{inc}$. The expressions for the scattering and extinction cross sections are similar and related through

$$C_{ext} = C_{abs} + C_{sca}. \tag{1.13}$$

For obtaining explicit expressions for the cross sections we assume the incident wave to propagate along the z-axis and to be x-polarized [1]. Furthermore we choose A large enough to be able to use the far field approximations in which the EM-waves are transverse,

$$\vec{E}_{sca} = E_0 \frac{e^{ikr-z}}{-ikr} \vec{X}, \tag{1.14}$$

$$\vec{H}_{sca} = \frac{k}{\mu\omega} \hat{e}_r \times \vec{E}_{sca},$$

with

$$\vec{X} = \Big(S_2 \cos\phi + S_3 \sin\phi\Big)\hat{e}_\theta - \Big(S_4 \cos\phi + S_1 \sin\phi\Big)\hat{e}_\phi, \quad \vec{X} \perp \hat{e}_r$$

Evaluation of (1.11) yields

$$C_{ext} = \frac{4\pi}{k^2} \Re e(\vec{X} \cdot \hat{e}_x)_{\theta=0}. \tag{1.15}$$

Using (1.14) one can rewrite (1.12)

$$\begin{aligned} C_{sca} &= \int_{4\pi} \frac{|\vec{X}|^2}{k^2} d\Omega \\ &= \int_{4\pi} \frac{dC_{sca}}{d\Omega} d\Omega \end{aligned} \tag{1.16}$$

with $dC_{sca}/d\Omega$ the differential scattering cross section. Derived quantities are the phase function or scattering diagram

$$p \equiv \frac{1}{C_{sca}} \frac{dC_{sca}}{d\Omega}$$

[1] the derivations and resulting expressions for y-polarized light are similar; expressions for unpolarized light are obtained by taking the mean

($\int_{4\pi} p d\Omega = 1$) and the asymmetry parameter

$$\vec{g} \equiv \int_{4\pi} d\Omega p \hat{n}. \tag{1.17}$$

(with $\hat{n} = (\sin\theta\cos\phi, \sin\theta\sin\phi, \cos\theta)$) This definition of the asymmetry parameter is taken from Kimura [9] and can be interpreted as the mean direction of the scattered light; the definition given by Bohren and Huffman is just the component along the z-axis. The latter only tells how much light is scattered in the z-direction.

The radiation pressure cross section C_{pr} is composed from three of the above quantities

$$C_{pr} = C_{ext} - < cos\,\theta > C_{sca}. \tag{1.18}$$

This is a measure for the radiation pressure in the direction parallel to $\vec{k}$. This expression was rigorously derived by Debye, [13], for spherical particles by integrating the Maxwell stress-tensor. For an interpretation of (1.18) consider the waves to be streams of photons. The incoming photons transfer an amount of momentum to the particle, proportional to C_{ext}. Part of this momentum leaves the particle, carried away by the scattering photons. The momentum of the photons scattered in the forward direction is proportional to $< cos\,\theta > C_{sca}$. For spherical particles the amount of momentum lost in directions perpendicular to this forward direction is cylindrical symmetrical and therefore amounts to zero; for particles whose scattered field does not exhibit cylindrical symmetry, this cancellation does not occur.

1.3 Discrete Dipole Approximation

This description of the DDA is based on an overview by Draine and Flatau, [14], and a publication by Draine [21]; for more details on DDA I refer to these articles and [3].

In DDA the shape of the scattering particle is approximated by a set of N polarizable volume-elements, with corresponding polarizabilities α_j and electric dipole moments $\vec{P}_j$. The electric and magnetic fields at $\vec{r}_j$, radiated by a dipole at $\vec{r}_l$, when excited by a plane harmonic wave are (omitting $e^{-i\omega t}$)

$$\begin{aligned}
\vec{E}_{jl} &= k^2(\hat{n}_{jl} \times \vec{P}_l) \times \hat{n}_{jl} \frac{e^{ikr_{jl}}}{r_{jl}} \quad + \\
&\quad (3\hat{n}_{jl}(\hat{n}_{jl} \cdot \vec{P}_l) - \vec{P}_l)\left(\frac{1}{r_{jl}^3} - \frac{ik}{r_{jl}^2}\right) e^{ikr_{jl}} \\
&= \mathbf{A}_{jl} \cdot \vec{P}_l, \qquad (1.19) \\
\vec{B}_{jl} &= k^2(\hat{n}_{jl} \times \vec{P}_l)\left(1 - \frac{1}{ikr_{jl}}\right)\frac{e^{ikr_{jl}}}{r_{jl}}, \qquad (1.20)
\end{aligned}$$

with

$$\begin{aligned} \vec{r}_{jl} &= \vec{r}_j - \vec{r}_l \\ \hat{n}_{jl} &= \vec{r}_{jl}/r_{jl} \end{aligned}$$

(see Jackson chapter 9, [22] and Lakhtakia [23]). The complex 3×3 matrix $\mathbf{A}_{jl}$ is commonly refered to as the geometrical factor and has properties $\mathbf{A}_{jl} = \mathbf{A}_{lj} = \mathbf{A}_{jl}^T$. This matrix is ***not*** Hermitian.

The dipole at $\vec{r}_j$, in volume-element j, is excited by the accumulated fields of the scattered radiation due to other dipoles and the incident wave, inducing a dipole moment $\vec{P}_j$. The constant EM-fields in volume j are related to $\vec{P}_l$ by

$$\begin{aligned} \vec{E}_j &= \alpha_j^{-1} \vec{P}_j \\ &= \vec{E}_0 e^{i\vec{k}\cdot\vec{r}_j} + \sum_{j \neq l}^{N} \vec{E}_{jl}, \qquad (1.21) \\ \vec{B}_j &= \vec{B}_0 e^{i\vec{k}\cdot\vec{r}_j} + \sum_{j \neq l}^{N} \vec{B}_{jl}. \qquad (1.22) \end{aligned}$$

Hence finding the N dipole moments $\vec{P}_l$ means solving a system of $3N$ linear, complex equations of $3N$ complex variables. In principle any method for solving a lineair system $A\mathbf{x} = \mathbf{b}$ will do. But the mere size of the (dense) matrix involved in this problem, makes direct methods computationally prohibitive. Therefore iterative methods are much more suitable for doing the job; here a Conjugate Gradient method is used (see [24] for details on the particular CG). First used by DeVoe in 1964 [25], DDA's use was extended by Purcell and Pennypacker by including retardation effects in 1973 [26]. The latter was used here with two computational enhancements :

1. If the polarizable elements are located on a rectangular grid, the matrix-vector product (1.21) is actually a discrete convolution, [27]. Exploiting this feature the $O(N^2)$ complexity for regular matrix-vector products can be reduced to $O(NlogN)$ with Fast Fourier Transformation (FFT).

2. Parallelization of the above FFT-enhanced matrix-vector product, [28].

Also see chapter 2 for a more detailed discussion of these matters.

The various cross sections and asymmetry parameter in terms of the

dipole moments are

$$C_{abs} = \frac{4\pi k}{|\vec{E}_0|^2} \sum_{j=1}^{N} \left\{ \Im m[\vec{P}_j \cdot (\alpha_j^{-1})^* \vec{P}_j^*] - \frac{2}{3} k^3 \vec{P}_j \cdot \vec{P}_j^* \right\}, \quad (1.23)$$

$$C_{ext} = \frac{4\pi k}{|\vec{E}_0|^2} \sum_{j=1}^{N} \Im m[\vec{E}_{inc,j}^* \cdot \vec{P}_j], \quad (1.24)$$

$$\frac{dC_{sca}}{d\Omega} = \frac{k^4}{|\vec{E}_0|^2} \left| \sum_{j=1}^{N} [\vec{P}_j - \hat{n}(\hat{n} \cdot \vec{P}_j)] e^{-ik\hat{n}\cdot\vec{r}_j} \right|^2. \quad (1.25)$$

Expressions for C_{sca} and $\vec{g}$ follow from (1.16) and (1.17) respectively. Furthermore the scattered electric field in the far field regime is given by

$$\vec{E}(\vec{r}) = \frac{k^2\, e^{ikr}}{r} \sum_{j=1}^{N} [\vec{P}_j - \hat{n}(\hat{n} \cdot \vec{P}_j)] e^{-ik\hat{n}\cdot\vec{r}_j}, \quad (1.26)$$
$$\vec{r} = r\hat{n}$$

1.4 Description of research

The following issues will be addressed:

- Earlier work on applying the DDA to radiation pressure calculations by Kimura, [9], and Draine, [29], will be considered. The routine both authors used, based on (1.18), will also be implemented here. An integration routine will be implemented on top of the already existing DDA-code. Test-cases will be spherical particles, allowing for comparison to MIE-calculations. The scattering cross-section will also be calculated by integration and compared to $C_{sca} = C_{ext} - C_{abs}$. This will allow for a separation of the model-error in DDA and the error due to numerical quadrature, and for an

- An alternative algorithm that will arrive at radiation pressure by first calculating the force per dipole will be developed, implemented and tested on the same cases as the integration-routine. Next to the obvious experimental comparison, the two different ways for calculating radiation pressure will be compared theoretically.

- Adaptation of the communication routines, currently implemented in PVM, to MPI making the parallel DDA-code more portable, see e.g. [30, 31] for detailed descriptions of PVM respectively MPI. Next to that, the current FFT-enhanced CG-algorithm only allows for non-absorbing particles to be simulated. This serious restriction will have to be removed before any simulations can be done.

- Finally the available DDA-code will be adapted to do simulations of dust-aggregates. Some example aggregates will be tested and the force-field resulting from the alternative algorithm will be visualized. The shape of the force-field might indicate possible deformations in the dust-aggregate due to the radiation pressure.

Chapter 2

Adapting existing DDA-code to absorbing, inhomogeneous particles

2.1 Introduction

This chapter will focus on two issues. In the next section the translation of PVM-based communication to MPI-based communication will be discussed. The last section of this chapter will deal with the correct use of Fourier Transformation the in matrix-vector products used in the Conjugate Gradient algorithm. But first the use of Fast Fourier Transformations and parallelization in the DDA will be introduced.

The basic DDA-equations (1.21) can be cast into the form

$$\begin{aligned} \vec{\mathbf{E}}_{inc} &= \big(\mathbf{I} - \mathbf{AC}\big)\vec{\mathbf{E}} \\ &= \mathbf{B}\vec{\mathbf{E}}, \end{aligned} \tag{2.1}$$

with $3N$-vectors

$$\begin{aligned} \vec{\mathbf{E}} &= \{\vec{E}_1, \ldots, \vec{E}_N\}, \\ \vec{\mathbf{E}}_{inc} &= \{\vec{E}_{inc,1}, \ldots, \vec{E}_{inc,N}\}, \end{aligned}$$

and $3N \times 3N$-matrices

$$\mathbf{A} = \begin{pmatrix} 0 & \mathbf{A}_{12} & \ldots & \mathbf{A}_{1N} \\ \mathbf{A}_{21} & & \ddots & \vdots \\ \vdots & \ddots & & \mathbf{A}_{(N-1)N} \\ \mathbf{A}_{N1} & \ldots & \mathbf{A}_{N(N-1)} & 0 \end{pmatrix},$$

$$\mathbf{C} = \begin{pmatrix} \boldsymbol{\alpha}_1 & \ldots & 0 \\ \vdots & \ddots & \vdots \\ 0 & \ldots & \boldsymbol{\alpha}_N \end{pmatrix}.$$

It is also assumed that the polarization is isotropic, i.e. $\boldsymbol{\alpha}_j = \alpha_j \mathbf{I}_3$, which makes $\mathbf{C}$ diagonal. The dipole moments follow from $\vec{P}_j = \boldsymbol{\alpha}_j \vec{E}_j$.

If (2.1) is solved with a Conjugate Gradient method, then for each iteration matrix-vector product(s) involving the full matrix $\mathbf{A}$ and $\mathbf{A}^\dagger$ will have to be evaluated. The memory-requirements are $O(N^2)$ and the complexity per iteration is also $O(N^2)$. By locating the dipoles on a rectangular lattice, the matrix-vector product $\mathbf{B}\vec{\mathbf{E}}$ in (2.1) can be formulated as a discrete convolution. Denoting Fourier Transformation in three dimensions by F, the convolutions in $\mathbf{B}\vec{\mathbf{E}}$ can be evaluated by

$$\mathbf{B}\vec{\mathbf{E}} = \vec{\mathbf{E}} - F^{-1}(F(\mathbf{A})F(\mathbf{C}\vec{\mathbf{E}})). \tag{2.2}$$

For non-rectangular particles the coupling constants belonging to lattice-sites not occupied by the particle, are set to zero. This will increase the number dipoles to N_L. Because of the $O(N_L)$ memory-requirements for storing $F(\mathbf{A})$ and specifically the $O(N_L log N_L)$-complexity of FFTs, see [27], this increase will pay off.

Even with FFT, the DDA is limited by both processing speed and memory-use. The bulk of the execution-time is spent on evaluating the matrix-vector products in the iterative solver. Further the memory-use by the DDA is $O(N_L)$ and its accuracy rises with the number of dipoles used to represent the scattering particle, see e.g. [14, 21]. Since with distributed computing the processing speed as well as the amount of memory can be improved, it will increase DDA it's applicability. The actual parallelization is discussed in [28].

2.2 Porting PVM-based communication to MPI-based

The message passing environment P(arallel) V(irtual) M(achine) was introduced in DDA in 1995, [28]. The reason for also implementing the communication-routines of the parallelized DDA-solver with yet another message passing environment, M(essage) P(assing) I(nterface), next to PVM, is the portability and standardization of MPI. MPI was designed to incorporate the best features of earlier message passing communication systems, to allow it's users to parallelize their programs as smoothly as possible, and to be portable.

While replacing PVM-routines with MPI-routines, the standard global-communications of MPI were used as much as possible, but the critical transposition routine, was ported by merely replacing PVM-calls with corresponding MPI-calls. This transposition routine changes the decomposition of the FFT-grid from decomposition in the z-direction into decomposition in the x-direction during each Fourier-transformation and vice versa during each inverse transformation, see [28]. Since these all-to-all communications

take the largest part of the communication time, the port has been done effectively by replacing PVM-calls by their corresponding MPI-calls.

The scalability of the PVM- and MPI-version has been compared in fig.

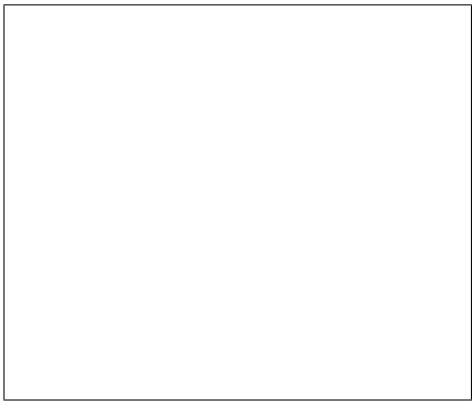

Figure 2.1:

2.1. In this figure the time per iteration is shown as a function of the number of processors and the number of dipoles in the DDA-simulation. These experiments have been performed on a Parsytec CC. MPI clearly shows better performance. This was due to the fact that this particular implementation of MPI buffers its data less than PVM and is therefore no indication to a better performance of MPI in general [1].

2.3 (Re-)enabling DDA to heterogeneous, absorbing particles

The original fast DDA implementation, [28], was not able to produce correct results for absorbing and/or coated spheres. This was caused by an erroneous implementation of multiplication with the hermitian matrix.

The Conjugate Gradient algorithm used for solving the DDA-equations, [24], requires both $\mathbf{B}$ and its hermitian $\mathbf{B}^\dagger$. Using the definition of an hermitian matrix, $\mathbf{B}^\dagger$ expressed in terms of $\mathbf{A}$ and $\mathbf{C}$ is

$$\begin{aligned} \mathbf{B}^\dagger &= \mathbf{I} - (\mathbf{AC})^\dagger, \\ &= \mathbf{I} - \mathbf{C}^\dagger\mathbf{A}^\dagger, \\ &= \mathbf{I} - \mathbf{C}^*\mathbf{A}^*. \end{aligned}$$

The hermitian product, including Fourier Transformation, becomes

$$\mathbf{B}^\dagger\vec{\mathbf{E}} = \vec{\mathbf{E}} - \mathbf{C}^* F^{-1}\Big(F(\mathbf{A}^*)F(\vec{\mathbf{E}})\Big). \tag{2.3}$$

[1] Private communication, F. van der Linde

This formulation of the hermitian product deviates from the one originally implemented

$$(\mathbf{B}^{\dagger}\vec{\mathbf{E}})_{wrong} = \vec{\mathbf{E}} - F^{-1}\Big((F(\mathbf{A})^{*}F(\mathbf{C}\vec{\mathbf{E}})\Big). \tag{2.4}$$

For Fourier-transforms in general the relation

$$F^{*}\Big(f(r)\Big) = F\Big(f^{*}(-r)\Big) \tag{2.5}$$

holds. Since the geometric factor obeys $\mathbf{A}(\vec{r}_j - \vec{r}_l) = \mathbf{A}(\vec{r}_l - \vec{r}_j)$, the identity $F(\mathbf{A}^{*}) = F^{*}(\mathbf{A})$ is valid. For homogeneous, non-absorbing particles (2.4) is therefore equal to (2.3); in that case $\mathbf{C}$ is the unit-matrix in $3N$-dimensional vector-space $\mathbf{I}_{3N}$ times a real number, which makes the complex conjugation of $\mathbf{C} = \mathbf{C}^{*}$ and which makes $\mathbf{C}^{*}$ and $\mathbf{A}^{*}$ commute. For weakly absorbing, homogeneous particles, the complex conjugation of $\mathbf{C}$ in (2.3) does matter, but the deviation from (2.3) is still relatively small, which still permits the CGNR-algorithm to converge, only along a different, longer route through iterant space. For heterogeneous, non-absorbing particles $\mathbf{C}^{*}$ and $\mathbf{A}^{*}$ do not commute. Still, if the refractive indices do not differ to much, the CGNR-algorithm will still converge. This is why the results of a simulation of a concentric sphere with refractive indices $m = 1.02$ and $m = 1.05$ in [28] were in close correspondence to MIE-calculations.

The hermitian multiplication (2.3) is not the one actually implemented. Exploiting the identity $\mathbf{A}^{*}\vec{\mathbf{E}} = (\mathbf{A}\vec{\mathbf{E}}^{*})^{*}$ reduces both memory-use and runtime (one less matrix to initialize).

The radiation pressure calculations for absorbing particles prove this implementation to be correct for homogeneous, absorbing particles, see chapter 4. For heterogeneous particles some coated spheres were simulated and compared to MIE-results (see tables 2.1 and 2.2). The refractive indices of the different layers of the coated spheres were chosen to have clearly distinct, complex values, since this is what the original fast DDA implementation could not deal with. The core and coat radii were chosen arbitrarily. The errors in these cases are appreciable, 5 percent, but acceptable since the refractive index, sphere 1, and size, sphere 2, are in the regime where the DDA is known to experience difficulty.

case	core refr. index	core radius	coat refr. index	coat radius
1	$1.14 + 0.38i$	3.517577	$2.5 + 1.4i$	5.02511
2	$1.33 + 0.01i$	7.039179	$1.81 + 0.48i$	10.05597

Table 2.1: sphere-characteristics

case	$\frac{Q_{ext,DDA}-Q_{ext,MIE}}{Q_{ext,MIE}}$ (perc.)	$\frac{Q_{sca,DDA}-Q_{sca,MIE}}{Q_{sca,MIE}}$ (perc.)
1	3.5	-0.80
2	3.0	5.2

Table 2.2: errors in percents

Chapter 3

Extracting radiation pressure from DDA: Theory

3.1 Introduction

In this chapter an expression will be derived for calculating the radiation pressure in the Discrete Dipole Approximation. This method will calculate the forces per dipole; the total radiation pressure can then be obtained from a trivial summation. This new method will be compared to another method, based on integrating the Poynting vector of the scattered radiation.

Similar to the electro magnetic fields the radiation pressure will be considered as the sum of two parts; one arising from the incoming radiation, $\vec{F}_{inc}$, and the other arising from the scattered radiation, $\vec{F}_{sca}$. $\vec{F}_{inc}$ turns out to be proportional to the extinction cross section C_{ext}. Similar to the scattering cross section there are two methods for determining the scattering force $\vec{F}_{sca}$. One way for obtaining the scattering cross section is (1.16), integrating the irradiated scattered intensity. $\vec{F}_{sca}$ can be obtained similarly by integrating the Poynting vector.

The other method for calculating C_{sca} is equation (1.13). It is preferable for two reasons. It has a lower complexity, two $O(N)$-operations instead of one for each scattering direction, and it will be shown to be the analytical solution to (1.16) [1]. This other method will be called *direct* as opposed to the indirect integration-method, because of the extra quadrature error of the latter. The force and cross section resulting from the direct methods will get the subscript 'd' for direct to distinguish them from integrated values, labeled with subscript 'i'. A direct method for calculating the scattering force does not yet exist and will be derived in this chapter. The analytical

[1] Precisely formulated the numerical value of (1.16) will be shown to converge to the numerical value of (1.13) for rising accuracy of the numerical quadrature

solutions of $\vec{F}_{sca,i}$ and $C_{sca,i}$ will also be shown to be exactly equal to $\vec{F}_{sca,d}$ respectively $C_{sca,d}$. Schematically this theoretical work can be summarized by figure 3.1.

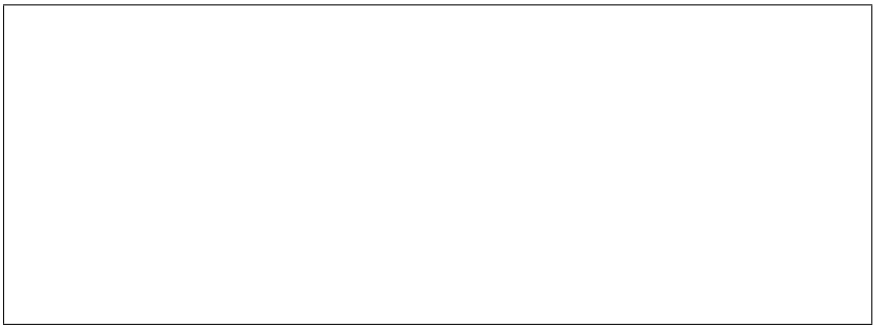

Figure 3.1: transition

3.2 Starting point and previous work

The starting point for the radiation pressure calculations will be the electro-magnetic force on one dipole. As Gordon showed, [32], the force on a dipole j in an electro-magnetic field, $\vec{E}_j = \vec{E}(\vec{r}_j, t)$ and $\vec{B}_j = \vec{B}(\vec{r}_j, t)$, is

$$\vec{F}_j = Re\Big(\vec{P}_j \cdot \nabla_j\Big) Re\Big(\vec{E}_j\Big) \quad + \quad \frac{1}{c} Re\Big(\frac{d\vec{P}_j}{dt}\Big) \times Re\Big(\vec{B}_j\Big). \tag{3.1}$$

If the time-dependence is harmonic, time-averaging of (3.1) leads to

$$< \vec{F}_j >= \frac{1}{2} Re\Big((\vec{P}_j^* \cdot \nabla_j)\vec{E}_j \quad + \quad ik\vec{P}_j^* \times \vec{B}_j\Big). \tag{3.2}$$

See appendix (A.1.1) for a detailed derivation.

Draine [29] proceeded by separating the electric field into two parts

$$\vec{E}_j = \vec{E}_{inc,j} + \vec{E}_{sca,j} \tag{3.3}$$

$$\vec{E}_{inc,j} = \vec{E}_0 e^{i\vec{k}\cdot\vec{r}_j}, \tag{3.4}$$

$$\vec{E}_{sca,j} = \sum_{j \neq l} \vec{E}_{jl}, \tag{3.5}$$

and similar expressions for $\vec{B}_j$; the force per dipole is separated in a similar fashion

$$< \vec{F}_j >=< \vec{F}_{inc,j} > + < \vec{F}_{sca,j} > .$$

The force due to the incoming field $< \vec{F}_{inc,j} >$ is

$$\begin{aligned} < \vec{F}_{inc,j} > &= \frac{1}{2} Re\Big([\vec{P}_j^* \cdot i\vec{k}] \vec{E}_{inc,j} \quad + \quad ik\vec{P}_j^* \times (\hat{k} \times \vec{E}_{inc,j}) \Big), \\ &= \frac{1}{2} Re\Big(i\vec{k} [\vec{P}_j^* \cdot \vec{E}_{inc,j}] \Big), \\ &= \frac{1}{2} \vec{k} Im\Big(\vec{P}_j \cdot \vec{E}_{inc,j}^* \Big); \end{aligned} \tag{3.6}$$

here two the vector-identity

$$\vec{A} \times (\vec{B} \times \vec{C}) = \vec{B}(\vec{A} \cdot \vec{C}) - \vec{C}(\vec{A} \cdot \vec{B}) \tag{3.7}$$

was used. Accumulated for all dipoles and with the substitution of (1.24) this yields (in cgs-units)

$$\begin{aligned} < \vec{F}_{inc} > &= \sum_j < \vec{F}_{inc,j} > \\ &= \frac{1}{8\pi} \quad C_{ext} \quad |\vec{E}_0|^2 \quad \hat{k}, \end{aligned} \tag{3.8}$$

as has already been shown by Draine [29]. The next step will be deriving an expression for the scattering force $< \vec{F}_{sca,j} >$

$$< \vec{F}_{sca,j} > = \frac{1}{2} Re\Big(\vec{P}_j^* \cdot \nabla_j \vec{E}_{sca,j} \quad + \quad ik\vec{P}_j^* \times \vec{B}_{sca,j} \Big). \tag{3.9}$$

Neither Draine nor Kimura, [9], followed this approach, because they were not interested in the force per dipole. Instead they only calculated the total scattering force. For a derivation Draine considered the conservation of momentum. The photons of the incident field result in $< \vec{F}_{inc} >$, while the outgoing photons of the scattered radiation give rise to $< \vec{F}_{out} >$. Using conservation of momentum, the resulting force on the particle $< \vec{F} >$ is therefore

$$< \vec{F} > = < \vec{F}_{inc} > - < \vec{F}_{out} > .$$

Identification leads to $< \vec{F}_{sca,i} > = - < \vec{F}_{out} >$. The (time-averaged) transport of momentum carried out by the scattered radiation, is obtained by integrating the Poynting vector of the scattered field over a the total space-angle

$$\begin{aligned} < \vec{F}_{out} > &= \int_{4\pi} r^2 d\Omega Re\{ \vec{E}_{sca} \times \vec{B}_{sca} \} \\ &= \int_{4\pi} r^2 d\Omega Re\{ \vec{E}_{sca} \times (\hat{n} \times \vec{E}_{sca}) \} \\ &= \frac{k^4}{8\pi} \int_{4\pi} d\Omega \, \hat{n} \Big| \sum_{j=1}^{N} \{ \vec{P}_j - \hat{n}(\hat{n} \cdot \vec{P}_j) \} \, e^{-ik\hat{n} \cdot \vec{r}_j} \Big|^2. \end{aligned} \tag{3.10}$$

This expression was derived by again applying (3.7) and substituting the far field approximation for $\vec{E}_{sca}$ (1.26). The z-component of (3.10) is equal to

$$< F_{out,z} >= -\frac{|\vec{E}_0|^2}{8\pi}\, g_z\, C_{sca},$$

so

$$< F_z >= \frac{|\vec{E}_0|^2}{8\pi} C_{pr}.$$

3.3 Evaluation of the scattering force I: Integrating the Poynting vector of the scattered field

In this section the numerical quadrature of $C_{sca,i}$ and $< \vec{F}_{out} >$ will be discussed. The integral expression for the scattering cross section is

$$C_{sca,i} = \frac{k^4}{|\vec{E}_0|^2} \int_\Omega d\Omega \Big| \sum_{j=1}^{N} \{\vec{P}_j - \hat{n}(\hat{n} \cdot \vec{P}_j)\}\, e^{-ik\hat{n}\cdot\vec{r}_j} \Big|^2. \tag{3.11}$$

The integrand of $< \vec{F}_{out} >$ is the same as the one for $C_{sca,i}$, save for the extra unit vector $\hat{n}$ in the scattering direction. Since the behavior of the extra sines and cosines in $\hat{n}$ is smooth, the integration error for each of the three integrals making up $< \vec{F}_{out} >$, is expected to behave like the error in $C_{sca,i}$.

The integral (3.11) is of the form

$$I = \int_0^\pi d\theta \left[\int_0^{2\pi} d\phi\, f(\phi, \theta) \right]. \tag{3.12}$$

As is suggested by (3.12),the result of the integration in the ϕ-domain will be treated as the integrand for the integration in the θ-domain. Here the Romberg-method will be used for the integration in the ϕ-domain as well as in the ϕ-domain (read *Numerical Recipes in C*, [33] for a detailed description of this and other integration method). It is basically a sophisticated version of the trapezoidal rule,

$$\int_{x_1}^{x_M} dx f(x) \approx h\Big[\frac{1}{2}f_1 + f_2 + \ldots + \frac{1}{2}f_M\Big] \qquad h = \frac{x_M - x_1}{M-1}.$$

A straightforward and efficient way to reaching a certain level of accuracy with this procedure, is making successive estimations with $h \to \frac{h}{2}$ for each new estimation (see fig 3.2). This makes the n'th estimate use $2^n + 1$ points. Convergence is checked for successive estimates s_n and s_{n-1} by testing whether $|s_n - s_{n-1}| < \epsilon$ or not, with ϵ some small constant. The

Figure 3.2: refinement scheme

Romberg-method does not merely use the trapezoidal estimate s_n in the n-th refinement stage, but combines the K previous estimates $s_{n-1}, \ldots, s_{n-K}$ for an estimate to yield error-cancellation.

The book *Numerical Recipes in C* offers a standard routine for calculating one dimensional integrals with the Romberg-method. Both integrations in the θ- as well as in the ϕ-domain are evaluated with this routine, i.e. obtaining one integrand-value for the θ-integration requires one full integration. Some objections/questions can be raised to this rather crude approach.

1. The sampling of the integration intervals is uniform. This might cause trouble with particles whose scattering intensity is strongly peaked in some direction(s); there accurate sampling of the peak-direction(s) might become computationally prohibitive rather soon.

2. This method does not refine the integration-grid simultaneously for both integration-variables.

These (integration) matters will not be addressed here, since there is another, direct method, see section 3.4.

Since a parallelized implementation is used and the dipole moments are distributed, the scattered electric field values will be calculated in advance, allowing the communication for the field-calculations to be done at once. Doing the communication for calculating the field for each direction separately, would mean spending much more time on communication.

3.4 Evaluation of the scattering force II: a direct method

Calculating the scattering force per dipole is more demanding in two respects:

1. the procedure of working out (3.9) is straightforward but of considerable length.
2. The actual computation of $< \vec{F}_{sca,d} >= \sum_{j=1}^{N} < \vec{F}_{sca,j} >$ is $O(N^2)$, whereas (3.10) is $O(N)$. It will be argued that $< \vec{F}_{sca} >$ is a convolution similar to (1.21), thereby reducing the complexity to $O(N \log N)$.

It is convenient to reformulate $\vec{E}_{jl}$, equation (1.19), into

$$\begin{aligned} \vec{E}_{jl} &= e^{ikr_{jl}}\left[(\frac{k^2}{r_{jl}} - \frac{1}{r_{jl}^3} + \frac{ik}{r_{jl}^2})\vec{P}_l + (\frac{3}{r_{jl}^3} - \frac{3ik}{r_{jl}^2} - \frac{k^2}{r_{jl}})\hat{n}_{jl}(\hat{n}_{jl}\cdot\vec{P}_l)\right] \quad (3.13)\\ &= \mathbf{A}_{jl}\cdot\vec{P}_l. \end{aligned}$$

This shows the evaluation of $\vec{P}_j^* \cdot \nabla_j \vec{E}_{jl}$ to consist of four non-trivial differentiations. See appendix A.1.2 for the mathematical details and the resulting expression for $\vec{P}_j^* \cdot \nabla_j \vec{E}_{jl}$.

The magnetic term expressed in dipole moments is

$$\begin{aligned} ik\vec{P}_j^* \times \vec{B}_j &= ik^3 \sum_{l\neq j} \vec{P}_j^* \times \left(\hat{n}_{jl} \times \vec{P}_l\right)\left(1 - \frac{1}{ikr_{jl}}\right)\frac{e^{ikr_{jl}}}{r_{jl}},\\ &= \sum_{l\neq j}(\frac{ik^3}{r_{jl}} - \frac{k^2}{r_{jl}^2})\left((\vec{P}_j^*\cdot\vec{P}_l)\hat{n}_{jl} - (\vec{P}_j^*\cdot\hat{n}_{jl})\vec{P}_l\right)e^{ikr_{jl}} \quad (3.14) \end{aligned}$$

Combining the previous results in this section, $< \vec{F}_{sca,d} >$ can be expressed as

$$\begin{aligned} < \vec{F}_{sca,d} > &= \frac{1}{2}\sum_{j=1}^{N}\sum_{l\neq j} Re\,\vec{G}_{jl} \quad (3.15)\\ \vec{G}_{jl} &= e^{ikr_{jl}}\left[\left((\vec{P}_j^*\cdot\vec{P}_l)\hat{n}_{jl} + \vec{P}_j^*(\hat{n}_{jl}\cdot\vec{P}_l) + (\vec{P}_j^*\cdot\hat{n}_{jl})\vec{P}_l\right.\right.\\ &\quad \left.-5(\vec{P}_j^*\cdot\hat{n}_{jl})\hat{n}_{jl}(\hat{n}_{jl}\cdot\vec{P}_l)\right)\left(\frac{3}{r_{jl}^4} - \frac{3ik}{r_{jl}^3} - \frac{k^2}{r_{jl}^2}\right)\\ &\quad \left.+\left((\vec{P}_j^*\cdot\vec{P}_l)\hat{n}_{jl} - (\vec{P}_j^*\cdot\hat{n}_{jl})\hat{n}_{jl}(\hat{n}_{jl}\cdot\vec{P}_l)\right)\left(\frac{ik^3}{r_{jl}} - \frac{k^2}{r_{jl}^2}\right)\right]. \end{aligned}$$

3.5 Calculating the force per dipole using Fast Fourier Transformations

The computational burden in evaluating $< \vec{F}_{sca,d} >$ comes from the double summation in (3.15). This burden can be relieved by using Fast Fourier Transformation. In order to make this more clear, the complex 3-vector $\vec{G}_{jl}$ in (3.15) is expressed in terms of complex 3×3 matrices

$$\vec{G}_{jl} = \vec{P}_j^* \cdot \mathbf{M}_{jl,m} \cdot \vec{P}_l \, \hat{e}_m. \tag{3.16}$$

(at the right hand side the Einstein summation convention is used).

The complex 3×3 matrices $\mathbf{M}_{jl,m}$ depend only on k and $\vec{r}_{jl}$. They are defined by

$$\begin{aligned}
\mathbf{M}_{jl,m} &= e^{ikr_{jl}} \Bigg[\\
&\quad (\mathbf{U}_{jl,m} + \mathbf{V}_{jl,m} + \mathbf{W}_{jl,m} - 5\mathbf{T}_{jl,m}) \left(\frac{3}{r_{jl}^4} - \frac{3ik}{r_{jl}^3} - \frac{k^2}{r_{jl}^2} \right) \\
&\quad + (\mathbf{U}_{jl,m} - \mathbf{T}_{jl,m}) \left(\frac{ik^3}{r_{jl}} - \frac{k^2}{r_{jl}^2} \right) \Bigg] \qquad (3.17) \\
\mathbf{T}_{jl,m} &= \hat{n}_{jl} \hat{n}_{jl} n_{jl,m} \\
\mathbf{U}_{jl,m} &= \mathbf{1} n_{jl,m} \\
\mathbf{V}_{jl,m} &= \hat{n}_{jl} \vec{\Delta}_m \\
\mathbf{W}_{jl,m} &= \vec{\Delta}_m \hat{n}_{jl}
\end{aligned}$$

with $\Delta_{m,n} = \delta_{mn}$. The m-th column of matrix $\mathbf{V}_{jl,m}$ is $\hat{n}_{jl}$, its other columns contain zeros. Similarly the m-th row of matrix $\mathbf{W}_{jl,m}$ is $\hat{n}_{jl}$ and its other rows contain zeros. Just as the geometrical factors $\mathbf{A}_{jl}$ the matrices $\mathbf{M}_{jl,m}$ are symmetrical. The matrices $\mathbf{T}_{jl,m}$ and $\mathbf{U}_{jl,m}$ are both symmetrical on their own. While $\mathbf{V}_{jl,m}$ and $\mathbf{W}_{jl,m}$ are not, their sum $\mathbf{V}_{jl,m} + \mathbf{W}_{jl,m}$ is symmetrical. Therefore each of the matrices $\mathbf{M}_{jl,m}$ is symmetrical. Contrary to the geometrical factors they are anti-symmetrical in the pair of indices j and l, since the unit vectors $\hat{n}_{jl}$ have odd powers, 1 and 3, whereas in the geometrical factors they have even powers, 0 and 2. Introducing

$$\begin{aligned}
\mathbf{P} &= \{\vec{P}_1, \ldots, \vec{P}_N\} \in \mathbb{C} \\
\mathbf{M}_m &= \begin{pmatrix}
0 & \mathbf{M}_{12,m} & \ldots & \mathbf{M}_{1N,m} \\
\mathbf{M}_{21,m} & \ddots & \ddots & \vdots \\
\vdots & \ddots & \ddots & \mathbf{M}_{N-1,N,m} \\
\mathbf{M}_{N1,m} & \ldots & \mathbf{M}_{N,N-1,m} & 0
\end{pmatrix}
\end{aligned}$$

equation (3.15) can be written as

$$< \vec{F}_{sca,d} >= (\mathbf{P}^* \cdot \mathbf{M}_m \cdot \mathbf{P}) \hat{e}_m \tag{3.18}$$

As an intermediate step the scattering force on dipole j can be calculated by

$$< \vec{F}_{sca,j} >= P^*_{j,n}(\mathbf{M}_m \cdot \mathbf{P})_{3j+n}\hat{e}_m. \tag{3.19}$$

Again the Einstein summation convention is used.

Because the dipoles are arranged in a rectangular grid and their coordinates merely appear in the form $\vec{r}_{jl} = \vec{r}_j - \vec{r}_l$, (3.18) is a discrete convolution. Discrete convolutions can be evaluated with $O(N \log N)$-complexity rather then $O(N^2)$-complexity [27]. Implementing (3.15) with FFT is straightforward, in principle.

3.6 Connecting the integration and direct method

In this section the integrals (3.11) and (3.10) will be solved analytically. First both will be cast into a different form :

$$\begin{aligned} < \vec{F}_{out} > &= \frac{k^4}{8\pi} \sum_{j,l}^{N} \int_{4\pi} d\Omega\, \hat{n}\, I_{jl}(\hat{n}), \qquad (3.20) \\ &= \sum_{j,l}^{N} < \vec{F}_{I,jl} > \\ &= - < \vec{F}_{sca,i} >, \\ C_{sca,i} &= \frac{k^4}{|\vec{E}_0|^2} \sum_{j,l}^{N} \int_{4\pi} d\Omega I_{jl}(\hat{n}) \qquad (3.21) \end{aligned}$$

with

$$\begin{aligned} I_{jl}(\hat{n}) &= \Big(\vec{P}^*_j \cdot \vec{P}_l - (\vec{P}^*_j \cdot \hat{n})(\hat{n} \cdot \vec{P}_l)\Big)\, e^{ik\hat{n}\cdot\vec{r}_{jl}}, \\ \vec{r}_{jl} &= \vec{r}_j - \vec{r}_l. \end{aligned}$$

The reversal of summation and integration is of no concern, since the number of dipoles N is large but finite. The relation

$$\Big| \sum_{j=1}^{N} \{\vec{P}_j - \hat{n}(\hat{n} \cdot \vec{P}_j)\}\, e^{-ik\hat{n}\cdot\vec{r}_j} \Big|^2 = \sum_{j,l}^{N} I_{jl}(\hat{n})$$

follows easily from working out the left hand side; further, one should notice that $I_{jl}(\hat{n}) = I^*_{lj}(\hat{n})$, which will cause the complex parts of each integral-term jl and lj in the double summation to cancel.

The actual evaluation of (3.20) and (3.21) is complicated by the exponential factor

$$exp\Big(ik\hat{n} \cdot \vec{r}_{jl}\Big) = exp\Big(ik(\sin\theta\cos\phi\, r_{jl,x} + \sin\theta\sin\phi\, r_{jl,y} + \cos\theta\, r_{jl,z})\Big),$$

which arises for $j \neq l$. The complexity of the integrals (3.20) and (3.21) can be reduced by considering each integral-term separately and aligning the z-axis for the spherical coordinates parallel to $\vec{r}_{jl}$. This will reduce the complex exponent $ik\hat{n} \cdot \vec{r}_{jl}$ to $ikr_{jl}\cos\theta$. Working out in full detail (3.20) and (3.21) will show that it is possible to separate each term into a θ- and ϕ-dependent factor. The integration of the ϕ-dependent parts is straightforward, the θ-dependent parts need some more attention.

All θ-dependent integrals are of the form

$$\Theta = \int_0^\pi d\theta \sin\theta f(\cos\theta) e^{ikr_{jl}\cos\theta}, \tag{3.22}$$

where f is function of $\cos\theta$. Working out (3.20) and (3.21) in full detail, will also show that only the ϕ-dependent parts, whose corresponding θ-dependent parts have no odd powers of $\sin\theta$, do not vanish. So there is no case where f contains odd powers of $\sqrt{1-\cos^2\theta}$, but only even powers and will therefore merely be a polynomial in $\cos\theta$. This calls for a substitution $t = \cos\theta$, which reduces (3.22) to

$$\Theta = \int_{-1}^{1} dt f(t) e^{ikr_{jl}t} \tag{3.23}$$

The integral

$$I_u(\alpha) = \int_{-1}^{1} dt\, t^u\, e^{i\alpha t} \qquad u \in \mathbb{N}, \alpha \in \mathbb{R},$$

will be solved in appendix A.2.1.

With the above expressions at hand, writing down the solutions to (3.20) and (3.21) is a matter of accurate administration. Similar to previous mathematical details, for this case they will be treated in appendix A.2.2.

First the scattering force will be discussed. Introducing the dummy variables

$$\begin{aligned}
a_{jl} &= e^{ikr_{jl}}, \\
b_{1,jl} &= \tfrac{3}{r_{jl}^4} - \tfrac{3ik}{r_{jl}^3} - \tfrac{k^2}{r_{jl}^2}, \\
b_{2,jl} &= \tfrac{ik^3}{r_{jl}} - \tfrac{k^2}{r_{jl}^2}, \\
\vec{c}_{1,jl} &= \begin{pmatrix} P_{j,x}^* P_{l,z} + P_{j,z}^* P_{l,x} \\ P_{j,y}^* P_{l,z} + P_{j,z}^* P_{l,y} \\ P_{j,x}^* P_{l,x} + P_{j,y}^* P_{l,y} - 2P_{j,z}^* P_{l,z} \end{pmatrix}, \\
\vec{c}_{2,jl} &= (P_{j,x}^* P_{l,x} + P_{j,y}^* P_{l,y})\, \hat{e}_z,
\end{aligned}$$

the integrated scattering force becomes

$$\begin{aligned}
< \vec{F}_{I,jl} > &= \frac{k^4}{8\pi} \int_\Omega d\Omega\, \hat{n}\, I_{jl}(\hat{n}) \\
&= -\frac{1}{2}\Big[Im(a\, b_1) Im(\vec{c}_1) + Im(a\, b_2) Im(\vec{c}_2) \Big]_{jl}.
\end{aligned} \tag{3.24}$$

The imaginary part of $< \vec{F}_{I,jl} >$ has already been omitted; save for being cancelled by the imaginary part of $< \vec{F}_{I,lj} >$, it will not be of any importance in the next steps. After inserting $\hat{n}_{jl} = \hat{e}_z$ in $\vec{G}_{jl}$ in (3.15), the direct scattering force expressed in the same dummy variables is

$$\begin{aligned} < \vec{F}_{jl} > &= \frac{1}{2} Re\, \vec{G}_{jl} \\ &= \frac{1}{2} \sum_{j \neq l} Re(a\, b_1\, \vec{c}_1 + a\, b_2\, \vec{c}_2)_{jl} \\ &= \frac{1}{2} \sum_{j \neq l} \Big[Re(a\, b_1) Re(\vec{c}_1) - Im(a\, b_1) Im(\vec{c}_1) \\ &\quad + Re(a\, b_2) Re(\vec{c}_2) - Im(a\, b_2) Im(\vec{c}_2) \Big]_{jl} . \end{aligned} \tag{3.25}$$

It is clear that

$$- < \vec{F}_{I,jl} > \neq < \vec{F}_{jl} >,$$

but

$$- < \vec{F}_{I,jl} > - < \vec{F}_{I,lj} > = < \vec{F}_{jl} > + < \vec{F}_{lj} > . \tag{3.26}$$

This is true since $\vec{c}_{1,jl} = -\vec{c}^{\,*}_{1,lj}$ and $\vec{c}_{2,jl} = -\vec{c}^{\,*}_{2,lj}$. Therefore $< \vec{F}_{sca,d} >$ and $< \vec{F}_{sca,i} >$ are exactly equal, i.e. the numerical result of the integration method will converge to that of the direct method. At first sight this feature is rather surprising; the direct scattering force uses the full expressions for the electric fields, but the integrated scattering force uses the far field. A starting point for an explanation might be offered by Jackson [22], chapter 9. In his derivation of the scattered field of a single dipole he invoked the far field approximation. This could mean the DDA already is a far field approximation. This idea has not been properly investigated.

The integrated scattering cross section can be treated analogously. With the additional dummy variables

$$\begin{aligned} p_{1,jl} &= \tfrac{k^2}{r_{jl}^2} - \tfrac{ik^3}{r_{jl}} + \tfrac{ik}{r_{jl}^3}, \\ p_{2,jl} &= \tfrac{-3k^2}{r_{jl}^2} + \tfrac{ik^3}{r_{jl}} - \tfrac{3ik}{r_{jl}^3}, \\ q_{1,jl} &= \vec{P}_j^{\,*} \cdot \vec{P}_l, \\ q_{2,jl} &= P^*_{j,z} P_{l,z}. \end{aligned}$$

the integrated scattering cross section becomes

$$C_{I,jl} = \frac{4\pi}{|\vec{E}_0|^2} \begin{cases} \frac{2k^4}{3} |\vec{P}_j|^2 & j = l \\ \Big[Re(a\, p_1) Re(q_1) + Re(a\, p_2) Re(q_2) \Big]_{jl} & j \neq l \end{cases} \tag{3.27}$$

(again the imaginary part of $C_{I,jl}$ has been dropped for $j \neq l$). The direct method for calculating the scattering cross section is

$$\begin{aligned} C_{sca} &= C_{ext} - C_{abs}, \\ &= \frac{4\pi k}{|\vec{E}_0|^2} \sum_{j=1}^{N} \left[Im(\vec{P}_j \cdot \vec{E}^*_{inc,j} - \vec{P}_j (\alpha_j^{-1})^* \vec{P}^*_j) + \frac{2k^3}{3} |\vec{P}_j|^2 \right]. \end{aligned} \tag{3.28}$$

By substituting

$$\begin{aligned} Im(ab^*) &= Re(ia^*b) \\ \vec{E}_{inc,j} - \alpha_j^{-1} \vec{P}_j &= -\textstyle\sum_{l \neq j} \mathbf{A}_{jl} \cdot \vec{P}_l \\ \hat{n}_{jl} &= \hat{e}_z \end{aligned}$$

the direct scattering cross section becomes

$$\begin{aligned} C_{sca} &= \sum_{j,l} C_{jl} \\ C_{jl} &= \frac{4\pi}{|\vec{E}_0|^2} \begin{cases} \frac{2k^4}{3} |\vec{P}_j|^2 & j = l \\ \Big[\begin{array}{l} Re(a\,p_1) Re(q_1) - Im(a\,p_1) Im(q_1) \\ + Re(a\,p_2) Re(q_2) - Im(a\,p_1) Im(q_1) \end{array} \Big]_{jl} & j \neq l \end{cases} \end{aligned} \tag{3.29}$$

Again it is clear that

$$C_{I,jl} \neq C_{jl},$$

but

$$C_{I,jl} + C_{I,lj} = C_{jl} + C_{lj}, \tag{3.30}$$

since $q_{1,jl} = q^*_{1,lj}$ and $q_{2,jl} = q^*_{2,lj}$. Therefore $C_{sca,d}$ and $C_{sca,i}$ are exactly equal, i.e. again the numerical result of the integration method will converge to that of the direct method. This is a rediscovery of work by Markel [34], who used it for an alternative derivation of the absorption cross section. The equality $C_{sca,d} = C_{sca,i}$ is less surprising then $< \vec{F}_{sca,d} >$ and $< \vec{F}_{sca,i} >$, since the expressions for C_{ext}, C_{abs}, and C_{sca} are all derived in the far field approximation.

Although the derivations of both equalities (3.26) and (3.30) are quite similar, their implications are not. In practical computation $< \vec{F}_{sca,i} >$ will always converge to $< \vec{F}_{sca,d} >$ for rising accuracy, even if the set of dipole moments is not the correct solution (or a set of random complex numbers for that matter). But by using (1.21) in (3.29), the correctness of the dipole moments is assumed. This implies that if $C_{sca,i}$ does not converge to $C_{sca,d}$, the set of dipole moments cannot be the correct solution to the DDA-equations. This feature will be used and elaborated in chapter 5.

Chapter 4

Extracting radiation pressure from DDA: simulating spherical particles

4.1 Experimental Setup

Both the integration and direct method have been tested on a number of spherical particles with different size-parameters, $x = \{2.5, 5, 10\}$, and for relative refractive indices m listed in table 4.1. The DDA input-parameters for each case are tabulated in appendix C.1. Due to a lack of time, the

m	material
1.05	Human cells
$1.14 + 0.38i$	H_2O at $10K$ illuminated by $\lambda = 0.1\mu$-radiation
$1.33 + 0.01i$	dirty ice
$1.68 + 0.03i$	Amorphous silicate illuminated by radiation with $0.4\mu < \lambda < 2.0\mu$
$1.7 + 0.156i$	
$1.81 + 0.48i$	H_2O at $10K$ illuminated by $\lambda = 0.15\mu$-radiation
$2.5 + 1.4i$	graphite
$3.05 + 0.33i$	Amorphous silicate illuminated by $\lambda = 90\mu$-radiation

Table 4.1: relative refractive indices

direct method for calculating $\vec{F}_{sca,d}$ has not been implemented with the $O(N \log N)$-complexity FFT suggested in section 3.5, but instead with the direct sumation of $O(N^2)$-complexity. Therefore the application will meet memory-bounds in an earlier stage than when implemented with FFT; the

initially distributed arrays with dipole moments and their coordinates are needed as a whole by each node with the direct method. Compare with the memory overhead in the original parallel DDA implementation.

Before focusing on the radiation pressure related data, the convergence of the CG-method is mentioned, see appendix C.1. Compare the number of iterations needed for the spheres with refractive indices $m_4 = 1.68 + 0.03i$, $m_5 = 1.7 + 0.156i$ and $m_6 = 1.81 + 0.48i$ (for each size-parameter). It seems that while the real parts $Re(m)$ are approximately equal, the number of iterations, needed for convergence, drops with rising $Im(m)$. The DDA-literature does not mention such behavior. This feature will not be investigated here, but its origin should at some point be searched for.

4.2 The integration method

For each case the scattering coefficient and the scattering force were integrated for five different final stages of refinement, $n = \{4, 5, 6, 7, 8\}$. In each case $n_\theta = n_\phi = n$ and $K_\theta = K_\phi = K$ [1] were used. The minimal required rate of convergence was chosen small enough to use all the previously calculated values for the scattered field, $\epsilon = 10^{-9}$. K was set to n, based on the assumption that extrapolation yields the best result when all the available information is used. For each case C_{ext} and C_{abs} were calculated to obtain $C_{sca,d}$. Second $C_{sca,i}$ and $\vec{F}_{sca,i}$ were integrated for each case to all the stages of refinement mentioned above; finally $\vec{F}_{rp,i}$ followed from C_{ext} and $\vec{F}_{sca,i}$. The discussion of $\vec{F}_{sca,d}$ is postponed to the next section.

The following error metrics are calculated as a function of n for each case, and plotted in appendix B.1 :

- The integrated scattering efficiency extracted from DDA compared to values generated by MIE-code [2].

$$\epsilon(Q_{sca})_{MIE} = \big[(Q_{sca,i})_{DDA} \quad - \quad (Q_{sca})_{MIE}\big]/(Q_{sca})_{MIE}$$

- Comparison of the integrated and the direct scattering efficiency $Q_{sca,i}$ and $Q_{sca,d}$. This is an internal check that can be done independently from the particle-shape and composition. It is therefore an important test for the quality of values resulting from simulations of scattering particles whose analytical solutions are not known, see the discussion in section 5.2.3. Next to that it is a means for testing the accuracy of the integration algorithm.

$$\epsilon(Q_{sca})_{DDA} = \big[Q_{sca,i,DDA} \quad - \quad Q_{sca,d,DDA}\big]/Q_{sca,d,DDA}$$

[1] see section 3.3 for the meaning of K

[2] All MIE-values were generated by the algorithm published in [2]. Although MIE-theory is formally exact, actual numbers resulting from MIE-theory can only be approximate, since the formal solutions are all infinite expansions.

- Comparison of $F_{sca,i,z}$ extracted from DDA compared to values generated by MIE-code.

$$\epsilon(F_{sca})_{MIE} = \big[\frac{8\pi F_{sca,i,z,DDA}}{\vec{E}^2_{inc}\pi a^2_{eff}} \quad - \quad (gQ_{sca})_{MIE}\big]/(gQ_{sca})_{MIE}$$

  a_{eff} is the radius of the equivalent volume sphere with a volume $V = N\,V_{dip}$.

- Comparison of $F_{rp,i,z}$ extracted from DDA compared to values generated by MIE-code.

$$\epsilon(F_{rp})_{MIE} = \big[Q_{ext,DDA} - \frac{8\pi F_{sca,i,z,DDA}}{\vec{E}^2_{inc}\pi a^2_{eff}} \quad - \quad Q_{pr,MIE}\big]/Q_{pr,MIE}$$

- In the case of a spherical particle, the fraction

$$\epsilon(F_{rp})_i = \big[\sqrt{F^2_{rp,i,x,DDA} + F^2_{rp,i,y,DDA}}\big]/F_{rp,i,z,DDA}$$

  is a means for testing the accuracy of the integration algorithm and the DDA, since $F_{rp,x,MIE} = F_{rp,y,MIE} = 0$.

In fig. 4.1 these fractions are plotted for the case of $m = 1.14 + 0.38i$ and $x = 5$. Similar plots for the other cases are printed in appendix B.1. In

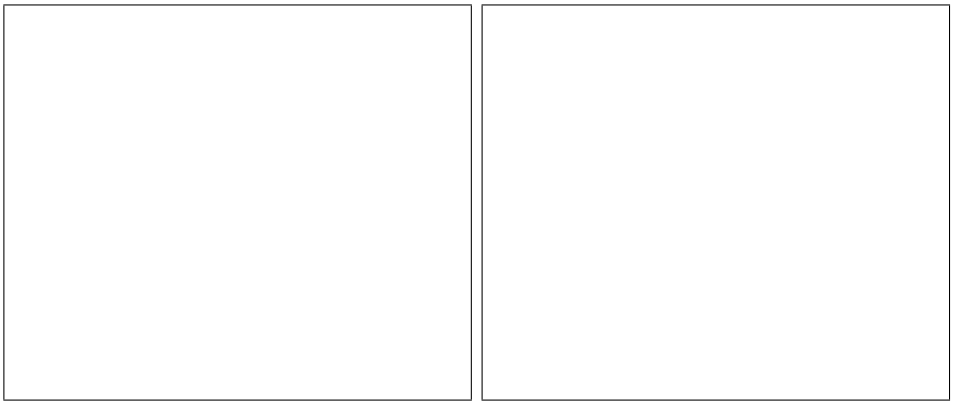

Figure 4.1: Fractional errors for $m = 1.14 + 0.38i$ and $x = 5$

appendices B.2 and B.3 the measured quantities are plotted as a function of the real and imaginary part of the relative refractive index respectively for a more complete overview. They also contain plots of the MIE-errors in Q_{ext} and Q_{abs}.

Fig. 4.1 is exemplary for the other cases, in the sense that it confirms two expectations about the integration procedure. First, the integrated scattering cross section is expected to converge to the direct scattering cross section

for rising n, i.e. $\epsilon(Q_{sca})_{DDA} \to 0$, see section 3.6. The plots of $\epsilon(Q_{sca})_{DDA}$ for each case firmly confirm this expectation. Second, due to likeness of the integrands in (3.11) and (3.10) the behavior of $\epsilon(F_{sca})_{MIE}$ is expected to be similar to $\epsilon(Q_{sca})_{MIE}$. It can be said that for all cases the observed behavior of $\epsilon(F_{sca})_{MIE}$ is much more flat than $\epsilon(Q_{sca})_{MIE}$'s and that $\epsilon(F_{sca})_{MIE}$ (hardly) changes for $n = (6, 7, 8)$ (possibly the factor $\cos\theta$ makes the integrand more smooth). Still, the behavior of $\epsilon(F_{sca})_{MIE}$ tends to exhibit the same irregularities, ($x = 10$), and curvature, ($x = 2.5$ and $x = 5$), for lower n.

By comparing the MIE-errors in Q_{ext} and $F_{rp,z,i}$, appendices B.2.1 and B.2.5 respectively, it can be concluded that these errors are of the same order for $n = 6$, which corresponds to roughly $2^{2n} \approx 4.0e3$ integration points. Further refinement of the integration grid does not result in more accurate values for $F_{sca,z,i}$, i.e. $(g_z C_{sca})_i$, and therefore not of $F_{rp,z}$. As can be expected the accuracy grows worse for coarse integration grids, even so that for $n = 4$ a significant number of values are totally unacceptable, therefore the result for $n = 4$ are not plotted in the graphs. See for example the value of $(g_z C_{sca})_i$ for the particles ($x = 10, m = 1.05$) and ($x = 10, m = 1.33+0.01i$).

From the plots of $\epsilon(F_{sca})_{MIE}$ and $\epsilon(F_{rp})_{MIE}$ in B.2.4 and B.2.5 respectively, one can observe a tendency for the MIE-errors to rise with larger m and at the same time to drop for rising x. The former tendency of rising errors for larger $|m|$ is a common feature of DDA. The latter can be explained from the difference in shape between the real sphere and its counterpart in the DDA-simulation. In the simulations above the number of dipoles per wavelength was kept constant for each refractive index. Therefore the number of dipoles in the spherical particle is $N_{dip} \propto x^3$, see appendix C.1, so for larger x the shape of simulated sphere is closer to the shape of the real sphere. This behavior was first described and explained by Draine [21].

The difference between the values of $(g_x C_{sca})_i$ and $(g_y C_{sca})_i$ for each case is striking. The value of $(g_y C_{sca})_i$ remains at a (roughly) constant, low value (typically of order 10^{-7}) for rising n. $(g_x C_{sca})_i$ starts at an absolute value 5 percent of $(g_z C_{sca})_i$ for $n = 4$ and decays slowly. The only difference between the two is in their integrands; for $(g_x C_{sca})_i$ a factor $\sin\theta\cos\phi$ is added to the differential scattering cross section, for $(g_x C_{sca})_i$ a factor $\sin\theta\sin\phi$. A last remark concerning the integration method is made on the behavior of the ratio $\epsilon(F_{rp})_i$ [3] plotted as a function of $Im(m)$, see appendix B.3.6; for non-absorbing spheres this ratio is > 10 percent for $n = 5$ ($n = 4$ even worse), while for absorbing spheres $\epsilon(F_{rp})_i$ is 2 percent when $n = 5$. These two observations concerning the components perpendicular to the direction of the incident beam, will not be investigated any further here (studying the differential scatttering cross section would be the first step). The direct method for calculating the scattering force offers a fruitfull alternative to

[3] De facto this comes down to the ratio $F_{sca,x,i}/F_{rp,z,i}$

the integration method.

4.3 The direct method

The direct method for evaluating the scattering force (3.15) was shown to be the exact solution to (3.10). In table 4.2 the results of the $O(N^2)$-implementation of (3.15) are compared to those obtained by numerical quadrature to the highest accuracy ($n = 8$) of (3.10) and MIE-results. Although not all cases could be simulated with the direct method, the results in table 4.2 can be considered a firm numerical confirmation of the final results of section 3.6, as is the behavior of the ratio $\epsilon(Q_{sca})_{DDA}$, see appendix B.2.3. Also notice that both the $(g_y C_{sca})_d$ and $(g_x C_{sca})_d$ are of the same order as $(g_y C_{sca})_i$. Since the direct method delivers more information, i.e. the forces per dipole, and it is the exact solution of the integral in the the integration method, the direct method is preferable from a modeling point .

When comparing execution time the $O(N^2)$ direct method is no match for the integration method. For the case $(x = 5, m = 1.14 + 0.38i)$ executed on a single workstation, the execution of the direct $O(N^2)$ method took 22 min to complete, whereas the integration method finished in 6 min ($n = 6$). Both timings include the runtime for the DDA-kernel of about 2.5 minutes. Clearly the direct method needs to be optimalized before it can be seriously useful.

A rough estimate for the execution time of the direct method with FFT-optimalization can be extracted by considering the profiling of the DDA-kernel. The initialization time for the Fourier transformed matrix $\mathbf{A}$ (see chapter 2) and the time per CG-iteration were both 8 seconds. Assuming

- the initialization time for each of the matrices $\mathbf{M}_x$, $\mathbf{M}_y$ and $\mathbf{M}_z$ in (3.18) is equal to that for $\mathbf{A}$,
- each iteration is dominated by the two matrix vector products involved,
- the execution time for the FFT-enhanced direct method is determined by the three matrix initializations and three matrix vector products,

the execution time for obtaining the radiation pressure per dipole on the $(x = 5, m = 1.14 + 0.38i)$-sphere will probably be about $40\,s$. The FFT-optimized direct method should definitely be implemented for two reasons.

1. It yields more information,
2. Even if the execution time for the direct method, estimated above, is too optimistic, it will likely be less than for the integration method.

x	m	$-f_{z,MIE}$	$-f_{z,d}$	$-f_{z,i}$	$C_{pr,MIE}$	$C_{pr,d}$	$C_{pr,i}$
2.5	1.05	0.371524	0.371659	0.37166	0.122651	0.122112	0.12211
	1.14+0.38i	8.24625	8.27892	8.27892	26.9337	26.9879	26.9879
	1.33+0.01i	16.7049	16.6745	16.6745	8.64969	8.53591	8.53591
	1.68+0.03i	52.2132	53.1363	53.1363	30.6572	30.0432	30.0432
	1.7+0.156i	33.7644	35.0417	35.0417	35.8229	35.8576	35.8576
	1.81+0.48i	20.9415	21.8652	21.8652	38.626	39.307	39.307
	2.5+1.4i	18.9673	20.1332	20.1332	38.489494	39.8698	39.8698
	3.05+0.33i	21.3637	23.0295	23.0296	37.605915	38.3417	38.3417
5	1.05	8.57554	8.57815	8.57815	0.859150	0.863781	0.86379
	1.14+0.38i	63.8590	63.7802	63.7802	105.156	105.065	105.065
	1.33+0.01i	222.436	223.542	223.542	53.8230	53.4137	53.4134
	1.68+0.03i	60.2681	62.5525	62.5525	112.658	111.251	111.251
	1.7+0.156i	73.1439	73.6662	73.6662	127.300	127.694	127.694
	1.81+0.48i	83.2464	84.2083	84.2083	123.102	124.179	124.179
	2.5+1.4i	87.5410	88.88566	88.8856	121.662	123.694	123.694
10	1.05	150.276	150.258	150.258	4.656049	4.66638	4.66626
	1.14+0.38i	315.490	315.302	315.302	384.379	384.237	384.236
	1.33+0.01i	438.904	441.835	441.835	262.641	263.107	263.106

x	m	$-f_{x,d}$	$-f_{x,i}$	$-f_{y,d}$	$-f_{y,i}$
2.5	1.05	3.1e-09	0.0018	1.7e-09	1.6e-09
	1.14+0.38i	-2.1e-08	0.036	8.6e-08	2.9e-08
	1.33+0.01i	6.3e-07	0.071	-1.9e-07	2.7e-07
	1.68+0.03i	1.8e-06	0.18	1.4e-06	2.4e-06
	1.7+0.156i	9.3e-07	0.12	-2.6e-07	1.8e-06
	1.81+0.48i	1.0e-06	0.079	1.9e-06	8.3e-07
	2.5+1.4i	-1.3e-06	0.092	2.4e-06	8.6e-07
	3.05+0.33i	3.9e-06	0.095	-3.5e-06	3.1e-07
5	1.05	6.5e-08	0.017	3.7e-08	2.0e-08
	1.14+0.38i	3.2e-08	0.14	1.6e-06	1.2e-06
	1.33+0.01i	1.6e-05	0.45	9.8e-06	1.0e-05
	1.68+0.03i	4.9e-06	0.30	8.0e-06	1.1e-05
	1.7+0.156i	3.7e-07	0.17	2.7e-06	1.4e-06
	1.81+0.48i	6.1e-07	0.20	6.72e-07	-1.8e-07
	2.5+1.4i	-4.7e-06	0.29	-1.1e-05	-1.9e-07
10	1.05	1.2e-06	0.15	6.1e-07	7.1e-07
	1.14+0.38i	-4.6e-06	0.43	3.5e-06	-3.4e-06
	1.33+0.01i	1.0e-04	1.1	9.1e-05	7.8e-05

Table 4.2: $\vec{f} = \vec{g} C_{sca}$ and C_{pr}

Finally some pictures of the forces per dipole are shown, see figures 4.2, 4.3 and 4.4. In these figures only bisections of the spheres along the yz-plane are

Figure 4.2: Force per dipole for the sphere $m = 1.05, x = 2.5$

displayed, the forces in the other halves are mirror images of the displayed halves. In all three cases the largest forces occur on the interface between sphere and medium. From [21, 36] it is known that the largest errors in the internal field occur exactly on this interface. The question whether these errors in the internal field are transferred to the force per dipole at the same place, can be answered by comparing the forces per dipole to the force field resulting from MIE-theory. Probably the work of Debye [13] can be helpfull in accomplishing this.

Figure 4.3: Force per dipole for the sphere $m = 1.33 + 0.01i, x = 2.5$

Figure 4.4: Force per dipole for the sphere $m = 1.14 + 0.38i, x = 2.5$

Chapter 5

Radiation pressure calculations on aggregate particles: preliminary results

5.1 Introduction

A quick glance at the title of this MsC thesis might suggest that it is primarily devoted to aggregate particles. As is often the case with first impressions, this one is deceiving. While previous chapters dealt with spherical particles, chapter 4, or no specific geometry at all, chapters 2 and 3, only this one will specifically consider DDA-based radiation pressure calculations on aggregate particles.

The primary aim of this chapter is to consider the behavior and validity of the DDA when applying it to fluffy and/or aggregate particles. It is with this idea in mind that some simulations have been performed and will be discussed. The literature investigation at the end of this chapter will also focus on this subject.

5.2 Applying the DDA to light scattering by aggregate particles

5.2.1 Experimental setup

Because of its general and flexible nature, several different implementations of the DDA exist. There is no conclusive argument for determining the best; this strongly depends on the problem being considered. The implementation used here determines the coupling constants from the relative

refractive index by the Lattice Dispersion Relation (LDR) [37], instead of the classic Clausius-Mossoti relation. It uses the Conjugate Gradient Normal Residue method to solve the linear system of equations, describing the electric field inside the particle. By arranging the dipoles on a rectangular grid, the matrix-vector products can (and will) be evaluated with Fast Fourier Transformation.

A dust particle is modeled by an aggregate of spherical grains. Besides by the coordinates of these grains, the aggregate is characterized by

- λ :
  wavelength,
- $m_g(\lambda)$:
  relative refractive index belonging to λ, for the constituting material of grain g,
- $r_{grain,g}$:
  radius of grain g,
- d_{box} :
  side length of the cubic box circumscribing the aggregate. A quick and easy estimate for d_{box} is

$$\begin{aligned} d_{box} &= 2\max(r_{i,x,max} - r_{i,x,min}, r_{i,y,max} - r_{i,y,min}, r_{i,z,max} - r_{i,z,min}) \\ & \quad i \in \{1, \ldots, N_{grain}\} \end{aligned}$$

From now on all grains are taken to be identical. The mapping of the grains on the dipole grid is determined by four parameters.

1. D_{grain} :
   Number of dipoles per grain. Here D_{grain} will be set to one (this will also be discussed in 5.2.2).
2. d_{dip} :
   Dipole-spacing.
3. $D_\lambda = \frac{\lambda}{d_{dip}\, Re(m)}$:
   Number of dipoles per wavelength. This parameter is not directly involved in mapping the grains to the dipoles, but it is crucial in the discretization of wave-phenomena; for accurate discretization of the internal field, one should take $D_\lambda > 10$, read [21, 37, 14, 38].
4. D_L :
   side length of the dipole-lattice circumscribing the aggregate.

The iteration of the CGNR-procedure is continued, as long as

$$\frac{(\mathbf{I}-\mathbf{AC})\vec{\mathbf{E}}-\vec{\mathbf{E}}_{inc}}{\vec{\mathbf{E}}_{inc}} > \epsilon_0$$

where ϵ_0 is called the stop-criterium.

The center of the dipole representing the grain is selected to be as close as possible to the original grain-center. It is clear that if the grid is too coarse, i.e. the dipole-spacing is too large, this can lead to several grains being represented by one dipole. This is prevented in the presented simulations by monitoring the number of grains in the projected aggregate.

The above quantities are related through

$$D_{grain}d_{dip}^3 = \frac{4\pi}{3}r_{grain}^3, \quad (5.1)$$

(equivalent volume sphere)

$$D_\lambda = \frac{\lambda}{d_{dip}\,Re(m)} \geq 10, \quad (5.2)$$

$$D_L = \left\lceil \frac{d_{box}}{d_{dip}} \right\rceil. \quad (5.3)$$

Inserting (5.1) in (5.2) yields

$$D_\lambda = \left(\frac{3D_{grain}}{4\pi}\right)^{1/3} \frac{\lambda}{r_{grain}} \frac{1}{Re(m)} \geq 10. \quad (5.4)$$

Two different aggregates were considered. Both were supplied by Carsten Dominik, who uses bigger versions of these aggregates to study dust-coagulation in interstellar clouds [6, 7, 8]. Aggregate 1 was made up of 51 grains (see figure 5.1 to get an idea of its structure) and aggregate 2 of 101 grains, all grains having a radius $r_{grain} = 0.1\mu m$. Both aggregates were simulated with $m_a = 1.14 + 0.38i$ and $m_b = 1.7 + 0.03i$. The latter corresponds to amorphous silicate illuminated by $0.25\mu m < \lambda < 2\mu m$, which the aggregates were originally modeled after. The reason for also using the former m_a, actually corresponding to ice at $10K$, was simply not to restrict the simulations to

Figure 5.1: Aggregate 1,51 grains

weakly absorbing material. In all cases $\lambda = 0.8\mu m$ was used.

$$\begin{aligned} d_{dip} &= 0.16(D_{grain})^{-1/3}\mu m, \\ d_{box,1} &= 1.6\mu m, \\ d_{box,2} &= 3.4\mu m, \\ D_{\lambda,a} &= 4.4(D_{grain})^{1/3}, \\ D_{\lambda,b} &= 2.9(D_{grain})^{1/3}, \\ D_{L,1} &= \left\lceil 9.85(D_{grain})^{1/3} \right\rceil, \\ D_{L,2} &= \left\lceil 20.76(D_{grain})^{1/3} \right\rceil, \\ \epsilon_0 &= 10^{-12}. \end{aligned}$$

For $D_{grain} = 1$, D_λ clearly disobeys $D_\lambda > 10$. The same simulations have therefore also been done with the grain-size as well as the grain-coordinates rescaled with factors $f = 0.5$ and $f = 0.25$, increasing $D_{\lambda,a}$ to 8.7 and 17.4 respectively, and $D_{\lambda,b}$ to 5.8 and 11.7 respectively. This mounts up to twelve different aggregates.

5.2.2 Objections

As has already been said the main objective of this chapter is to explore the behavior and the validity of the DDA in the realm of fluffy/aggregate

particles. For this reason the DDA was used in its standard configuration, CG-FFT with the Lattice Dispersion Relation for setting the polarizabilities, while in the discussion of the results, directions for possible improvements will be given.

Before considering the actual results, several objections can be raised to using the standard configuration of the DDA. First of all, the DDA in general is known to make the largest errors on the interface, the boundary between the scattering material and the medium, see e.g. [21]. Using only one dipole per grain, all dipoles will be on the interface, so one should be cautious while interpreting the resulting data. Second, the use of the LDR is not justified, since this way for calculating the coupling constant was derived assuming $\lambda \gg d_{dip}$, [37]; a demand that is not satisfied in these simulations. Kimura resolved this issue by replacing the LDR with the a1-term method proposed by Okamoto [39]. This method derives the polarizability of each monomer from MIE-theory. A similar method has been proposed by Dungey and Bohren [40].

Furthermore representing the aggregate on a rectangular grid, can be criticized from two points of view. From a modeling point of view one can raise the point of deformation; the simulated aggregate is one whose grains are slightly shifted from the original grain-centers. How will this affect the scattered and internal field ? The answer to this question is terra incognita. The fraction of the total number of sites N on the cubic grid belonging to the vacuum, i.e. voids, might become so large that the gridless $O(N_{non-void}^2)$ algorithm is going to be faster than the $O(N \log N)$ Fast Fourier Transform. The rigorous approach for the latter issue will be reintroducing the $O(N_{non-void}^2)$ method for matrix-vector multiplication and simply compare the execution times to the $O(N \log N)$. Here merely a complexity-analysis of matrix-vector multiplication with both methods will be done, thereby deriving a crude method for comparing execution time for the $O(N \log N)$-method and the $O(N_{non-void}^2)$-method. Let us denote the number of Flops (floating point operations) for the $O(N \log N)$-implementation by v_{grid} and for the $O(N_{grain}^2)$-implementation by $v_{gridless}$. First $v_{gridless}$ will be calculated. Matrix vector multiplication of a complex $3N_{non-void} \times 3N_{non-void}$-matrix and a complex $3N_{non-void}$-vector takes $9N_{non-void}^2$ complex scalar multiplications and $3N_{non-void}(3N_{non-void} - 1)$ complex scalar additions, which mounts up to $v_{gridless} \approx 72N_{non-void}^2$ Flops [1].

It is stated, that a Fast Fourier Transform of a linear array of l complex numbers takes $(2l)\log(2l)$ two-point Fourier Transforms (see [33] for a clear description of FFT and [27] for its implementation in the DDA). Furthermore it is stated, that one two-point Fourier Transform consists of one complex scalar multiplication and one complex scalar addition, i.e. 8

[1] 1 complex scalar multiplication = 4 real multiplications + 2 real additions → 6 Flops; 1 complex scalar addition = 2 real additions → 2 Flops

Flops. With the assumptions below, v_{grid} will be estimated:

- The rectangular grid is cubic and the side length of the cube is a power of 2, i.e. $\sqrt[3]{N} = N_x = N_y = N_z = l = 2^a, a \in \mathbb{N}$.
- The Fourier transformed interaction matrix is stored in memory, as are the trigonometric function values used in each FFT.
- The operation-count of the bit-reversal immediately preceding the actual transformation can be neglected (an array of length l involves at most $l/2$ exchanges of array-elements; this will be assumed to be overruled by the operation-count of the actual transformation itself).

The complex 3D FFT of a 3-vector field on the cubic grid takes $v_{grid} = 3\times3\times 8\times(2l)^2\times(2l)\log(2l) = 4.48N(3+\log N)$ Flops [2]. In the Fourier domain the convolution will take $8N\times(9\,complex\,multiplications+6\,complex\,additions) = 48.11NFlops$. One FFT, one convolution in the Fourier domain, and one inverse FFT mount up to $v_{grid} = 48N(35+8\log N)Flops$.

Bearing in mind the curve in figure 5.2 represents the equality $v_{grid} =$

Figure 5.2: FFT complexity comparison

$v_{gridless}$, the interpretation of this figure should be as follows. For a particle discretized with $N_{non-void}$ dipoles, which needs a cubic grid with N sites to facilitate FFT, the gridless $O(N^2_{non-void})$ is more efficient if the point with coordinates $(N, N_{non-void})$ lies below the curve describing $v_{grid} = v_{gridless}$ and vice versa. This idealized approach should not be applied too rigorously since

1. the Temperton FFT-algorithm, which is used here, does not demand the sides of the grid to be a power of two but allows for array-lengths that can be factorized into powers of two, three and five,

[2] Here log means $^2\log$

2. and the bit-reversal operation is not included.

But from the positions of the aggregates 1 and 2 in figure 5.2 one can still conclude that both will most likely be better off with $O(N^2_{non-void})$ matrix vector multiplication.

5.2.3 Simulation results

The light scattering simulations for each of the twelve different aggregates, were conducted with both X- and Y-polarized incident light. The behavior of the residue convergence, differences between direct and integrated scattering cross section, and direct and integrated scattering force were similar for both the X- and Y-polarization. Therefore only the results for Y-polarization have been included here.

Alas the behavior of the residue convergence and the differences between direct and integrated scattering cross section are not yet trustworthy. First of all did the residues for aggregate 2 with refractive index m_a not converge, for none of the three rescaling-factors 1, 0.5 and 0.25, as did the simulation of aggregate 2 with m_b and rescaling-factor 1 (see the convergence-schemes in appendix E). Furthermore, the comparison of the integrated and direct scattering cross section is not positive either. The comparison of the direct and integrated scattering force does yield good results, but this is however the least meaningful result (which will be explained later in this subsection).

In appendix D the following quantities have been plotted for each case :

$$\epsilon(C_{sca})_{DDA} = \frac{C_{sca,i} - C_{sca,d}}{C_{sca,d}}, \tag{5.5}$$

$$\epsilon(F_{sca,x})_{DDA} = \frac{F_{sca,i,x} - F_{sca,d,x}}{\vec{F}^2_{sca,d}}, \tag{5.6}$$

$$\epsilon(F_{sca,y})_{DDA} = \frac{F_{sca,i,y} - F_{sca,d,y}}{\vec{F}^2_{sca,d}}, \tag{5.7}$$

$$\epsilon(F_{sca,z})_{DDA} = \frac{F_{sca,i,z} - F_{sca,d,z}}{\vec{F}^2_{sca,d}}. \tag{5.8}$$

Save for the cases of simulating aggregate 1 with rescaling factor 0.5 and both the refractive indices, the ratios $\epsilon(C_{sca})_{DDA}$ do not converge to zero but to percentages in the range of $50 - 150\%$ (for the case of aggregate 2, $m = 1.7 + 0.03i$ and scale-factor 0.25, $\epsilon(C_{sca})_{DDA}$ it even converged to 360%) [3]. In 1998 Kimura [9] also reported a difference between $C_{sca,d}$ and

[3]The simulations, resulting in the data presented in the tables of appendix E, were performed in single precision. Repeating them in double precision only caused some changes in the least significant decimals

$C_{sca,i}$. After Draine, [21], he argued that if absorption dominates scattering, i.e. $C_{abs} \rightarrow C_{ext}$, C_{abs} and C_{ext} have to be calculated to high precision to get a reasonable accuracy in $C_{sca} = C_{ext} - C_{abs}$. In practical computation he used the (ad hoc) formula

$$\begin{aligned} C_{sca} &= \frac{C_{sca,i} + C_{sca,d} f_a^2}{1 + f_a^2}, \\ f_a &= 100 \frac{C_{sca,i}}{C_{ext}}. \end{aligned}$$

In table 5.1 $\epsilon(C_{sca})_{DDA}$ and C_{abs}/C_{ext} are compared. Although Kimura's explanation might receive some support from aggregate 1 with scaling-factors 1 and 0.25, it can hardly be called conclusive. Alas he did not print the differences between direct and integrated scattering cross section. Based on the calculations in section 3.6 another explanation is offered here.

The ratios $\epsilon(F_{sca,x})_{DDA}$, $\epsilon(F_{sca,y})_{DDA}$, and $\epsilon(F_{sca,z})_{DDA}$ all converge to

scale-factor	1		0.5		0.25	
(%)	$\frac{C_{abs}}{C_{ext}}$	$\epsilon(C_{sca})$	$\frac{C_{abs}}{C_{ext}}$	$\epsilon(C_{sca})$	$\frac{C_{abs}}{C_{ext}}$	$\epsilon(C_{sca})$
grain 1 $m = 1.14 + 0.38i$	98	124	90	0.4	88	122
grain 1 $m = 1.7 + 0.03i$	49	85	18	0.4	14	88
grain 2 $m = 1.14 + 0.38i$	-	-	-	-	-	-
grain 2 $m = 1.7 + 0.03i$	-	-	18	52	21	362

Table 5.1: Illustration of Kimura's argument.

zero for rising integration-accuracy, but this means nothing with regard to the correctness of the scattering force. Starting from equation (3.10) it was shown that $\vec{F}_{out}$ $(= -\vec{F}_{sca,i})$ can be expressed as sum of $N(N-1)$ integrals $\vec{F}_{I,jl}$. After solving each of these integrals and comparing them term-wise to (3.15), $\vec{F}_{sca,d}$ and $\vec{F}_{sca,i}$ were shown to be formally equal, see steps (3.24)-(3.26).

Similarly to $\vec{F}_{out}$, $C_{sca,i}$ was expressed as sum of $N(N-1)$ integrals $C_{I,jl}$. After expanding the N terms in the operational expression for $C_{sca,d}$ to $N(N-1)$, using

$$\vec{E}_{inc,j} - \alpha_j^{-1} \vec{P}_j = -\sum_{l \neq j} \mathbf{A}_{jl} \cdot \vec{P}_l, \tag{5.9}$$

$C_{sca,d}$ and $C_{sca,i}$ were shown to be formally equal, again by term-wise comparison, see steps (3.28) to (3.29). The use of (5.9), by which the dipole

Figure 5.3: Aggregate illuminated by X-polarized light $m = 1.7 + 0.03i$,51 grains

moments are assumed to be correct, implies that if $C_{sca,i}$ does not converge to $C_{sca,d}$, the dipole moments are not correct. The combination of this reasoning and the fact that the residues do converge, points in the direction of an ill conditioned matrix $\mathbf{B} = \mathbf{I} - \mathbf{AC}$ (see chapter 2). This discussion will be continued in section 5.3.

For what it is worth, the forces per dipole are displayed for the case of aggregate 1 with refractive index m_b and without rescaling in figures 5.3 and 5.4. Notice the strongest forces are approximately aligned (anti-)parallel to the polarization of the incoming radiation. Also notice that almost all of these strongest forces appear in pairs of equal size and opposite direction. The corresponding grains seem to attract each other.

5.3 The difference $C_{sca,i} - C_{sca,d}$

As has been argued in section 3.6, the integrated and direct scattering cross section are equal, **if** the correct dipole moments are used. In this section the question of what will happen, if the dipole moments are **not** correct, will be discussed. Suppose the $3N$-vector $\vec{\mathbf{P}}$ is the solution to the linear system $(\mathbf{C}^{-1} - \mathbf{A})\vec{\mathbf{P}} = \vec{\mathbf{E}}_{inc}$ [4]. By iteration $\vec{\mathbf{P}}_{er} = \vec{\mathbf{P}} + \vec{\mathbf{Q}}$ is obtained.

[4]Equation (2.1) is recovered by substituting $\vec{\mathbf{P}} = \mathbf{C}\vec{\mathbf{E}}$.

Figure 5.4: Aggregate illuminated by Y-polarized light $m = 1.7 + 0.03i$,51 grains

The leftover residue belonging to $\vec{\mathbf{P}}_{er}$ is

$$\begin{aligned} \vec{\mathbf{r}} &= (\mathbf{C}^{-1} - \mathbf{A})\vec{\mathbf{P}}_{er} - \vec{\mathbf{E}}_{inc} \\ &= (\mathbf{C}^{-1} - \mathbf{A})\vec{\mathbf{Q}}. \end{aligned}$$

The integrated and direct scattering cross section resulting from $\vec{\mathbf{P}}_{er}$ are labeled with er. Writing

$$\begin{aligned} \tilde{C}_{sca,d} &= \frac{|\vec{E}_0|^2}{4\pi} C_{sca,d} \\ &= \left[Im(\vec{\mathbf{P}} \cdot \vec{\mathbf{E}}^*_{inc} - \vec{\mathbf{P}}(\mathbf{C}^{-1})^* \vec{\mathbf{P}}^*) + \frac{2k^3}{3} |\vec{\mathbf{P}}|^2 \right] \end{aligned} \tag{5.10}$$

instead of the expression in section 3.6 using summation notation, it is straightforward to show that $\tilde{C}_{sca,d,er}$ can be expanded to

$$\begin{aligned} \tilde{C}_{sca,d,er} &= k\left[Im(\vec{\mathbf{P}}_{er} \cdot \vec{\mathbf{E}}^*_{inc} - \vec{\mathbf{P}}_{er}(\mathbf{C}^{-1})^* \vec{\mathbf{P}}^*_{er}) + \frac{2k^3}{3} |\vec{\mathbf{P}}_{er}|^2 \right] \\ &= \tilde{C}_{sca,d} + k\left[\frac{2k^3}{3} (\vec{\mathbf{P}}^* \cdot \vec{\mathbf{Q}} + \vec{\mathbf{Q}}^* \cdot \vec{\mathbf{P}} + \vec{\mathbf{Q}}^* \cdot \vec{\mathbf{Q}}) \right. \\ &\quad \left. -Im\left\{ \vec{\mathbf{Q}} \cdot (\mathbf{A}\vec{\mathbf{P}})^* + (\vec{\mathbf{P}} + \vec{\mathbf{Q}}) \cdot (\mathbf{A}\vec{\mathbf{Q}})^* \right\} \right] \\ &\quad +Im\left\{ (\vec{\mathbf{P}} + \vec{\mathbf{Q}}) \cdot \vec{\mathbf{r}}^* \right\}. \end{aligned}$$

Returning to the summation notation from section 3.6, $\tilde{C}_{sca,d,er}$ becomes

$$\begin{aligned}\tilde{C}_{sca,d,er} &= \tilde{C}_{sca,d} + \sum_{j=1}^{N} \frac{2k^4}{3}(\vec{P}_j^* \cdot \vec{Q}_j + \vec{Q}_j^* \cdot \vec{P}_j + \vec{Q}_j^* \cdot \vec{Q}_j) \\ &\quad - \sum_{j \neq l} Re\Big\{ ik(\vec{Q}_j^* \cdot \mathbf{A}_{jl} \cdot \vec{P}_l + (\vec{P}_j + \vec{Q}_j)^* \cdot \mathbf{A}_{jl} \cdot \vec{Q}_l) \Big\} \\ &\quad - \sum_{j=1}^{N} Im\Big\{ k(\vec{P}_j + \vec{Q}_j) \cdot \vec{r}_j^* \Big\}.\end{aligned}$$

The exercise of working out the integral in $\tilde{C}_{sca,i,er}$ is equal to that for working out $C_{sca,i}$ in section 3.6, with the transitions $\vec{P}_j^* \rightarrow \vec{P}_{er,j}^*$ and $\vec{P}_l \rightarrow \vec{P}_{er,l}$.

$$\begin{aligned}\tilde{C}_{sca,i,er} &= \Bigg[\frac{2k^4}{3} \sum_{j=1}^{N} |\vec{P}_{er,j}|^2 \\ &\quad + \sum_{j \neq l} \Big\{ Re(a\, p_1)_{jl} Re(\vec{P}_{er,j} \cdot \vec{P}_{er,l}) + Re(a\, p_2)_{jl} Re(P_{er,j,z} P_{er,l,z}) \Big\} \Bigg], \\ &= \tilde{C}_{sca,i} + \frac{2k^4}{3} \sum_{j=1}^{N} (\vec{P}_j^* \cdot \vec{Q}_j + \vec{Q}_j^* \cdot \vec{P}_j + \vec{Q}_j^* \cdot \vec{Q}_j) \\ &\quad + \sum_{j \neq l} \Big\{ Re(a\, p_1)_{jl} Re(q_{er,1,jl}) + Re(a\, p_2)_{jl} Re(q_{er,2,jl}) \Big\}. \qquad (5.11)\end{aligned}$$

Analogous to $q_{1,jl}$ and $q_{2,jl}$ in section 3.6 the dummy variables $q_{er,1,jl}$ and $q_{er,2,jl}$ are

$$\begin{aligned}q_{er,1,jl} &= \vec{P}_j^* \cdot \vec{Q}_l + \vec{Q}_j^* \cdot \vec{P}_l + \vec{Q}_j^* \cdot \vec{Q}_l, \\ q_{er,2,jl} &= P_{j,z}^* Q_{l,z} + Q_{j,z}^* P_{l,z} + Q_{j,z}^* Q_{l,z}.\end{aligned}$$

Following the same procedure as in section 3.6 that leads to the equality $C_{sca,i} = C_{sca,d}$, the difference final result becomes

$$C_{sca,i,er} - C_{sca,d,er} = -\frac{4\pi k}{|\vec{E}_0|^2} \sum_{j=1}^{N} Im\Big\{ (\vec{P}_j + \vec{Q}_j) \cdot \vec{r}_j^* \Big\}. \qquad (5.12)$$

For two cases (5.12) has been calculated

1. aggregate 1, $m = 1.7 + 0.03i$, and scale-factor=0.5,

$$\begin{aligned}(5.12) &\rightarrow 1.75535e-17 \\ C_{sca,d} &= 5.54837e-10 \\ C_{sca,i} &= 5.53274e-10\end{aligned}$$

2. aggregate 2, $m = 1.7 + 0.03i$, and scale-factor=0.5,

$$\begin{aligned} (5.12) &\rightarrow -2.66299e-16 \\ C_{sca,d} &= 9.05444e-10 \\ C_{sca,i} &= 1.37888e-09 \end{aligned}$$

The numbers $C_{sca,i}$ are not listed in appendix E. They are extrapolations from the values listed in the corresponding tables in appendix E for $Res \rightarrow \infty$, assuming the convergence of the integration-procedure behaves like $\propto 2^{-Res}$, which is true for the tabulated values in both cases. It is clear that (5.12) severely underestimates the difference $C_{sca,i} - C_{sca,d}$ in both simulations.

There is yet a third way to calculate the scattering cross section,

$$\tilde{C}_{sca,3} = \frac{8\pi k}{3|\vec{E}_0|^2} \sum_{j=1}^{N} |\vec{P}_j|^2 - \frac{4\pi k}{|\vec{E}_0|^2} \sum_{j \neq l} Re(ik\vec{P}_j^* \cdot \mathbf{A}_{jl} \cdot \vec{P}_l).$$

Provided the integration-procedure is correct, $\tilde{C}_{sca,i}$ will always converge to this $\tilde{C}_{sca,3}$ for the same reason $\vec{F}_{sca,i}$ will always converge to $\vec{F}_{sca,d}$, even for a set of incorrect dipole moments. So if $\tilde{C}_{sca,i}$ converges to $\tilde{C}_{sca,3}$ also, then this is an even stronger indication the CGNR-procedure does not yield the correct results and another solution method should be used.

5.4 Literature survey

Although there is a significant amount of work on *applying* the DDA to aggregate particles and on radiation pressure calculations on aggregate particles, none of it will be addressed here. The short literature investigation presented here, will focus entirely on the (troublesome) convergence of the CGNR-method and on the validity of the DDA when applied to aggregates of spheres.

The DDA has been applied to fluffy/aggregate particles previously by Kimura and Rahola, see e.g. [9, 41]. Neither of these workers reported convergence-troubles such as the ones displayed by the simulations presented here. Kimura did not mention which iterative method he used, but based on his references he probably used Draine's public-domain code, which employs the "stabilized bi-conjugate gradient method" [42].

Rahola used the Q(uasi)M(inimal)R(esidue) method, instead of the CGNR-method, combined with FFT. In a second publication [43], he analyzed the spectrum of the DDA coefficient-matrix for a spheudosphere. Virtually all eigenvalues turned out to be on a line segment in the complex plane, which he took to account for the good performance of the QMR. In a third publication [44] he also analyzed the spectrum of the DDA coefficient-matrix for

a D(iffusion)L(imited)A(ggregation)-cluster. Again the bulk of the eigenvalues were on a line segment in the complex plane, but compared to the speudosphere the number of eigenvalues not on this line segment was much larger. This larger variance of the eigenvalues might account for the troublesome convergence displayed here.

The validity of the DDA will be discussed by comparison to the rigorous solution of the Maxwell equations for aggregates of spheres, [45, 46] (this rigorous solution has received a firm experimental foundation, see e.g. [47, 48, 49, 46] and references therein). Both articles deal with aggregates of two touching spheres. While Flatau et al, [45], obtained a good agreement, Xu and Gustafson, [46], report a failure of the DDA in accuracy combined with a much longer execution time for the DDA. Close inspection of the latter article shows the reason for the failure. For accurate results from the DDA one should take $D_\lambda > 10$. Due to a lack of memory Xu and Gustafson performed some of their DDA-simulations without obeying this rule, simulations whose results consequently deviate from the rigorous solution and the laboratory experiments. For two-sphere aggregates the DDA and the rigorous solution are in close agreement, if $D_\lambda > 10$ is obeyed. For larger spheres and refractive indices this implies more dipoles, which obviously increases the memory-use and execution-time for the DDA. So if Xu and Gustafson claim the DDA to be much slower (100-1000 times) than the rigorous solution without supporting execution-times, this can well be true.

But for our purpose simulations of two-sphere aggregates can merely be preliminary benchmarks; the numbers of grains in aggregate 1 and 2 are modest. The rigorous solution has been verified with laboratory experiments for aggregates containing up to 27 spheres [48], but the DDA has not yet been tested in this region. There is a lot of work still to be done.

Chapter 6

Current state of affairs and future-work

6.1 Conclusions

In chapter 3, a method for calculating radiation pressure in the DDA was derived, without the need for integration and with the possibility to extract the radiation pressure per dipole. It was also shown the $O(N^2)$-complexity of this method could be reduced to $O(N \log N)$. The radiation pressure resulting from this new, direct method was shown to be formally equal to the already existing method for calculating the radiation pressure, which integrates the impulse of the scattered radiation. Analogously, the two already existing methods for calculating the scattering cross section, by integration of the scattered intensity and by the subtracting the extinction and absorption cross section, were also shown to be formally equal. With the aid of Fast Fourier Transformation the direct method for calculating radiation pressure will probably take comparable or even less computing time, than the integration method. Combining this to the extra information delivered by the direct method, the radiation pressure per dipole, radiation pressure calculations in the DDA should preferably be done with new method, see section 4.3.

Tests simulating a range of absorbing spheres, chapter 4, were used to demonstrate the validity of the new radiation pressure method and the equivalence of the integration and direct methods, for both the radiation pressure and the scattering cross section. The overall conclusion for DDA-based radiation pressure calculations on *spherical* particles is that, compared to MIE-theory, the error in the radiation pressure cross section is comparable to the error in the extinction cross section.

The next step of applying the DDA to aggregate particles proved to be more cumbersome. First of all the integrated scattering cross section did not converge to the direct one. This can probably be attributed to ill

conditioning of the DDA-matrix.

6.2 Future-work

As has already been announced in the title of this thesis, it is merely an exploration of DDA-based radiation pressure calculations on aggregate particles. Therefore the subject of future-work will receive more attention than the preceding conclusions.

6.2.1 DDA

First of all the benchmarks on spherical particles were not exhaustive; the radiation pressure per dipole was only verified by comparing the accumulated radiation pressure for all dipoles to the radiation pressure cross section resulting from MIE-code. As has already been argued, the work of Peter Debye, [13], might serve as guide for also verifying the radiation pressure per dipole; discretizing the integration of the Maxwell Stress Tensor in the same way the integral equation leading to the DDA-equations is discretized, will probably solve this problem.

An urgent matter is the insertion of Fast Fourier Transformation in the direct calculation of radiation pressure, especially since the advent of the "Fastest Fourier Transform in the West"(FFTW). This is a C-package for Fast Fourier Transformation, developed at MIT by Matteo Frigo and Steven G. Johnson; it includes subroutines for parallel, and multi-dimensional FFT under MPI [1]. They claim their portable package to be superior to other public-domain FFT-codes and support their claim by a set of benchmarks. Embedding this package into the current fDDA-code (not just into the radiation pressure algorithm but also in the CG-procedure) will probably increase its performance and portability.

Furthermore the use of CGNR for solving the DDA-equations should be reconsidered. Considering the discrepancy between integrated and direct scattering cross section from a purely algebraic level, it means the dipole moments resulting from CG iterations, do not satisfy the DDA-equations, although the residue does converge. The Q(uasi)M(inimal)R(esidue) method is thought to be more robust, and needs only one matrix-vector product per iteration, [41]. Another option is directly calculating the inverse by LU-factorization; usually the number of dipoles, i.e. matrix-size, prohibits such an approach, but for the 51-grain and 101-grain aggregates considered in chapter 5, resulting in complex 150×150-matrix and 300×300-matrix respectively, the problem-size of LU-factorization must be within reach.

[1] Available for free from **http://www.fftw.org/**

6.2.2 Light scattering by and radiation pressure on aggregate particles

After the problems with solving the DDA-equations have been eradicated (DDA-simulations of porous/aggregate particles by other workers [9, 41] indicate this must be possible), the accuracy of the DDA must be addressed. An internal check would be increasing the number of dipoles per grain; $D_{grain} = 8, 32, \ldots$. For using more than 32 dipoles per grain, probably only aggregate 1 or even smaller ones can be used. Using 32 dipoles per grain means replacing each grid-point by a small 4^3 grid, i.e. rescaling the number of grid-points with a factor 64. The next step will be $D_{grain} = 136$, i.e. replacing each grid-point by a 6^3 grid and thereby rescaling the number of grid-points with a factor 216. In figure 6.1 the FFT-complexity comparison

Figure 6.1: Each star in the $(N_{non-void}, N)$-plane represents aggregate 1 discretized with the number accompanying each is the number of dipoles per grain it represents

displayed in figure 5.2 is redrawn, this time for aggregate 1 with $D_{grain} > 1$ as described above. This illustrates that when increasing the number of dipoles per grain, eventually any aggregate will benefit from FFT, since $N_{non-void} \propto N$ for a particular aggregate.

By raising the number of dipoles per grain, the aggregate-deformation resulting from projecting the aggregate on a rectangular grid will decrease. But still the grain will be shifted. It might therefore be useful to recover the $O(N^2_{non-void})$-method not just for execution-time comparison but also for comparison of the scattered fields (that is with multiple dipoles per grain).

Next to these DDA-specific checks the scattered field should also be com-

pared to another independent solution, the rigorous solution of the Maxwell equations for multiple spheres a.k.a. multipole expansion method or extended Mie-theory. This method has received experimental verification for up to 27-sphere aggregates [48]. Of course direct comparison to experiments of light scattering resulting from aggregate particles would be the best check, but these are not available at the moment. Therefore comparison to extended MIE-theory seems to be the most reliable test at the moment.

It might be possible the DDA fails this test, or that the accuracy demands, i.e. large grids, render it computationally prohibitive/much more demanding than extended MIE-theory itself. In these cases replacing the DDA by extended MIE-theory might be an option. A serious drawback is that this approach will take us back to where we started; the mathematical apparatus for radiation pressure calculations has (to our knowledge) not yet been developed for extended MIE-theory. But this drawback might be less serious than it appears to be, because it descends from MIE-theory. MIE-theory from which Debye rigorously derived expressions for the radiation pressure cross section of a single sphere.

6.3 Final conclusions

The main part of this thesis is devoted to extracting radiation pressure from DDA-simulations. As the title of this thesis already suggests, it is merely a first exploration of applying the resulting expressions to aggregate particles. Not just because of the new means for extracting radiation pressure, but also because there is not yet an established recipe for applying the DDA to aggregate particles (assuming self-consistent results can be obtained); how should the polarizabilities be determined, and what number of dipoles per spherical grain should be used, are questions that need to be answered. Comparing the DDA to extended MIE-theory for two-sphere aggregates is a first step to answering these questions, but it cannot possibly provide a conclusive answer.

Bibliography

[1] Van de Hulst, H.C., "Light Scattering by Small Particles", Dover Publications Inc. (1957).

[2] Bohren, C.F. and Huffman, D.R., "Absorption and Scattering of Light by Small Particles", Wiley, (1983).

[3] Mishchenko, M.I., Hovenier, J.W., and Travis, L.D., "Light Scattering by Nonspherical Particles", Academic Press, (2000).

[4] Mathis, J.S., Whiffen, G., "Composite Interstellar Grains", *ApJ*, **341**, 808-822 (1989).

[5] Mathis, J.S., Rumpl, W. and Nordsieck, K.H., "The size distribution of interstellar grains", *ApJ*, **217**, 425-433 (1977).

[6] Dominik, C. and Tielens, A.G.G.M., "Resistance in the adhesive contact of two elastic spheres", *Philosophical Magazine A*, **72**, 783-803 (1995).

[7] Dominik, C. and Tielens, A.G.G.M., "Resistance to sliding on atomic scales in the adhesive contact of two elastic spheres", *Philosophical Magazine A*, **73**, 1279-1302 (1996).

[8] Dominik, C. and Tielens, A.G.G.M., "The physics of dust coagulation and the structure of dust aggregates in space", *ApJ*, **480**, 647-673 (1997).

[9] Kimura, H. and Mann, I., "Radiation Pressure Cross Sections for Fluffy Aggregates", *J. Quant. Spectrosc. Radiant. Transfer*, **60**, (1998).

[10] Mukai, T., Ishimoto, H., Kozasa, T., Blum, J. and Greenberg, J. M., "Radiation pressure forces of fluffy porous grains", *Astron. Astrophys.*, **262**, 315-320 (1992).

[11] Kozasa, T., Blum, J. and Mukai, T., "Optical propperties of dust aggregates I. wavelength dependence", *Astron. Astrophys.*, **263**, 423-432 (1992).

[12] Kozasa, T., Blum, J., Okamoto and Mukai, T., "Optical propperties of dust aggregates II. angular dependence of scattered light", *Astron. Astrophys.*, **276**, 278-288 (1993).

[13] Debye, P., "Der Lichdruck auf Kugeln von beliebligem Material", *Ann. Phys.*, **30**, 57-136 (1909).

[14] Draine, B.T. and Flatau, P.J., "Discrete-dipole approximation for scattering calculations", *J. Opt. Soc. Am. A*, **11**, 1491-1499 (1994).

[15] Goedecke, G.H. and O'Brien, S.G., "Scattering by irregular inhomogeneous particles via the digitized Green's function algorithm", *Appl. Opt.*, **27**, 2431-2438 (1988).

[16] Newman, E.H. and Kingsley, K., "An introduction to the method of moments", *J. Comput. Phys.*, **68**, 1-18 (1991).

[17] Barber, P.W. and Hill, S.C., "Light Scattering by Particles: Computational Methods", World Scientific, (1990).

[18] Taflove, Allen, "Computational Electordynamics: the Finite-Difference Time-Domain method", Artech House, (1995).

[19] Kim, S.-H., Martin, P.G. and Hendry, P.D., "The size distribution of interstellar dust particles", *ApJ*, **422**, 164-175 (1994).

[20] Bernatowicz, T.J., Amari, S., Zinner, E.K. and Lewis, R.S. "Interstellar grains within interstellar grains", *ApJ*, **422**, L73-L76 (1991).

[21] Draine, B.T., "The Discrete-Dipole Approximation and its Applications to Interstellar Graphite grains", *ApJ*, **333**, 842-872 (1988).

[22] Jackson, J.D., "Classical Electrodynamics", Wiley, New York, (1975).

[23] Lakhtakia and Akhlesh, "Macroscopic theory of the coupled dipole approximation method", *Opt. Comm.*, **79**, 1-5 (1990).

[24] Hoekstra, A.G., "Computer Simulations of Elastic Light Scattering, Implementation and Applications", University of Amsterdam (1994).

[25] DeVoe, H., "Optical properties of molecular aggregates. I Classical model of electronic absorption and refraction", *J. Chem. Phys.*, **41**, 393-400 (1964)

[26] Purcell, "E.M. and Pennypacker, C.R., Scattering and absorption of light by nonspherical dielectric grains", *ApJ*, **186**, 706-714 (1973).

[27] Goodman, J.J., Draine, B.T. and Flatau, P.J., "Application of fast-Fourier-Transform techniques to the discrete-dipole approximation", *Opt. L.*, **16**, 1198-1200 (1991).

[28] Hoekstra, A.G., Grimminck, M.D and Sloot, P.M.A, "Large scale simulations of elastic light scattering by a fast Discrete Dipole Approximation", *Journal of Modern Physics C*, **9**, 87-102 (1998).

[29] Draine, B.T., Weingartner, J.C., "Radiative torques on interstellar grains I.Superthermal Spin-up", *ApJ*, **470**, 551-565 (1996).

[30] Geist, A., Beguelin, A, Dongarra, J., Jiang, W, Mancheck, R. and Sunderam, V., "PVM: Parallel Virtual Machine - A User's Guide and Tutorial for Networked Parallel Computing" , (1994).

[31] Snir, M., Otto, S., Huss-Ledermann, S., Walker, D., Dongarra, J., "MPI: The Complete Reference", MIT Press, (1996).

[32] Gordon, J.P., "Radiation Forces and Momenta in Dielectric Media", *Phys. ReV. A*, **8**, 14-21 (1973).

[33] William H. Press, Brian P. Flannery , Saul A. Teukolsky and William T. Vettering, Numerical Recipes in C, Cambridge University Press (1988).

[34] Markel, V.A.,"Antisymmetrical optical states", *J. Opt. Soc. Am. B*, **12**, 1783-1791 (1995)

[35] Hoekstra, A.G. and Sloot, P.M.A., "Coupled Dipole Simulations of Elastic Light Scattering on Parallel Systems", *International Journal of Modern Physics C*, **6**, 663-679 (1995)

[36] Hoekstra, A.G., Rahola, J. and Sloot, P.M.A, "Accuracy of Internal Fields in Volume Integral Equation Simulations of Light Scattering", *Appl. Opt.*, **37**, 8482-8497 1998

[37] Draine, B.T. and Goodman, J., "Beyond Clausius-Mossoti: wave propagation on a polarizable lattice and the discrete dipole approximation", *ApJ*, **405**, 685-697 (1993).

[38] Hoekstra, A.G., and Sloot, P.M.A, "Dipolar unit size in coupled dipole calculations of the scattering matrix elements", *Opt. L.* **18**, 1211-1213 (1993).

[39] Okamoto, H., "Light scattering by clusters: the a1-term method", *Optical Review*, **2**, 407-412 (1995).

[40] Dungey, C.E., and Bohren, C.F., "Light Scattering by nonspherical particles: A refinement to the coupled dipole method", *J. Opt.Soc. Am. A*, **8**, 81-87 (1991).

[41] Lumme, K. and Rahola, J., "Light Scattering by porous dust particles in the Discrete Dipole Approximation", *ApJ*, **425**, 653-667 (1994).

[42] Flatau, P.J., "Improvements in the discrete-dipole approximation method of computing scattering and absorption", *Opt.Lett*, **21**, 1205-1207 (1997).

[43] Rahola, J., "Solution of dense systems of linear equations in the Discrete Dipole Approximation", *SIAM J.Sci.Comp.*, **17**, 78-89 (1996).

[44] Rahola, J., "Solution of dense systems of linear equations in electromagnetic scattering calculations", Licenciates' Thesis, Helsinki University of technology, (1994).

[45] Flatau, P.J., Fuller, K.A. and Mackowski, D.W., "Scattering by two spheres in contact: comparison between discrete-dipole approximation and modal analysis", *Appl. Opt.*, **32**, 3302-3305 (1993).

[46] Xu, Y.-L. and Gustafson, B.A.S.,"Comparison between Multisphere Light-Scattering calculations: Rigorous Solution and Discrete Dipole Approximation", *ApJ*, **513**, 894-909 (1999).

[47] Xu, Y.-L., "Electromagnetic Scattering by an aggregate of spheres", *Appl. Opt.*, **34**, 4573-4588 (1995).

[48] Xu, Y.-L. and Gustafson, B. A. S., "Experimental and theoretical results of light scattering by aggregates of spheres", *Appl. Opt.*, **36**, 8026-8030 (1997).

[49] Xu, Y.-L. and Wang, R.T., "Electromagnetic scattering by an aggregate of spheres: Theoretical and experimental study of the amplitude scattering matrix", *Phys. Rev. E*, **58**, 3931-3948 (1998).

Appendix A

Detailed calculations

A.1 Direct Radiation Pressure

A.1.1 Time-averaging the force per dipole

The time-dependent force per dipole (3.1) reads

$$\begin{aligned}\vec{F}_j(t) &= Re\Big(e^{-i\omega t}\vec{P}_j\cdot\nabla_j\Big)Re\Big(e^{-i\omega t}\vec{E}_j\Big)\\ &\quad +Re\Big(\frac{d(e^{-i\omega t}\vec{P}_j)}{dt}\Big)\times Re\Big(e^{-i\omega t}\vec{B}_j\Big).\end{aligned}$$

Assuming the dipoles are at rest $\frac{1}{c}\frac{d(e^{-i\omega t}\vec{P}_j)}{dt}$ equals $(-ik)e^{-i\omega t}\vec{P}_j$. Separating all variables in real and imaginary parts the time-dependent force becomes

$$\begin{aligned}\vec{F}_j(t) &= \Big(\cos\omega t Re(\vec{P}_j)-\sin\omega t Im(\vec{P}_j)\Big)\cdot\\ &\quad \nabla_j\Big(\cos\omega t Re(\vec{E}_j)-\sin\omega t Im(\vec{E}_j)\Big)\\ &\quad -k\Big(\cos\omega t Re(i\vec{P}_j)-\sin\omega t Im(i\vec{P}_j)\Big)\times\\ &\quad \Big(\cos\omega t Re(\vec{B}_j)-\sin\omega t Im(\vec{B}_j)\Big).\end{aligned}$$

The time-averaged force becomes

$$\begin{aligned}2<\vec{F}_j> &= Re(\vec{P}_j\cdot\nabla_j)Re(\vec{E}_j)+Im(\vec{P}_j\cdot\nabla_j)Im(\vec{E}_j)\\ &\quad -Re(ik\vec{P}_j)\times Re(\vec{B}_j)-Im(ik\vec{P}_j)\times Im\vec{B}_j).\end{aligned}$$

Using the relation

$$\begin{aligned}
&Re(\vec{\alpha}) \times Re(\vec{\beta}) + Im(\vec{\alpha}) \times Im(\vec{\beta}) = \\
&\hat{e}_o\, \epsilon_{opq} \left(Re(\alpha_p) Re(\beta_q) + Im(\alpha_p) Im(\beta_q) \right) = \\
&\epsilon_{opq} \quad \left(Re(\alpha_p^* \beta_q) \right) = \\
&Re(\vec{\alpha^*} \times \vec{\beta})
\end{aligned}$$

and $(ik\vec{P})^* = -ik\vec{P}^*$, yields

$$< \vec{F}_j >= \frac{1}{2} Re\Big(\vec{P}_j^* \cdot \nabla_j \vec{E}_j \quad + \quad ik\vec{P}_j^* \times \vec{B}_j \Big).$$

Here the Einstein-summation convention for double indices is used and ϵ_{opq} is the Levi-Civita tensor, which obeys

$$\epsilon_{opq} = \begin{cases} 0 & \text{if at least two indices are the same,} \\ 1 & \text{if } o,p,q \text{ is an even permutation of } 1,2,3, \\ -1 & \text{if } o,p,q \text{ is an odd permutation of } 1,2,3. \end{cases}$$

A.1.2 Differentiations

For easy reference the distance vector and its corresponding unit vector are given again:

$$\begin{aligned}
\vec{r}_{jl} &= \vec{r}_j - \vec{r}_l, \\
\hat{n}_{jl} &= \vec{r}_{jl}/r_{jl}.
\end{aligned}$$

Working out $\vec{P}_j^* \cdot \nabla_j \vec{E}_{jl}$ means doing three differentiations of the form

$$(\vec{P}_j^* \cdot \nabla_j) f(r_{jl}) = (\vec{P}_j^* \cdot \nabla_j r_{jl}) f^{'}(r_{jl})$$

resulting in a scalar and one resulting in a vector-value. For the first three particular cases the scalar functions and their derivatives are

$$\begin{aligned}
(e^{ikx})^{'} &= ike^{ikx}, \\
g(x) &= \tfrac{k^2}{x} - \tfrac{1}{x^3} + \tfrac{ik}{x^2}, \\
g^{'}(x) &= -\tfrac{k^2}{x^2} + \tfrac{3}{x^4} - \tfrac{2ik}{x^3}, \\
h(x) &= \tfrac{3}{x^3} - \tfrac{3ik}{x^2} - \tfrac{k^2}{x}, \\
h^{'}(x) &= -\tfrac{9}{x^4} + \tfrac{6ik}{x^3} + \tfrac{k^2}{x^2}.
\end{aligned}$$

The differentiation of the vector function can be simply rewritten to

$$(\vec{P}_j^* \cdot \nabla_j) \hat{n}_{jl} (\hat{n}_{jl} \cdot \vec{P}_l) = \hat{n}_{jl} (\vec{P}_j^* \cdot \nabla_j)(\hat{n}_{jl} \cdot \vec{P}_l) + (\hat{n}_{jl} \cdot \vec{P}_l)(\vec{P}_j^* \cdot \nabla_j) \hat{n}_{jl}. \quad \text{(A.1)}$$

The differentiations in (A.1) can decomposed into

$$\begin{aligned}(\vec{P}_j^* \cdot \nabla_j) n_{jl,u} &= \frac{1}{r_{jl}}(\vec{P}_j^* \cdot \nabla_j) r_{jl,u} - \frac{r_{jl,u}}{r_{jl}^2}(\vec{P}_j^* \cdot \nabla_j) r_{jl} \\ &= \frac{1}{r_{jl}}\Big(P_{j,u}^* - (\vec{P}_j^* \cdot \hat{n}_{jl}) n_{jl,u}\Big) \qquad u \in \{x, y, z\}. \quad \text{(A.2)}\end{aligned}$$

Inserting expressions in (A.1) yields

$$\begin{aligned}(\vec{P}_j^* \cdot \nabla_j)[\hat{n}_{jl}(\hat{n}_{jl} \cdot \vec{P}_l)] &= \frac{1}{r_{jl}}\Big[(\vec{P}_j^* \cdot \vec{P}_l)\hat{n}_{jl} + \vec{P}_j^*(\hat{n}_{jl} \cdot \vec{P}_l) \\ &\quad -2(\vec{P}_j^* \cdot \hat{n}_{jl})\hat{n}_{jl}(\hat{n}_{jl} \cdot \vec{P}_l)\Big].\end{aligned}$$

In full detail the vector $\vec{P}_j^* \cdot \nabla_j \vec{E}_{jl}$ reads

$$\begin{aligned}\vec{P}_j^* \cdot \nabla_j \vec{E}_{jl} &= \vec{P}_j^* \cdot \nabla_j \Big\{ e^{ikr_{jl}} \{ g(r_{jl})\, \vec{P}_l + h(r_{jl})\, \hat{n}_{jl}(\hat{n}_{jl} \cdot \vec{P}_l) \} \Big\}. \quad \text{(A.3)} \\ &= (\vec{P}_j^* \cdot \nabla_j e^{ikr_{jl}}) \{ g(r_{jl})\, \vec{P}_l + h(r_{jl})\, \hat{n}_{jl}(\hat{n}_{jl} \cdot \vec{P}_l) \} \\ &\quad + (\vec{P}_j^* \cdot \nabla_j g(r_{jl}))\, e^{ikr_{jl}}\, \vec{P}_l \\ &\quad + (\vec{P}_j^* \cdot \nabla_j h(r_{jl}))\, e^{ikr_{jl}}\, \hat{n}_{jl}(\hat{n}_{jl} \cdot \vec{P}_l) \\ &\quad + h(r_{jl})\, e^{ikr_{jl}}\, \vec{P}_j^* \cdot \nabla_j [\hat{n}_{jl}(\hat{n}_{jl} \cdot \vec{P}_l)].\end{aligned}$$

Using $(\vec{P}_j^* \cdot \nabla_j r_{jl}) = \vec{P}_j^* \cdot \hat{n}_{jl}$ (A.3) becomes

$$\begin{aligned}\vec{P}_j^* \cdot \nabla_j \vec{E}_{jl} &= e^{ikr_{jl}} \Bigg[\\ &\quad (\vec{P}_j^* \cdot \vec{P}_l)\hat{n}_{jl} \frac{h}{r_{jl}} \\ &\quad + (\vec{P}_j^* \cdot \hat{n}_{jl})\hat{n}_{jl}(\hat{n}_{jl} \cdot \vec{P}_l) \left\{ (ik - \frac{2}{r_{jl}})h + h' \right\} \\ &\quad + (\vec{P}_j^* \cdot \hat{n}_{jl})\vec{P}_l \left\{ ikg + g' \right\} \\ &\quad + \vec{P}_j^*(\hat{n}_{jl} \cdot \vec{P}_l)\, \frac{h}{r_{jl}} \Bigg],\end{aligned}$$

$$
\begin{aligned}
= \quad & e^{ikr_{jl}} \Bigg[\\
& (\vec{P}_j^* \cdot \vec{P}_l)\hat{n}_{jl}\big(\frac{3}{r_{jl}^4} - \frac{3ik}{r_{jl}^3} - \frac{k^2}{r_{jl}^2}\big) \\
& -(\vec{P}_j^* \cdot \hat{n}_{jl})\hat{n}_{jl}(\hat{n}_{jl} \cdot \vec{P}_l)\big(5(\frac{3}{r_{jl}^4} - \frac{3ik}{r_{jl}^3} - \frac{k^2}{r_{jl}^2}) + \frac{ik^3}{r_{jl}} - \frac{k^2}{r_{jl}^2}\big) \\
& +(\vec{P}_j^* \cdot \hat{n}_{jl})\vec{P}_l\big(\frac{3}{r_{jl}^4} - \frac{3ik}{r_{jl}^3} - \frac{2k^2}{r_{jl}^2} + \frac{ik^3}{r_{jl}}\big) \\
& +\vec{P}_j^*(\hat{n}_{jl} \cdot \vec{P}_l)\big(\frac{3}{r_{jl}^4} - \frac{3ik}{r_{jl}^3} - \frac{k^2}{r_{jl}^2}\big) \Bigg].
\end{aligned}
$$

A.2 Relating the integrated and direct methods

A.2.1 Evaluating $I_u(\alpha)$

The evaluation of $I_u(\alpha)$ comes down to multiple partial integration. There is a straightforward relation between the cases of I_u and I_{u-1}

$$
\begin{aligned}
I_u(\alpha) &= \int_{-1}^{1} dt\, t^u\, e^{i\alpha t}, \\
&= \frac{t^u e^{i\alpha t}}{i\alpha}\Big|_{t=-1}^{t=1} - \frac{u}{i\alpha}\int_{-1}^{1} dt\, t^{u-1}\, e^{i\alpha t}, \\
&= \frac{e^{i\alpha} + e^{-i\alpha}\,(-1)^{u+1}}{i\alpha} - \frac{uI_{u-1}(\alpha)}{i\alpha} \quad \text{for } 1 \le u.
\end{aligned}
$$

$I_u(\alpha)$ is expanded for $u \le 3$

$$
\begin{aligned}
I_0 &= (e^{i\alpha} - e^{-i\alpha})(i\alpha)^{-1}, \\
I_1 &= (e^{i\alpha} + e^{-i\alpha})(i\alpha)^{-1} \\
&\quad -(e^{i\alpha} - e^{-i\alpha})(i\alpha)^{-2}, \\
I_2 &= (e^{i\alpha} - e^{-i\alpha})\{(i\alpha)^{-1} + 2(i\alpha)^{-3}\} \\
&\quad -(e^{i\alpha} + e^{-i\alpha})2(i\alpha)^{-2}, \\
I_3 &= (e^{i\alpha} + e^{-i\alpha})\{(i\alpha)^{-1} + 6(i\alpha)^{-3}\} \\
&\quad -(e^{i\alpha} - e^{-i\alpha})\{3(i\alpha)^{-2} + 6(i\alpha)^{-4}\}.
\end{aligned}
$$

For further use some combinations are calculated and cast into a different form

$$\begin{aligned} I_0 + I_2 &= 4Re(e^{i\alpha}\{\frac{1}{\alpha^2} - \frac{i}{\alpha} + \frac{i}{\alpha^3}\}), \\ I_0 - 3I_2 &= 4Re(e^{i\alpha}\{\frac{-3}{\alpha^2} + \frac{i}{\alpha} - \frac{3i}{\alpha^3}\}), \\ I_1 &= 2iIm(e^{i\alpha}\{\frac{-i}{\alpha} + \frac{1}{\alpha^2}\}), \\ I_3 - I_1 &= 4iIm(e^{i\alpha}\{-\frac{3}{\alpha^4} + \frac{3i}{\alpha^3} + \frac{1}{\alpha^2}\}). \end{aligned}$$

A.2.2 Reduction of integral expressions for C_{sca} and $\vec{F}_{sca}$

Before the integrals are solved the dyadic

$$\begin{aligned} N(\phi,t) &= \hat{n}\hat{n} \\ &= \begin{pmatrix} \cos^2\phi\, s^2(t) & \sin\phi\,\cos\phi\, s^2(t) & \cos\phi\, ts(t) \\ \sin\phi\,\cos\phi\, s^2(t) & \sin^2\phi\, s^2(t) & \sin\phi\, ts(t) \\ \cos\phi\, ts(t) & \sin\phi\, ts(t) & t^2 \end{pmatrix} \end{aligned}$$

(with $s(t) = \sqrt{1-t^2}$) is introduced. The integral-terms in (3.20) read in full detail

$$\begin{aligned} \vec{F}_{I,jl} &= \frac{k^4}{8\pi}\int_0^{2\pi} d\phi \int_{-1}^{1} dt\, e^{ikr_{jl}t} \\ &\quad \begin{pmatrix} s(t)\,\cos\phi \\ s(t)\,\sin\phi \\ t \end{pmatrix} \left[(\vec{P}_j^* \cdot \vec{P}_l) - (\vec{P}_j^*)^T \cdot N(\phi,t) \cdot \vec{P}_l \right]. \end{aligned} \quad \text{(A.4)}$$

In the first term on the right hand side of (A.4) only the z-component does not vanish. The second term on the right hand side of (A.4) consists of 27 integrals; a sum of 9 for each spatial direction. Piecewise evaluation of the ϕ-dependent parts shows only of those integrals 7 not to vanish,

- x-direction : the terms corresponding to N_{13} and N_{31},
- y-direction : the terms corresponding to N_{23} and N_{32},
- z-direction : the terms corresponding to the diagonal-elements of N.

This reduces $\vec{F}_{I,jl}$ to

$$\begin{aligned} \vec{F}_{I,jl} &= \frac{k^4(I_3(kr_{jl}) - I_1(kr_{jl}))}{8} \begin{pmatrix} P^*_{j,x}\,P_{l,z} + P^*_{j,z}\,P_{l,x} \\ P^*_{j,y}\,P_{l,z} + P^*_{j,z}\,P_{l,y} \\ P^*_{j,x}\,P_{l,x} + P^*_{j,y}\,P_{l,y} - 2P^*_{j,z}\,P_{l,z} \end{pmatrix} \\ &\quad + \frac{k^4 I_1(kr_{jl})}{4} \begin{pmatrix} 0 \\ 0 \\ P^*_{j,x}\,P_{l,x} + P^*_{j,y}\,P_{l,y} \end{pmatrix}. \end{aligned} \quad \text{(A.5)}$$

For $j = l$ the complex exponential factor reduces to 1. The first term on the right hand side of (A.4) vanishes because $\int_{4\pi} d\Omega\hat{n} = 0$. Returning to the notation $(\vec{P}_j^* N(\phi,t)\vec{P}_j) = (\vec{P}_j^* \cdot \hat{n})(\hat{n} \cdot \vec{P}_j^*)$ it is clear that

$$(\vec{P}_j^* \cdot \hat{n})(\hat{n} \cdot \vec{P}_j) = \Big(Re(\vec{P}_j) \cdot \hat{n}\Big)^2 + \Big(Im(\vec{P}_j) \cdot \hat{n}\Big)^2.$$

This way the evaluation of the second term comes down to two integrations of the form $\int d\Omega\hat{n}\big(\vec{a}\cdot\hat{n}\big)^2$, with $\vec{a}$ a constant real vector. By choosing z-axis $\parallel \vec{a}$, the dot product $\vec{a} \cdot \hat{n}$ reduces to $a_z \cos\theta$.

$$\int d\Omega\hat{n}\big(\vec{a} \cdot \hat{n}\big)^2 = a_z^2 \int_0^{\pi} d\theta \int_0^{2\pi} d\phi \sin\theta\cos^2\theta \begin{pmatrix} \sin\theta\cos\phi \\ \sin\theta\sin\phi \\ \cos\theta \end{pmatrix}.$$

Because $\cos\phi$ and $\sin\phi$ are anti-symmetrical on the interval $0 \leq \phi \leq 2\pi$ and $\sin\theta\cos^3\theta$ is anti-symmetrical on the interval $0 \leq \theta \leq \pi$, all three components vanish, so $\vec{F}_{I,jj} = 0$.

Similarly (3.21) reads in full detail

$$C_{I,jl} = \frac{k^4}{\vec{E}_{inc}^2} \int_0^{2\pi} d\phi \int_{-1}^{1} dt\, e^{ikr_{jl}t} \left[(\vec{P}_j^* \cdot \vec{P}_l) - (\vec{P}_j^*)^T \cdot N(\phi,t) \cdot \vec{P}_l \right] \quad \text{(A.6)}$$

For $j = l$ the first term on the right hand side of (A.6) equals 4π. In the second term only the integrals corresponding to the diagonal elements of $N(\phi,t)$ do not vanish. Using $\int_0^{\pi/2} d\theta \sin^3\theta = 2/3$ it readily follows that $C_{I,jj} = \frac{8\pi k^4}{3}|\vec{P}_j^2|$. For $j \neq l$ piecewise evaluation of the ϕ-dependent parts, will again show a number of terms to vanish. The second term on the right hand side of (A.6) is again a sum of 9 integrals, of which only the ones corresponding to the diagonal elements do not vanish;

$$\begin{aligned} C_{I,jl} &= \frac{\pi k^4}{\vec{E}_{inc}^2} \Big[2\vec{P}_j^* \cdot \vec{P}_l I_0(kr_{jl}) - (P_{j,x}^* P_{l,x} + P_{j,y}^* P_{l,y})(I_0(kr_{jl}) - I_2(kr_{jl})), \\ &\quad - 2P_{j,z}^* P_{l,z} I_2(kr_{jl}) \Big] \\ &= \frac{\pi k^4}{\vec{E}_{inc}^2} \Big[\vec{P}_j^* \cdot \vec{P}_l (I_0(kr_{jl}) + I_2(kr_{jl})) \\ &\quad + P_{j,z}^* P_{l,z} (I_0(kr_{jl}) - 3I_2(kr_{jl})) \Big]. \end{aligned}$$

Appendix B

Graphs : Spherical particles

B.1 Errors vs. resolution

B.1.1 m = 1.05

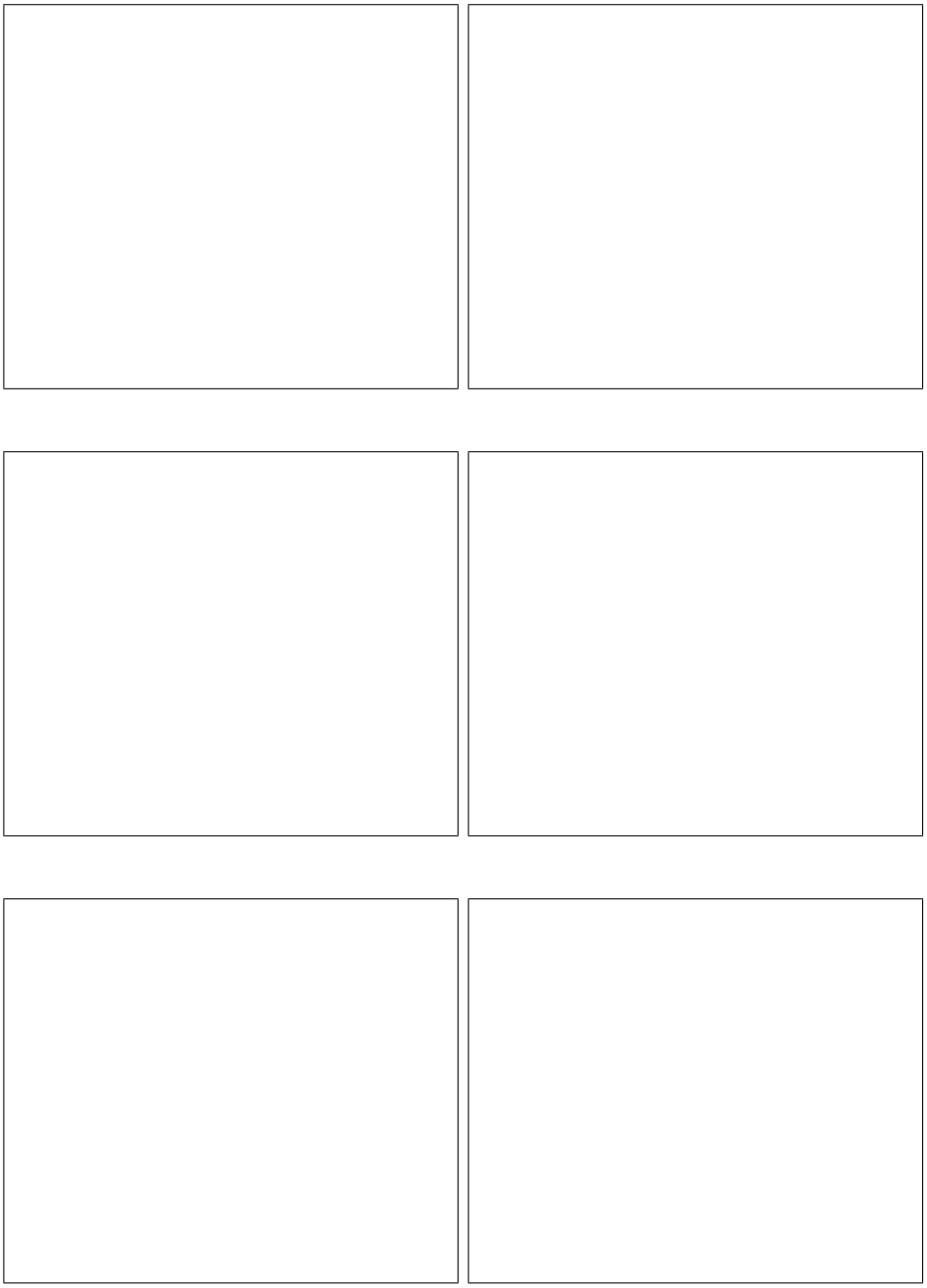

B.1.2 m = 1.14+0.38i

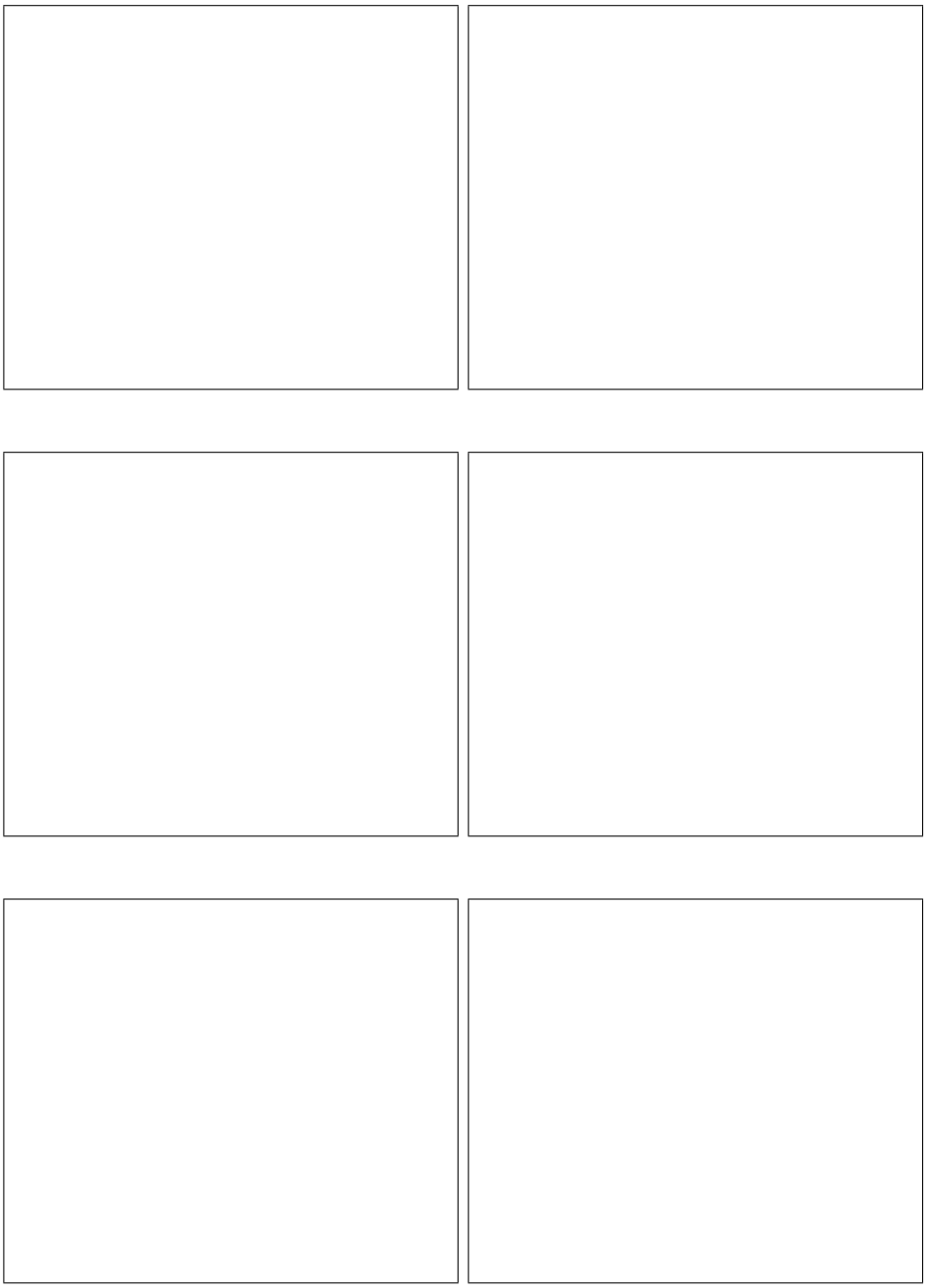

B.1.3 m = 1.33+0.01i

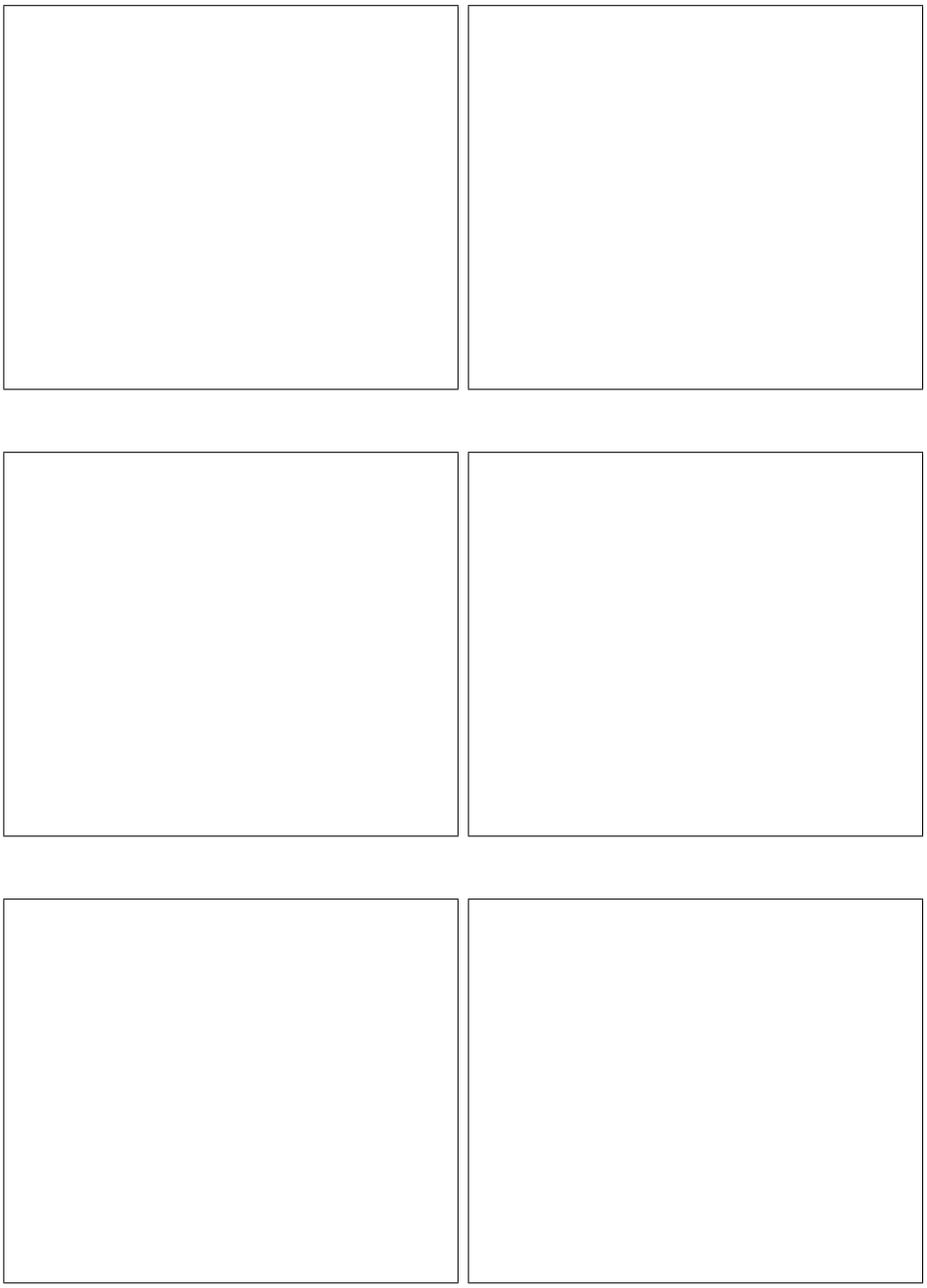

B.1.4 m = 1.68+0.03i

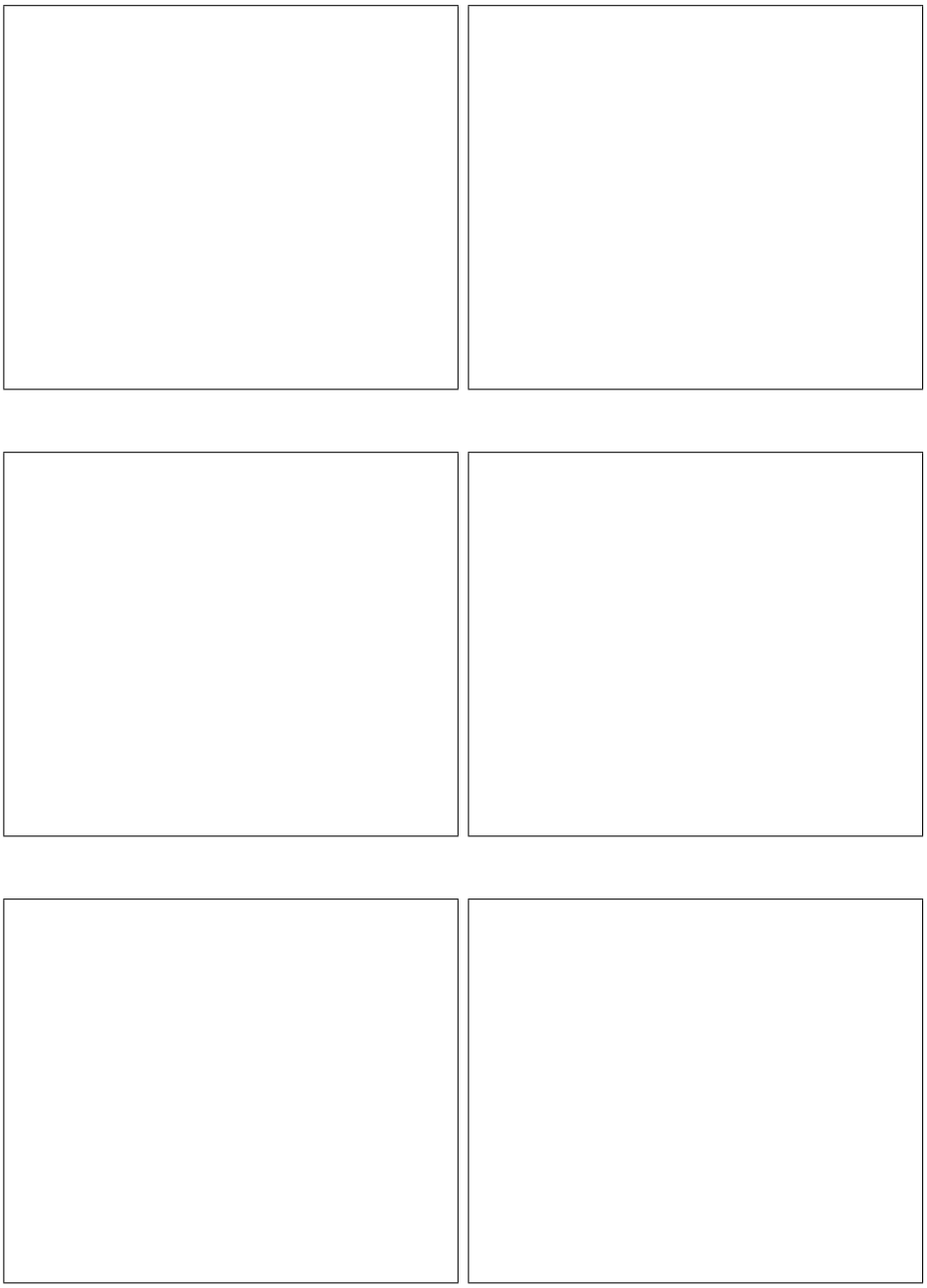

B.1.5 m = 1.7+0.156i

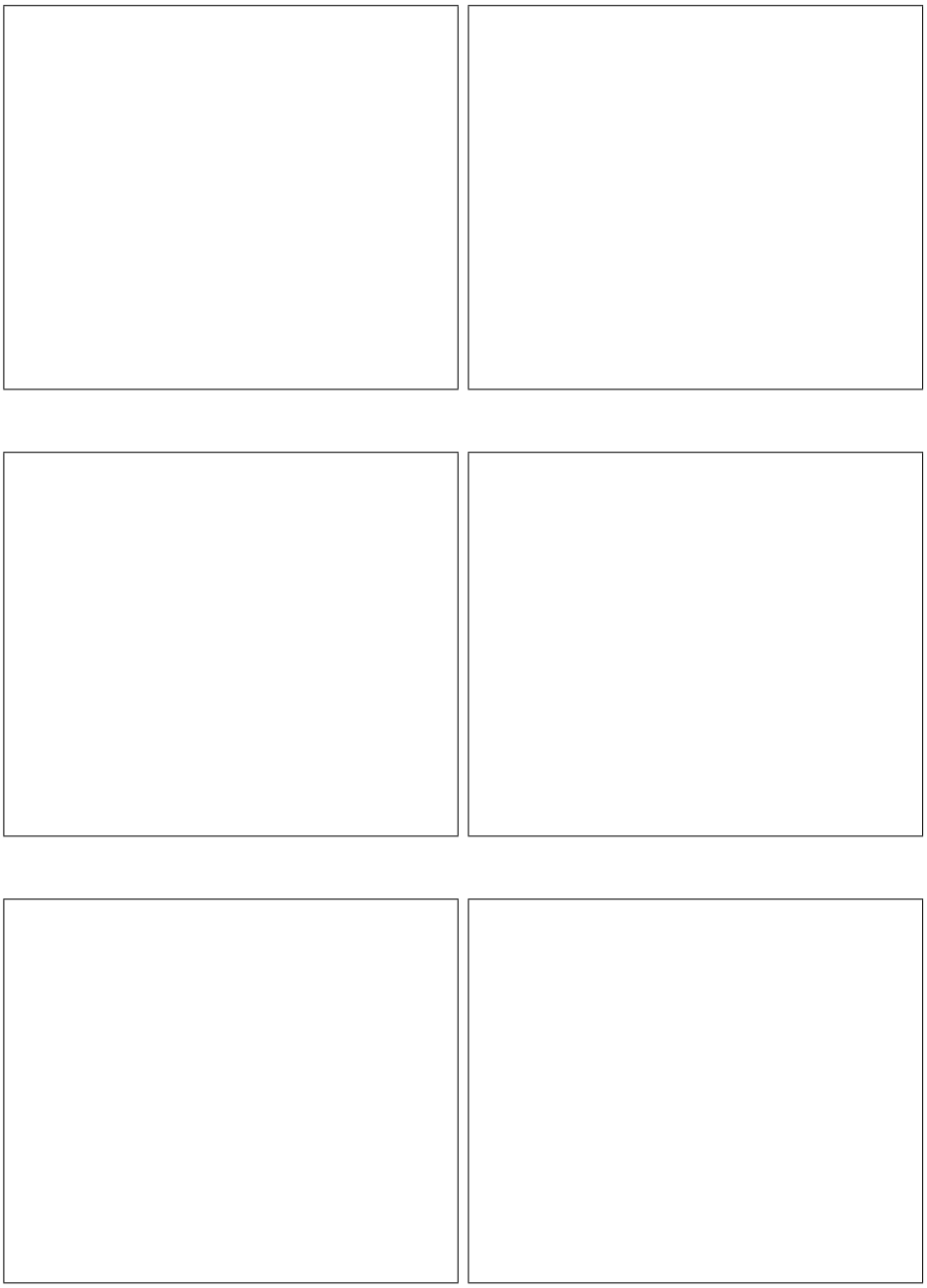

B.1.6 m = 1.81+0.48i

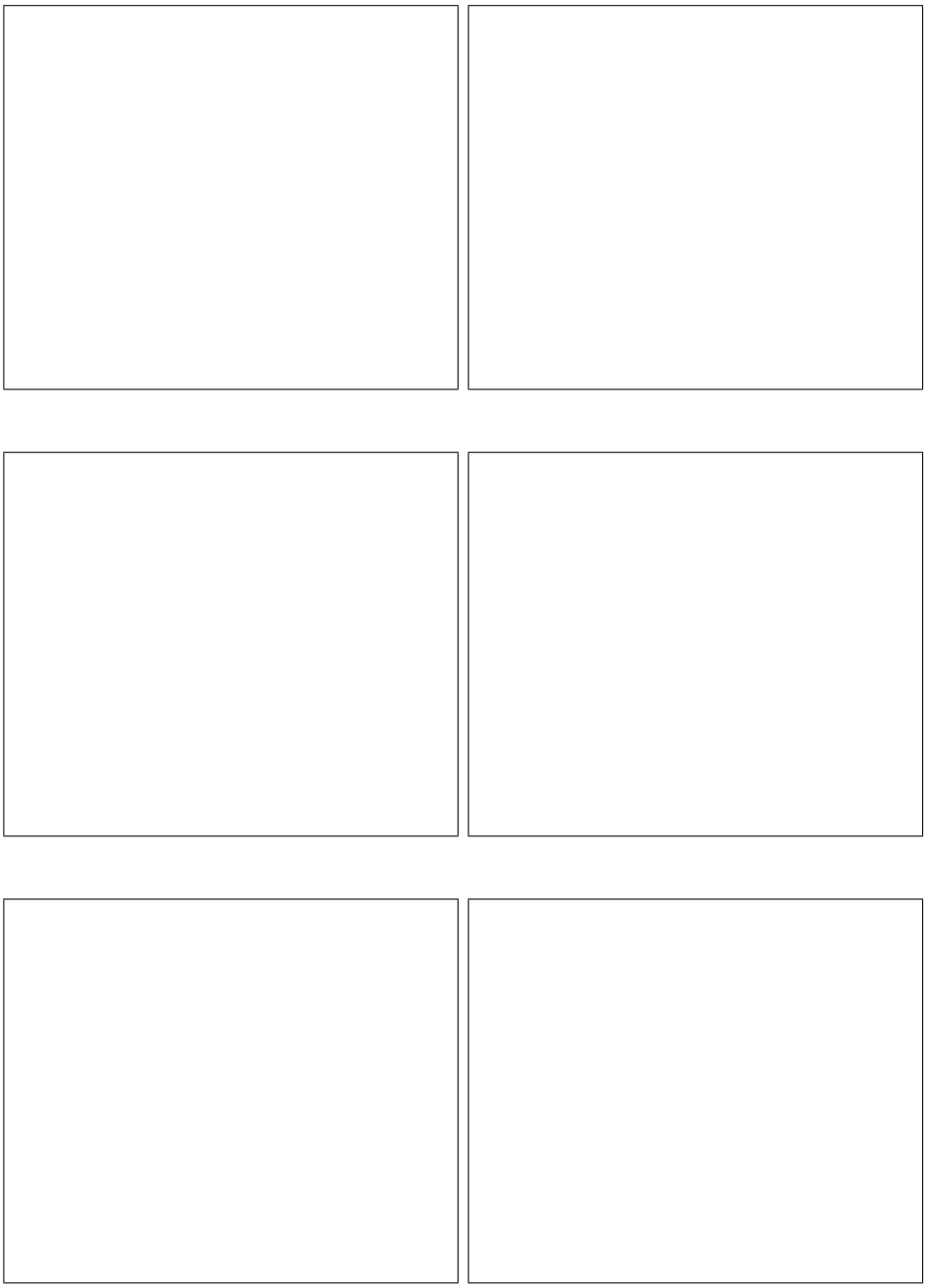

B.1.7 m = 2.5+1.4i

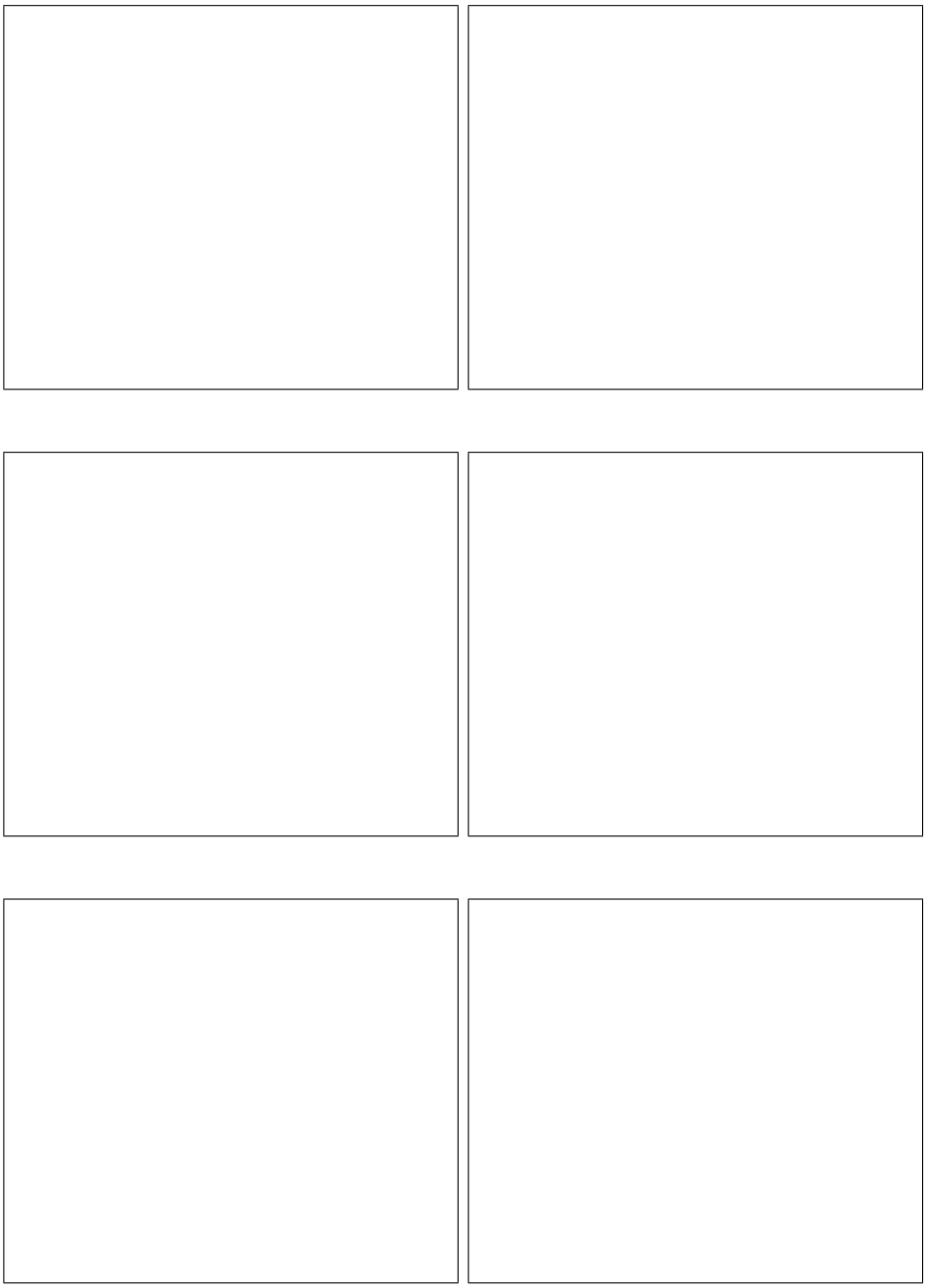

B.1.8 m = 3.05+0.33i

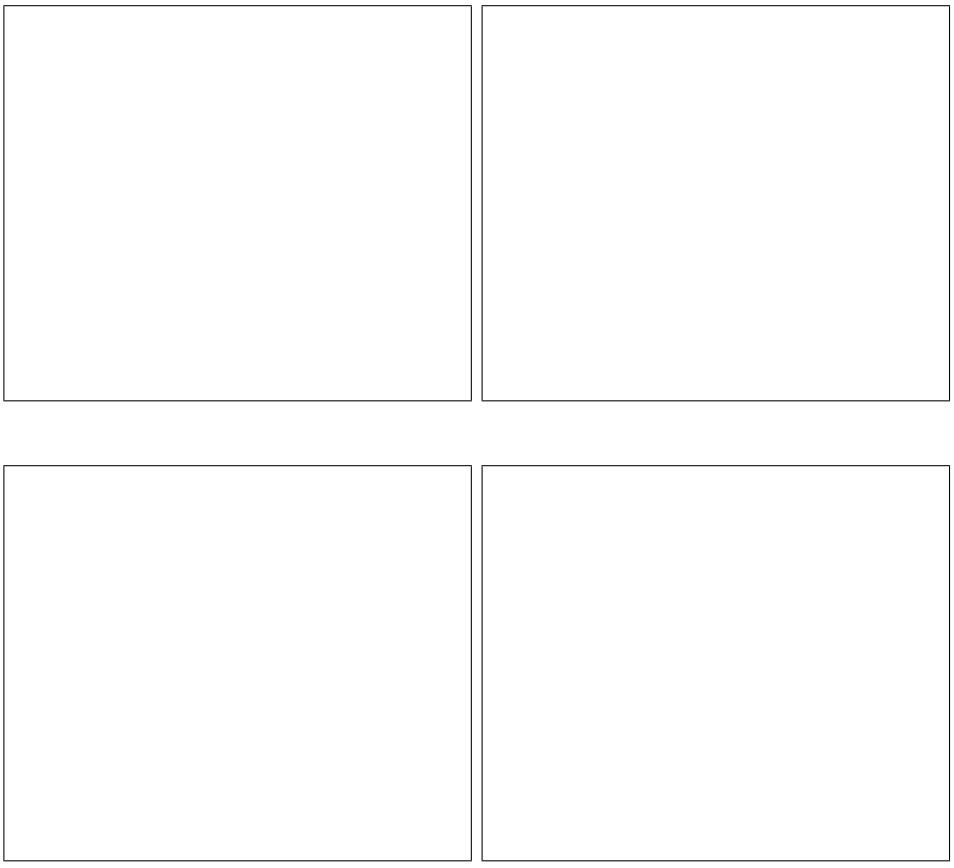

B.2 Errors vs. Real part of the refractive index : Spherical particles

B.2.1 Mie-error in Direct Extinction, Absorption and Scattering Coefficient

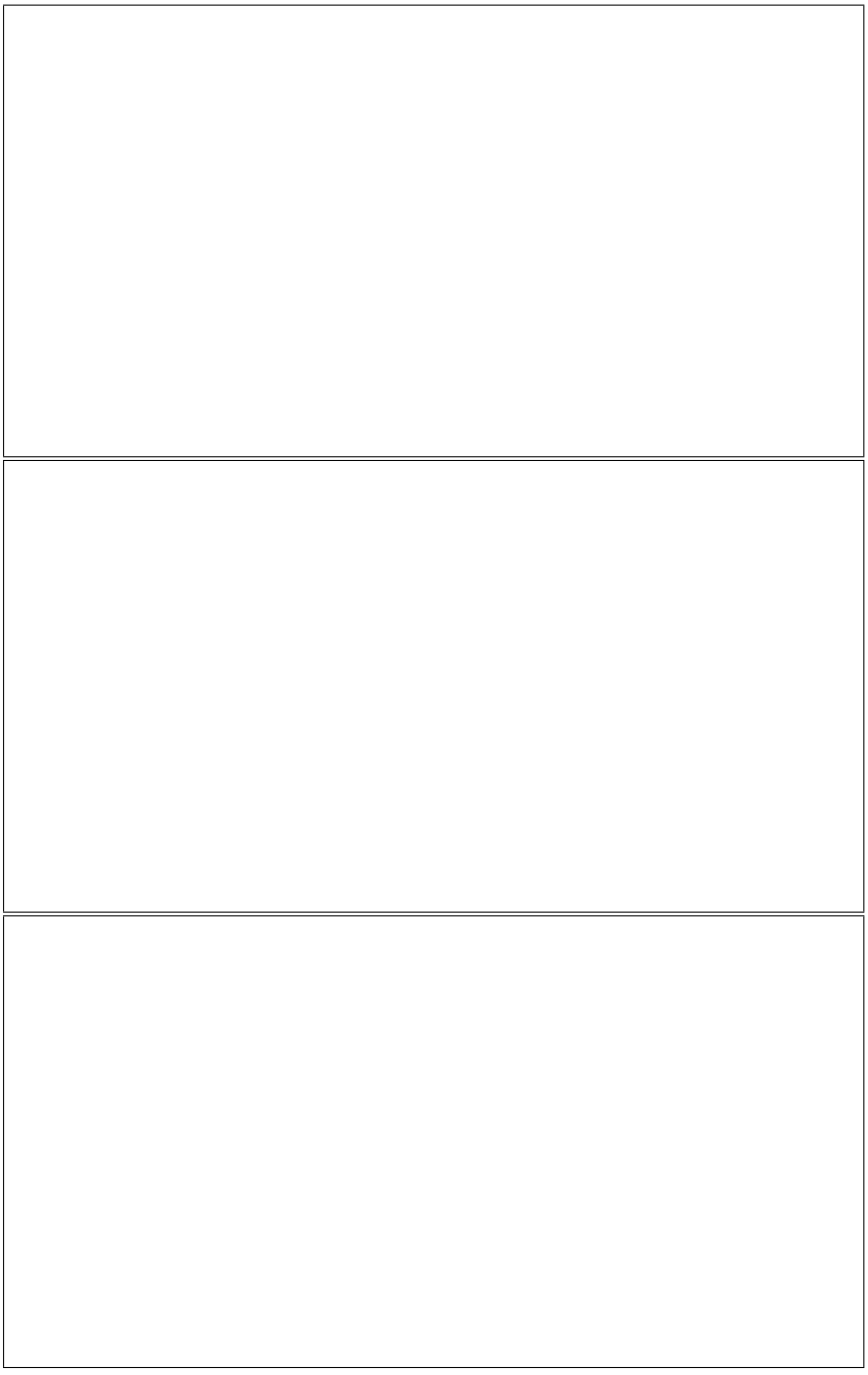

B.2.2 Mie-error in Integrated Scattering Coefficient

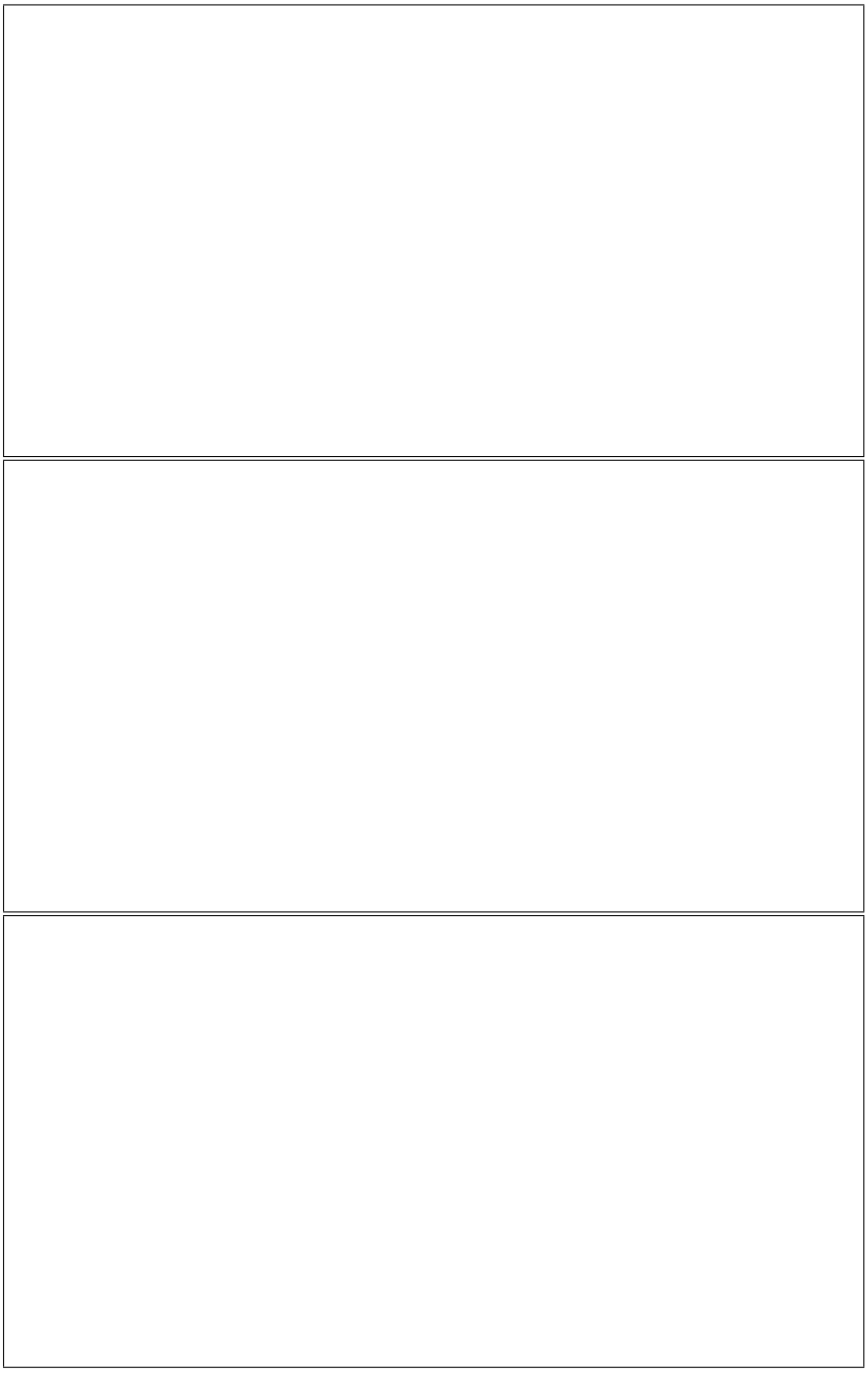

B.2.3 Modelling error in Scattering Coefficient

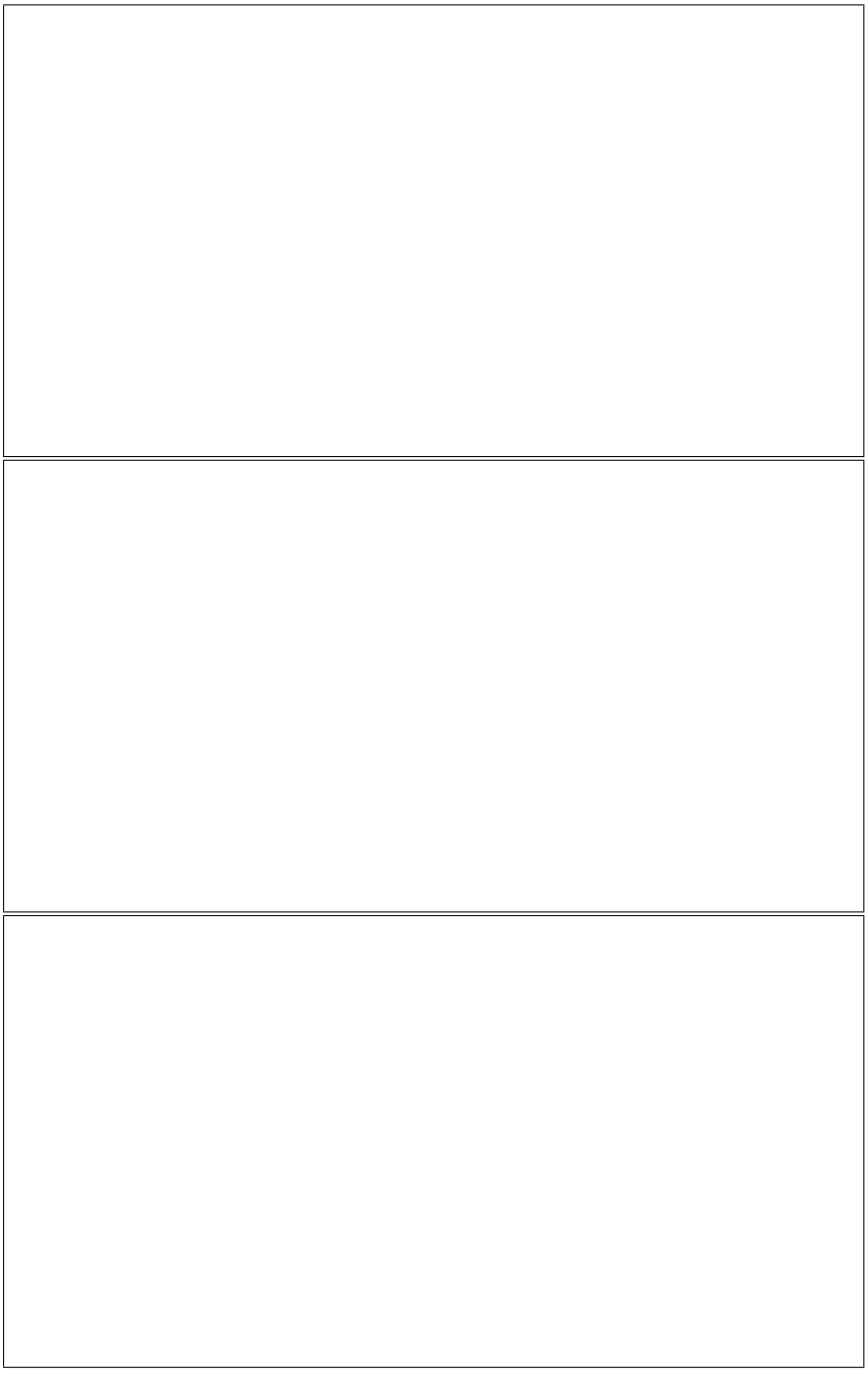

B.2.4 Mie-error in the Integrated Scattering force

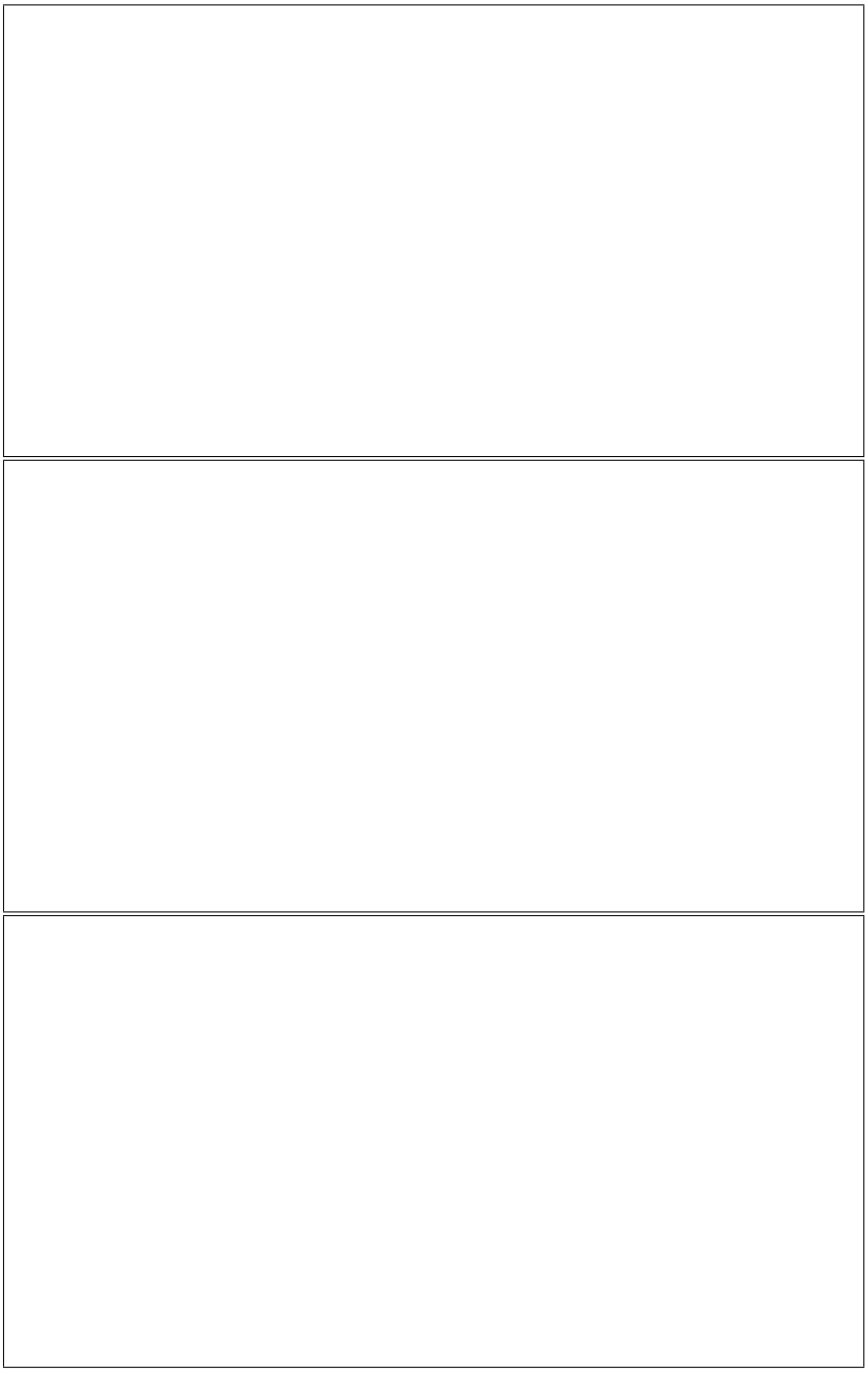

B.2.5 Mie-error in Integrated Radiation Pressure cross-section

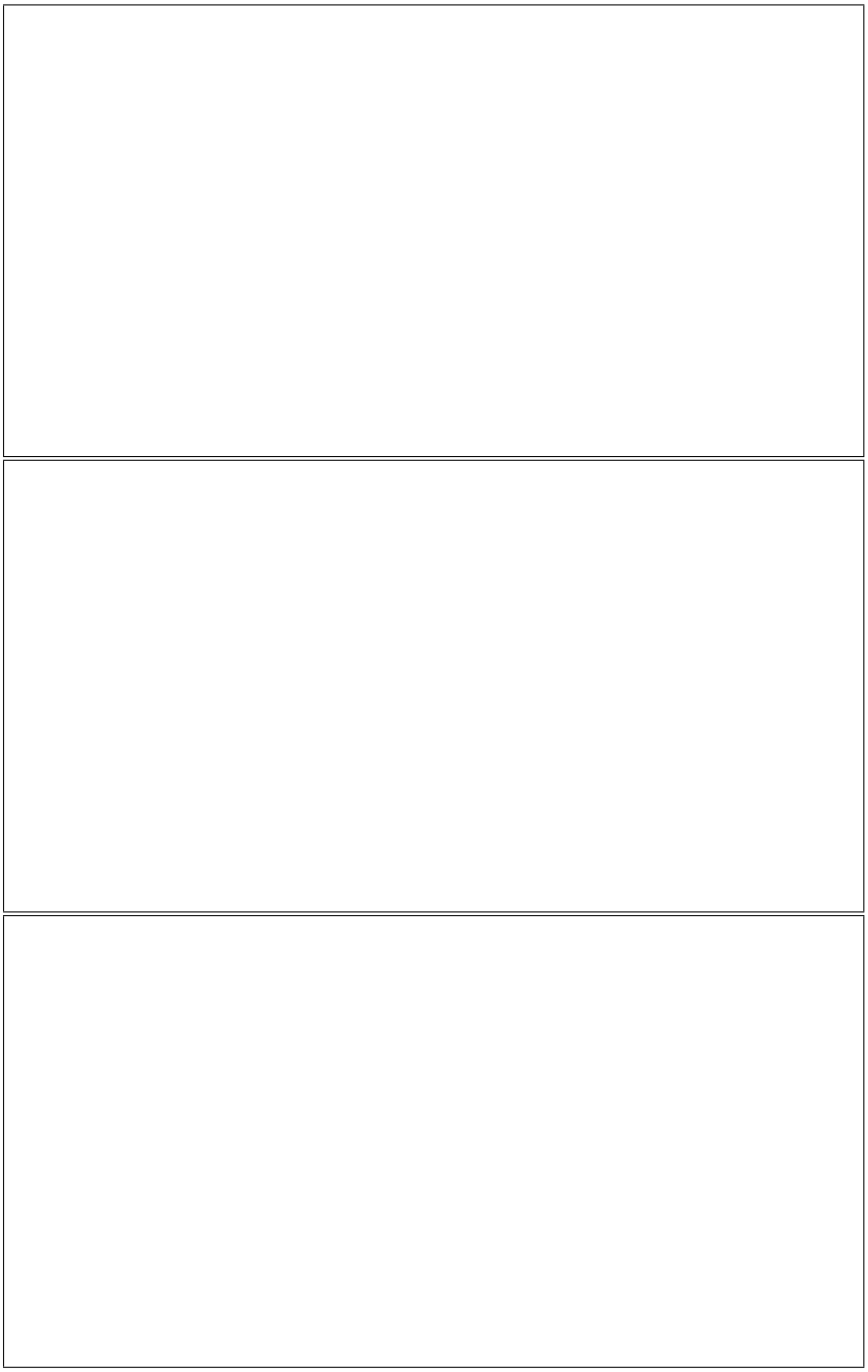

B.2.6 Modelling error in Radiation Pressure cross-section

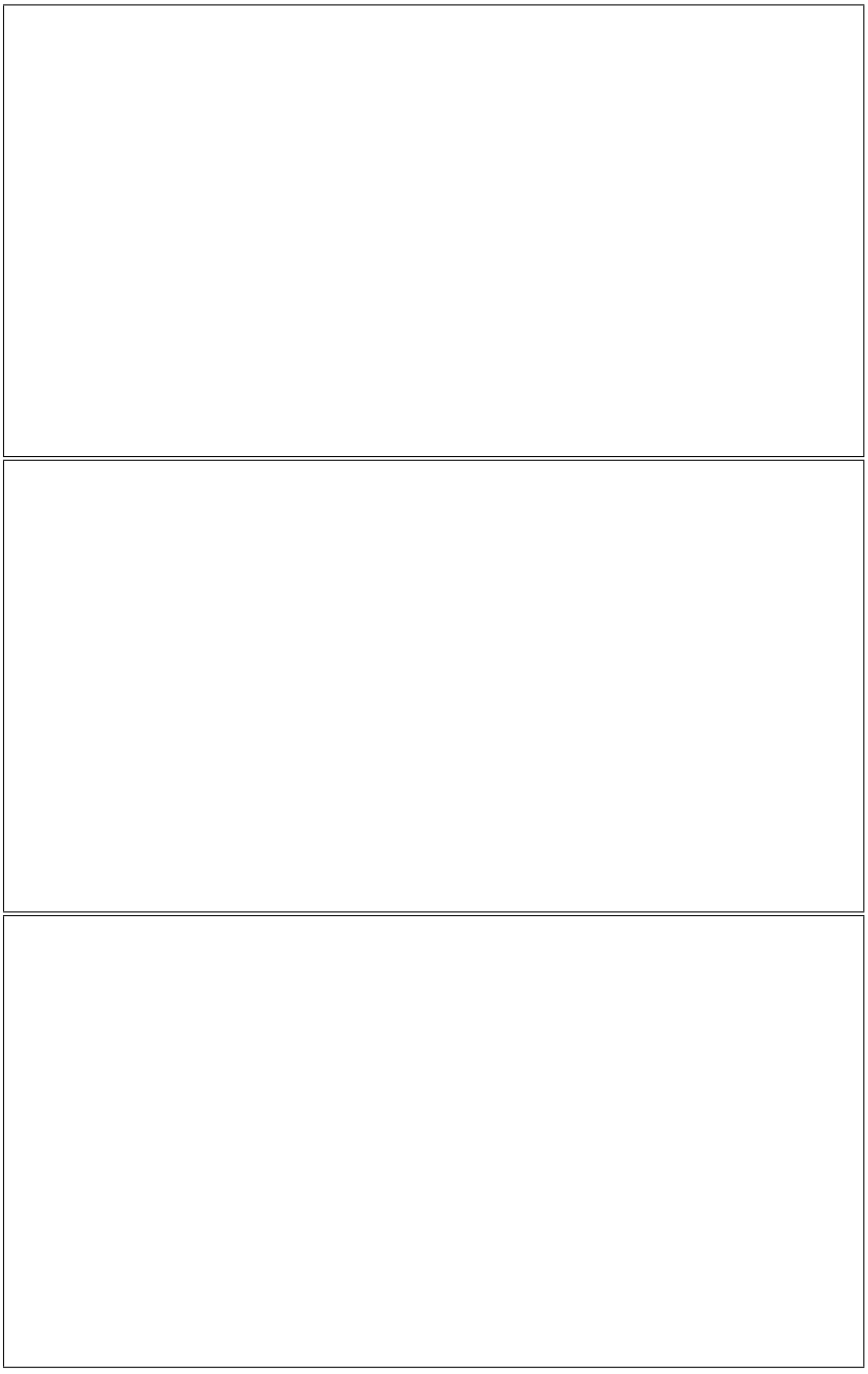

B.3 Errors vs. Imaginary part of the refractive index : Spherical particles

B.3.1 Mie-error in Direct Extinction, Absorption and Scattering Coefficient

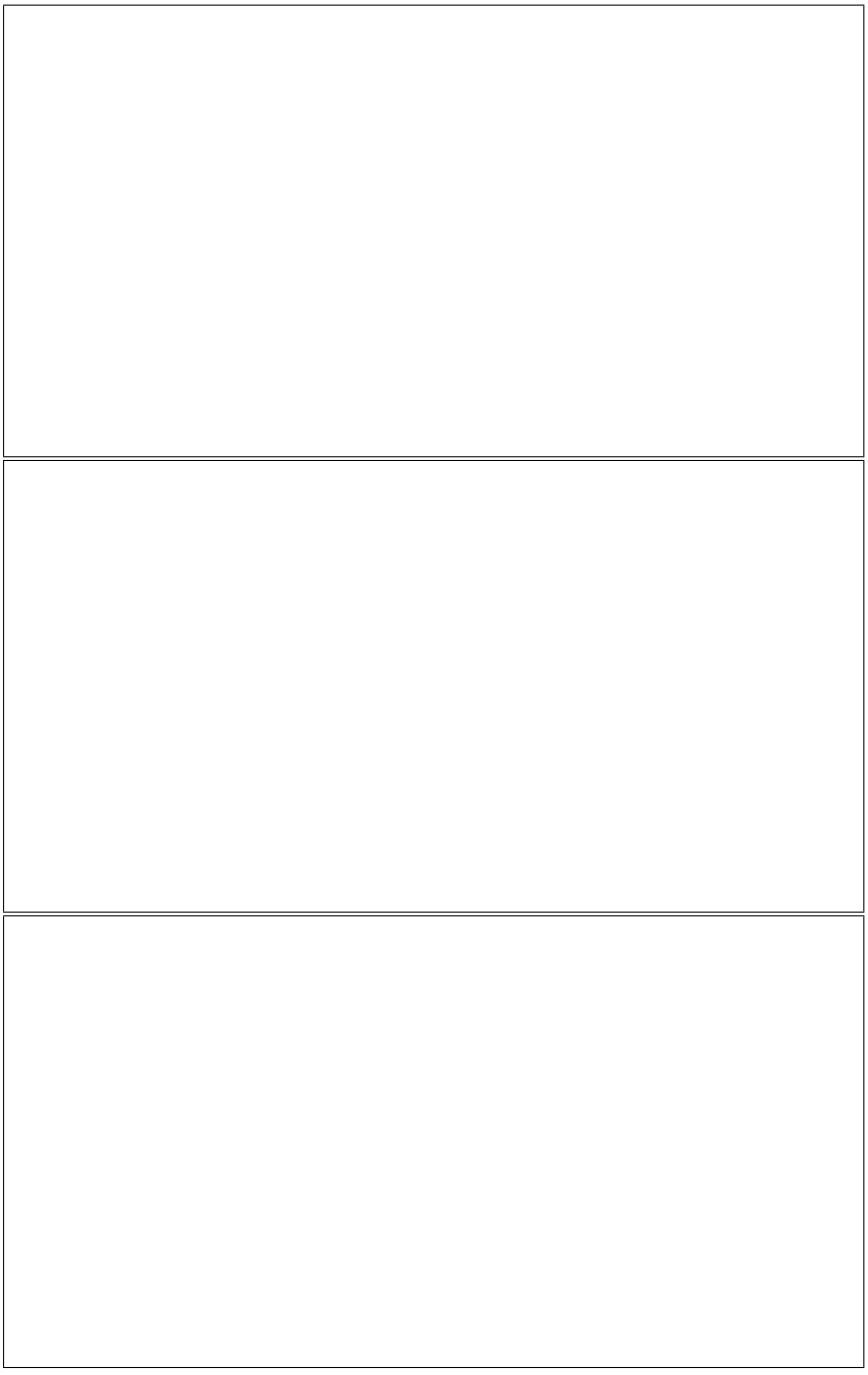

B.3.2 Mie-error in Scattering Coefficient

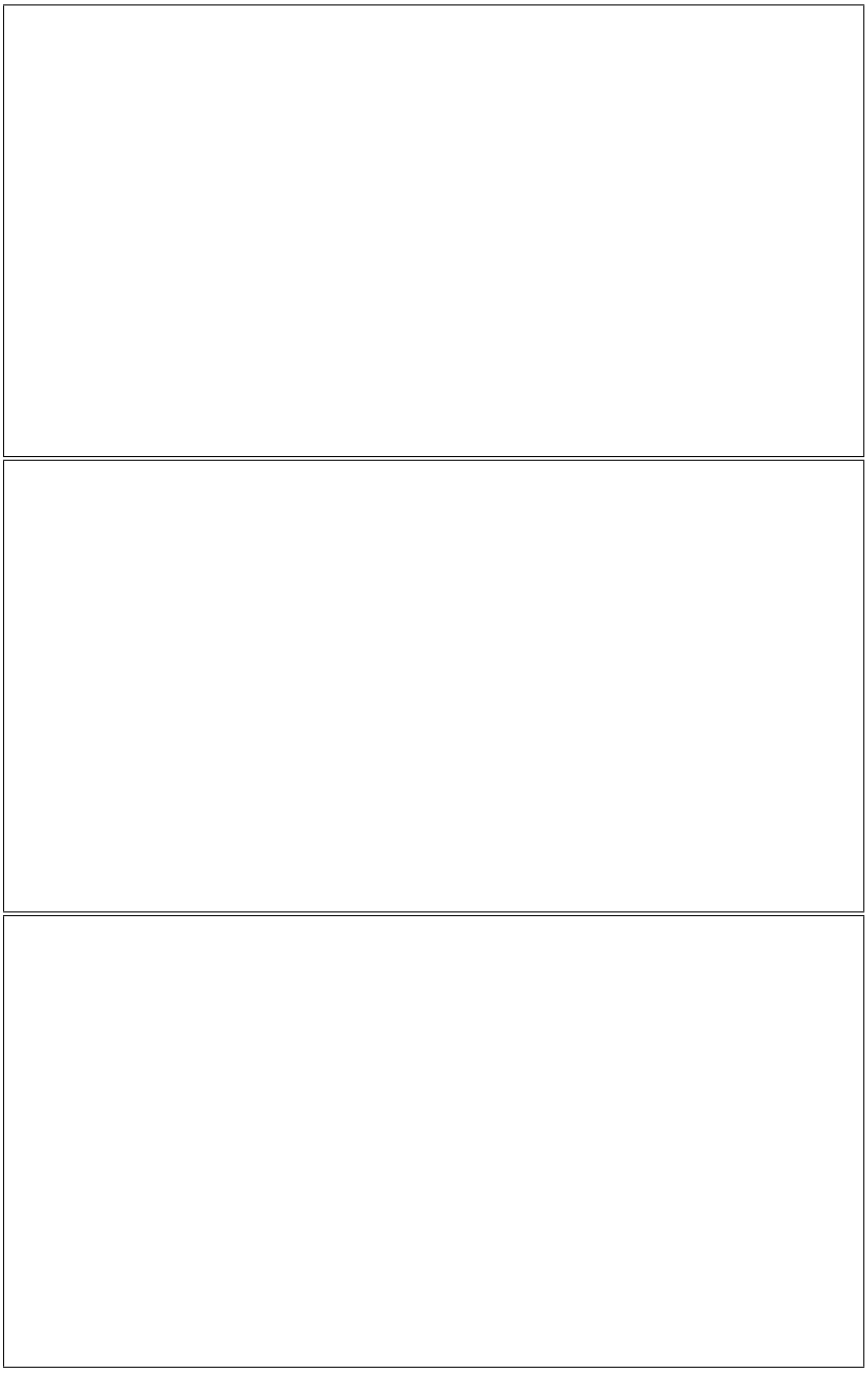

B.3.3 Modelling error in Scattering Coefficient

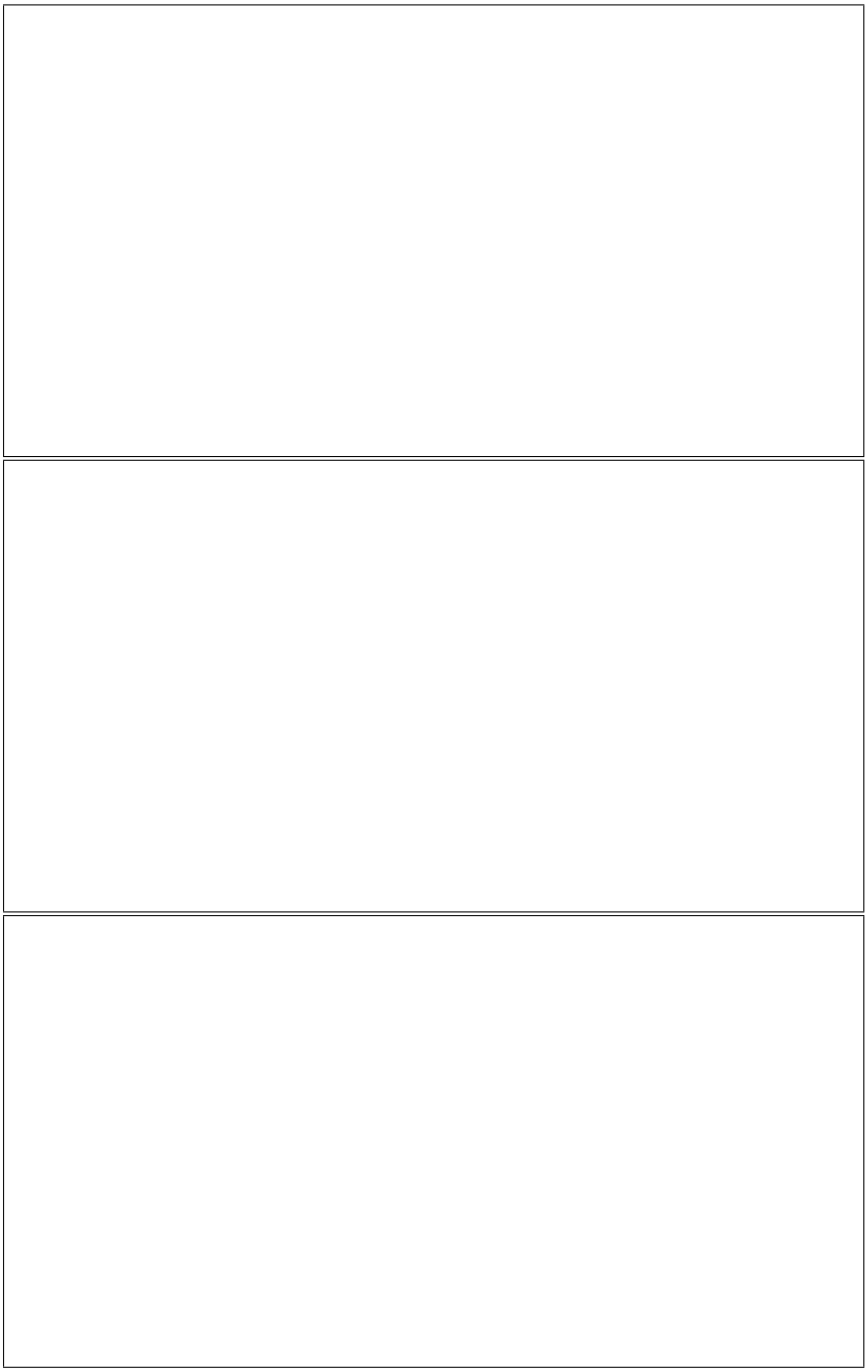

B.3.4 Mie-error in the Scattering force

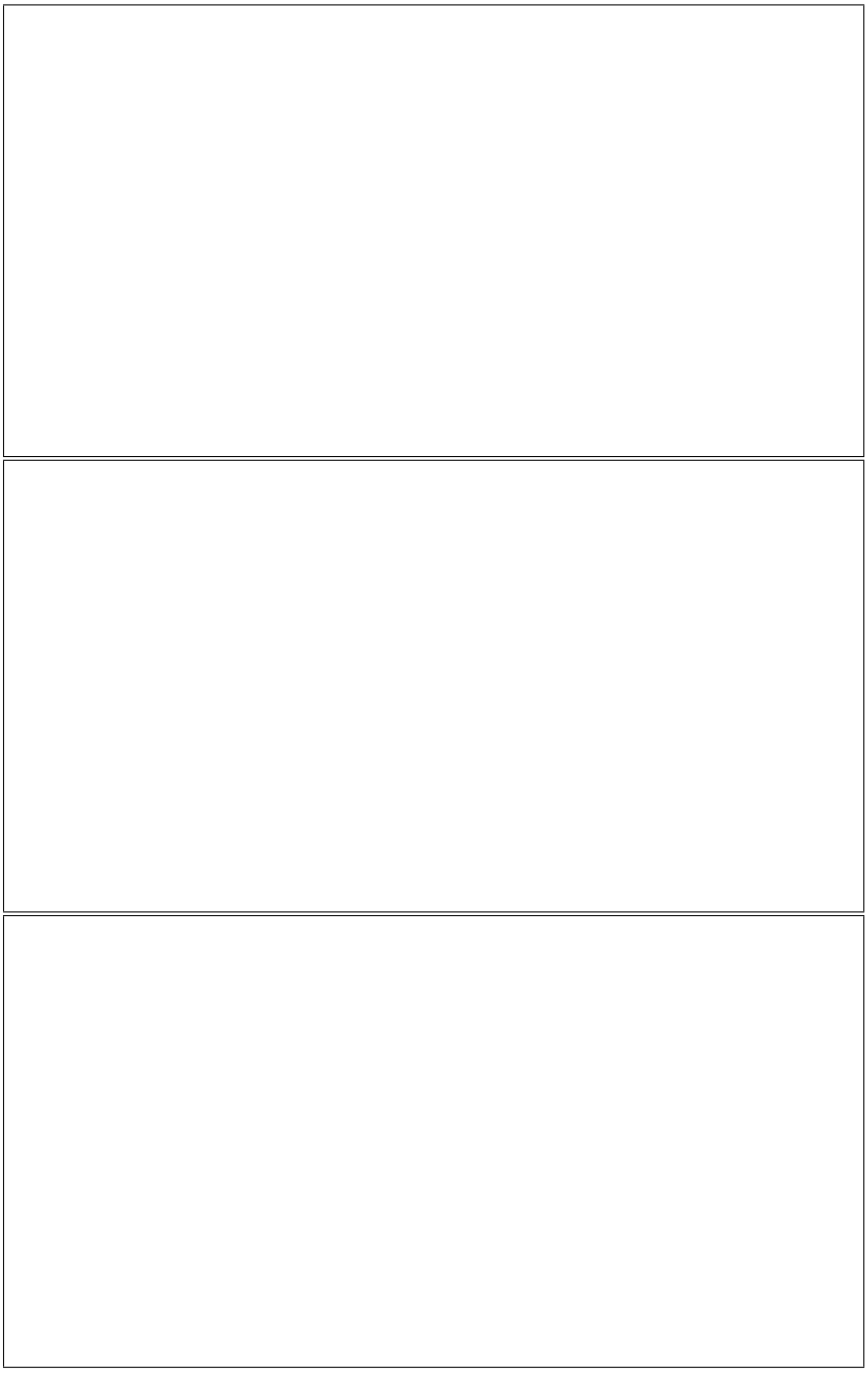

B.3.5 Mie-error in Radiation Pressure cross-section

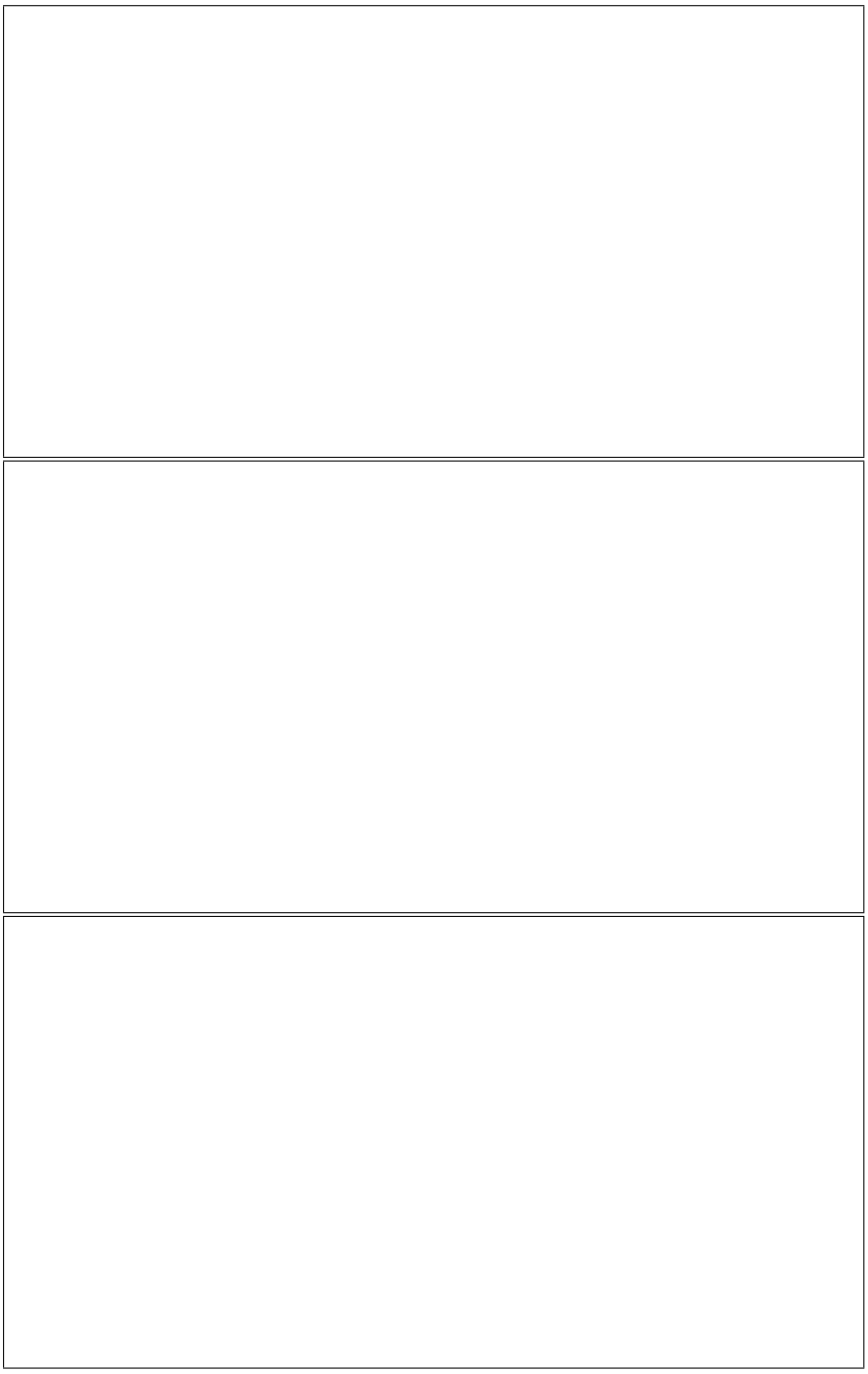

B.3.6 Modelling error in Radiation Pressure cross-section

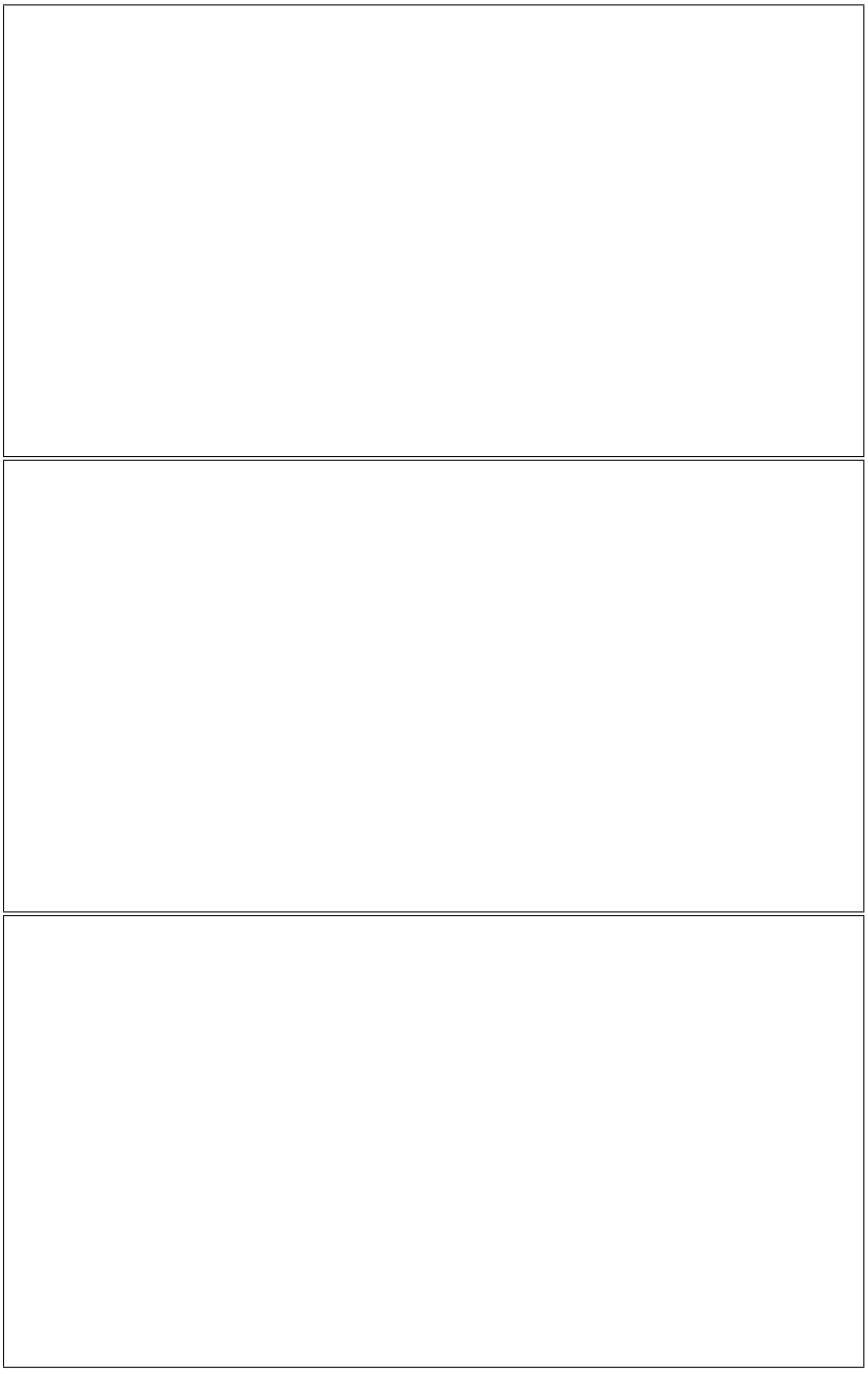

Appendix C

Raw Numbers : Spherical particles

C.1 DDA input-parameters

m	$\frac{\#\text{dip}}{\lambda}$	box-size	#dip in sphere	#CG-iterations
1.05	15	12	912	6
$1.14 + 0.38i$				11
$1.33 + 0.01i$				19
$1.68 + 0.03i$	20	16	2176	46
$1.7 + 0.156i$				37
$1.81 + 0.48i$				37
$2.5 + 1.4i$	30	24	7208	72
$3.05 + 0.33i$	40	32	17256	266

Table C.1: $x = 2.5$

m	$\frac{\#\text{dip}}{\lambda}$	box-size	#dip in sphere	#CG-iterations
1.05	15	24	7208	8
$1.14 + 0.38i$				21
$1.33 + 0.01i$				39
$1.68 + 0.03i$	20	32	17256	160
$1.7 + 0.156i$				102
$1.81 + 0.48i$				70
$2.5 + 1.4i$	30	48	57856	132
$3.05 + 0.33i$	40	64	137376	497

Table C.2: $x = 5$

m	$\frac{\#\text{dip}}{\lambda}$	box-size	#dip in sphere	#CG-iterations
1.05	15	48	57856	13
$1.14 + 0.38i$				40
$1.33 + 0.01i$				125
$1.68 + 0.03i$	20	64	137376	716
$1.7 + 0.156i$				233
$1.81 + 0.48i$				145
$2.5 + 1.4i$	30	96	436400	277

Table C.3: $x = 10$

C.2 Raw data

In the table headings in this appendix the names $F_{sca,x}$, $F_{sca,y}$ and $F_{sca,z}$ will be used heavily. The printed numbers are not the actual forces but $8\pi F_{sca,x}/\vec{E}_{inc}^2$, $8\pi F_{sca,y}/\vec{E}_{inc}^2$ and $8\pi F_{sca,z}/\vec{E}_{inc}^2$ respectively.

C.2.1 m = 1.05
x = 2.51994

Quantity	Mie-value
Q_{ext}	0.024771
Q_{sca}	0.024771
g_z	0.751806
Q_{pr}	0.006148

Table C.4: Mie-values

	Cross-section	Efficiency
Extinction	0.49377	0.02475
Absorption	-6.84086e-10	-3.42909e-11
Scattering	0.49377	0.02475

Table C.5: Direct DDA

Res	C_{sca} (conv.)	Q_{sca}
4	0.49023 (7.742e-05)	0.02457
5	0.49213 (1.48053e-05)	0.02467
6	0.49295 (1.62086e-06)	0.02471
7	0.49336 (2.02542e-07)	0.02473
8	0.49357 (2.53261e-08)	0.02474

Res	$-F_{sca,x}$ (conv.)	$-F_{sca,y}$ (conv.)
4	0.02815 (0.00054)	5.37808e-09 (0.00348)
5	0.01414 (3.35795e-05)	2.19918e-09 (0.00121)
6	0.00709 (4.258e-06)	2.12642e-09 (0.00052)
7	0.00355 (5.3019e-07)	1.53124e-09 (0.00011)
8	0.00178 (6.61511e-08)	1.57986e-09 (3.03485e-05)

Res	$-F_{sca,z}$ (conv.)
4	0.37126 (0.00045)
5	0.37166 (3.95467e-06)
6	0.37166 (8.64701e-09)
7	0.37166 (1e-09)
8	0.37166 (1e-09)

Table C.6: Integrated DDA

C.2.2 m = 1.05
x = 5.01954

Quantity	Mie-value
Q_{ext}	0.119193
Q_{sca}	0.119193
g_z	0.908937
Q_{pr}	0.010854

Table C.7: Mie-values

	Cross-section	Efficiency
Extinction	9.44194	0.11928
Absorption	-5.517e-09	-6.96988e-11
Scattering	9.44194	0.11928

Table C.8: Direct DDA

Res	C_{sca} (conv.)	Q_{sca}
4	9.42155 (0.00214)	0.11903
5	9.439 (7.0198e-06)	0.11925
6	9.44194 (1.87847e-07)	0.11927
7	9.44137 (1.43755e-08)	0.11928
8	9.44165 (1.81862e-09)	0.11928

Res	$-F_{sca,x}$ (conv.)	$-F_{sca,y}$ (conv.)
4	0.26957 (0.00596)	1.04189e-07 (0.00048)
5	0.1378 (0.0001)	9.12076e-08 (0.00061)
6	0.06884 (6.65764e-08)	5.58974e-08 (0.00071)
7	0.03442 (5.637e-08)	4.11783e-08 (4.61392e-05)
8	0.01721 (7.11368e-09)	1.97213e-08 (9.60308e-05)

Res	$-F_{sca,z}$ (conv.)
4	8.58811 (0.00183)
5	8.57686 (5.22551e-06)
6	8.57816 (1.48829e-07)
7	8.57815 (1e-09)
8	8.57815 (1e-09)

Table C.9: Integrated DDA

C.2.3 m = 1.05
x = 10.0502

Quantity	Mie-value
Q_{ext}	0.488248
Q_{sca}	0.488248
g_z	0.969948
Q_{pr}	0.014673

Table C.10: Mie-values

	Cross-section	Efficiency
Extinction	154.924	0.48822
Absorption	-4.47582e-08	-1.41049e-10
Scattering	154.924	0.48822

Table C.11: Direct DDA

Res	C_{sca} (conv.)	Q_{sca}
4	181.53 (0.0145)	0.57207
5	154.169 (0.00069)	0.48585
6	154.908 (4.65725e-06)	0.48817
7	154.917 (1.36341e-08)	0.4882
8	154.92 (1.51599e-09)	0.4882

Res	$-F_{sca,x}$ (conv.)	$-F_{sca,y}$ (conv.)
4	3.23191 (0.01346)	1.29621e-06 (0.00855)
5	1.14127 (0.0016)	6.37116e-07 (0.00031)
6	0.58629 (2.70036e-05)	2.49528e-07 (0.00133)
7	0.29307 (1e-09)	6.35689e-07 (0.00017)
8	0.14656 (1.30359e-08)	7.13795e-07 (6.09368e-06)

Res	$-F_{sca,z}$ (conv.)
4	175.38 (0.01459)
5	149.667 (0.00067)
6	150.254 (3.81588e-06)
7	150.258 (6.04181e-09)
8	150.258 (1e-09)

Table C.12: Integrated DDA

C.2.4 m = 1.14 + 0.38i
x = 2.51994

Quantity	Mie-value
Q_{ext}	1.76346
Q_{sca}	0.546803
g_z	0.755954
Q_{pr}	1.3501

Table C.13: Mie-values

	Cross-section	Efficiency
Extinction	35.2668	1.76781
Absorption	24.3687	1.22152
Scattering	10.8981	0.54629

Table C.14: Direct DDA

Res	C_{sca} (conv.)	Q_{sca}
4	10.8422 (0.0003)	0.54348
5	10.8753 (1.14984e-05)	0.5451
6	10.8867 (1.02063e-06)	0.54571
7	10.8924 (1.28131e-07)	0.546
8	10.8953 (1.60058e-08)	0.54614

Res	$-F_{sca,x}$ (conv.)	$-F_{sca,y}$ (conv.)
4	0.57847 (0.0004)	1.80285e-07 (0.00156)
5	0.2891 (1.37209e-05)	8.7656e-08 (0.00156)
6	0.14468 (1.78171e-06)	7.00047e-08 (0.00016)
7	0.07239 (2.22169e-07)	9.01538e-08 (6.13436e-05)
8	0.03621 (2.77568e-08)	2.94377e-08 (1.72176e-05)

Res	$-F_{sca,z}$ (conv.)
4	8.26455 (0.00073)
5	8.27904 (6.49422e-06)
6	8.27892 (1.40821e-08)
7	8.27892 (1e-09)
8	8.27892 (1e-09)

Table C.15: Integrated DDA

C.2.5 m = 1.14 + 0.38i
x = 5.01954

Quantity	Mie-value
Q_{ext}	2.13525
Q_{sca}	0.90648
g_z	0.889992
Q_{pr}	1.32849

Table C.16: Mie-values

	Cross-section	Efficiency
Extinction	168.845	2.1331
Absorption	97.2676	1.22883
Scattering	71.5777	0.90427

Table C.17: Direct DDA

Res	C_{sca} (conv.)	Q_{sca}
4	72.0047 (0.00069)	0.90967
5	71.4397 (3.12743e-05)	0.90253
6	71.522 (1.12713e-06)	0.90357
7	71.5499 (9.50292e-08)	0.90392
8	71.5639 (1.19837e-08)	0.9041

Res	$-F_{sca,x}$ (conv.)	$-F_{sca,y}$ (conv.)
4	2.12916 (0.00571)	1.48463e-06 (0.00807)
5	1.09465 (0.00012)	7.19215e-07 (0.00066)
6	0.54849 (3.02595e-06)	1.16483e-06 (0.00015)
7	0.27465 (4.23414e-07)	1.08877e-06 (3.32902e-05)
8	0.13744 (5.27771e-08)	1.15979e-06 (6.86203e-06)

Res	$-F_{sca,z}$ (conv.)
4	64.6807 (0.00023)
5	63.7467 (5.74976e-05)
6	63.7805 (5.18239e-07)
7	63.7802 (1e-09)
8	63.7802 (1e-09)

Table C.18: Integrated DDA

C.2.6 m = 1.14 + 0.38i
x = 10.0502

Quantity	Mie-value
Q_{ext}	2.20555
Q_{sca}	1.06837
g_z	0.930602
Q_{pr}	1.21132

Table C.19: Mie-values

	Cross-section	Efficiency
Extinction	699.538	2.2045
Absorption	361.028	1.13774
Scattering	338.51	1.06676

Table C.20: Direct DDA

Res	C_{sca} (conv.)	Q_{sca}
4	362.904 (0.01374)	1.14364
5	340.252 (0.00026)	1.07226
6	338.18 (5.99567e-06)	1.06573
7	338.392 (1.53507e-07)	1.0664
8	338.451 (1.06573e-08)	1.06659

Res	$-F_{sca,x}$ (conv.)	$-F_{sca,y}$ (conv.)
4	8.2973 (0.00988)	-3.42784e-06 (0.0129)
5	3.35069 (0.00091)	-3.25753e-06 (0.00137)
6	1.70966 (2.0534e-05)	-3.19076e-06 (7.96573e-05)
7	0.85662 (5.71209e-07)	-3.26184e-06 (2.96599e-05)
8	0.42884 (7.89414e-08)	-3.39118e-06 (6.27089e-06)

Res	$-F_{sca,z}$ (conv.)
4	338.998 (0.01443)
5	317.717 (0.00026)
6	315.203 (7.78662e-06)
7	315.302 (7.68237e-08)
8	315.302 (1e-09)

Table C.21: Integrated DDA

C.2.7 m = 1.33 + 0.01i
x = 2.51994

Quantity	Mie-value
Q_{ext}	1.27094
Q_{sca}	1.17828
g_z	0.710664
Q_{pr}	0.433581

Table C.22: Mie-values

	Cross-section	Efficiency
Extinction	25.2105	1.26372
Absorption	1.8354	0.092
Scattering	23.3751	1.17172

Table C.23: Direct DDA

Res	C_{sca} (conv.)	Q_{sca}
4	23.2253 (0.00011)	1.16421
5	23.3066 (1.3426e-05)	1.16828
6	23.3408 (1.43188e-06)	1.17
7	23.3579 (1.7901e-07)	1.17085
8	23.3665 (2.23729e-08)	1.17128

Res	$-F_{sca,x}$ (conv.)	$-F_{sca,y}$ (conv.)
4	1.13422 (0.00041)	5.37229e-07 (0.00034)
5	0.56657 (1.15808e-05)	3.68656e-07 (0.00042)
6	0.28346 (1.54943e-06)	3.23219e-07 (9.96699e-05)
7	0.14181 (1.93471e-07)	2.9058e-07 (6.79699e-05)
8	0.07093 (2.41415e-08)	2.74588e-07 (5.13449e-06)

Res	$-F_{sca,z}$ (conv.)
4	16.6547 (0.00051)
5	16.6747 (4.48661e-06)
6	16.6745 (9.5191e-09)
7	16.6745 (1e-09)
8	16.6745 (1e-09)

Table C.24: Integrated DDA

C.2.8 m = 1.33 + 0.01i
x = 5.01954

Quantity	Mie-value
Q_{ext}	3.49011
Q_{sca}	3.29449
g_z	0.852981
Q_{pr}	0.679971

Table C.25: Mie-values

	Cross-section	Efficiency
Extinction	276.955	3.4989
Absorption	15.4418	0.19508
Scattering	261.514	3.30382

Table C.26: Direct DDA

Res	C_{sca} (conv.)	Q_{sca}
4	261.42 (0.00106)	3.30264
5	260.835 (8.9958e-06)	3.29525
6	261.203 (1.37859e-06)	3.2999
7	261.358 (1.44831e-07)	3.30186
8	261.436 (1.81687e-08)	3.30284

Res	$-F_{sca,x}$ (conv.)	$-F_{sca,y}$ (conv.)
4	7.00737 (0.00498)	1.09921e-05 (0.00723)
5	3.5978 (0.00012)	1.00892e-05 (3.17901e-05)
6	1.80404 (3.73196e-06)	9.07789e-06 (1.83252e-05)
7	0.90368 (5.06337e-07)	1.01274e-05 (4.67748e-06)
8	0.45229 (6.31453e-08)	1.00164e-05 (2.5644e-06)

Res	$-F_{sca,z}$ (conv.)
4	225.36 (0.00084)
5	223.467 (3.32399e-05)
6	223.542 (3.29266e-07)
7	223.542 (1e-09)
8	223.542 (1e-09)

Table C.27: Integrated DDA

C.2.9 m = 1.33 + 0.01i
x = 10.0502

Quantity	Mie-value
Q_{ext}	2.21083
Q_{sca}	1.83546
g_z	0.75357
Q_{pr}	0.827681

Table C.28: Mie-values

	Cross-section	Efficiency
Extinction	704.94	2.22153
Absorption	118.993	0.37499
Scattering	585.948	1.84654

Table C.29: Direct DDA

Res	C_{sca} (conv.)	Q_{sca}
4	479.701 (0.00317)	1.51172
5	596.913 (0.00076)	1.8811
6	584.587 (2.05985e-05)	1.84225
7	585.429 (3.51197e-07)	1.8449
8	585.687 (2.69143e-08)	1.84572

Res	$-F_{sca,x}$ (conv.)	$-F_{sca,y}$ (conv.)
4	15.346 (0.00618)	6.50252e-05 (0.00775)
5	8.6059 (0.00044)	7.78566e-05 (0.00086)
6	4.27163 (6.21146e-06)	7.15877e-05 (3.04437e-05)
7	2.1365 (1.31557e-07)	7.18547e-05 (7.8116e-06)
8	1.06846 (1.30347e-08)	7.77523e-05 (1.97002e-06)

Res	$-F_{sca,z}$ (conv.)
4	340.203 (0.00462)
5	454.887 (0.00099)
6	441.513 (2.95823e-05)
7	441.836 (1.78548e-07)
8	441.835 (1e-09)

Table C.30: Integrated DDA

C.2.10 m = 1.68 + 0.03i
x = 2.52546

Quantity	Mie-value
Q_{ext}	4.13589
Q_{sca}	3.72906
g_z	0.698795
Q_{pr}	1.53004

Table C.31: Mie-values

	Cross-section	Efficiency
Extinction	83.1795	4.15132
Absorption	8.0025	0.39939
Scattering	75.177	3.75193

Table C.32: Direct DDA

Res	C_{sca} (conv.)	Q_{sca}
4	74.2716 (0.00014)	3.70675
5	74.7512 (2.50849e-05)	3.73068
6	74.9641 (2.77363e-06)	3.74131
7	75.0705 (3.46227e-07)	3.74662
8	75.1238 (4.32445e-08)	3.74928

Res	$-F_{sca,x}$ (conv.)	$-F_{sca,y}$ (conv.)
4	2.87104 (0.00048)	2.71261e-06 (0.00066)
5	1.44089 (2.98042e-05)	2.49835e-06 (13)
6	0.72249 (3.71408e-06)	2.54929e-06 (1.06258e-05)
7	0.36184 (4.62978e-07)	2.56951e-06 (2.72319e-05)
8	0.18108 (5.77876e-08)	2.42661e-06 (8.38604e-06)

Res	$-F_{sca,z}$ (conv.)
4	53.06 (0.00066)
5	53.137 (5.62084e-06)
6	53.1363 (1.17085e-08)
7	53.1363 (1e-09)
8	53.1363 (1e-09)

Table C.33: Integrated DDA

C.2.11 m = 1.68 + 0.03i
x = 5.03617

Quantity	Mie-value
Q_{ext}	2.17025
Q_{sca}	1.52516
g_z	0.495933
Q_{pr}	1.41388

Table C.34: Mie-values

	Cross-section	Efficiency
Extinction	173.803	2.18126
Absorption	49.5644	0.62204
Scattering	124.239	1.55922

Table C.35: Direct DDA

Res	C_{sca} (conv.)	Q_{sca}
4	123.975 (0.00431)	1.55591
5	122.172 (5.75921e-05)	1.53328
6	123.258 (8.60883e-06)	1.54691
7	123.748 (9.6651e-07)	1.55306
8	123.993 (1.20694e-07)	1.55614

Res	$-F_{sca,x}$ (conv.)	$-F_{sca,y}$ (conv.)
4	4.48351 (0.00578)	1.14778e-05 (0.00437)
5	2.31198 (0.00013)	1.27007e-05 (0.00018)
6	1.18429 (2.42656e-05)	1.16102e-05 (1.89386e-05)
7	0.59927 (2.95847e-06)	1.25065e-05 (7.24435e-06)
8	0.30144 (3.67456e-07)	1.10523e-05 (2.47521e-07)

Res	$-F_{sca,z}$ (conv.)
4	65.8741 (0.00659)
5	62.461 (0.00021)
6	62.5531 (1.43955e-06)
7	62.5525 (2.40375e-09)
8	62.5525 (1e-09)

Table C.36: Integrated DDA

C.2.12 m = 1.68 + 0.03i
x = 10.056

Quantity	Mie-value
Q_{ext}	2.16995
Q_{sca}	1.33216
g_z	0.788128
Q_{pr}	1.12004

Table C.37: Mie-values

	Cross-section	Efficiency
Extinction	690.188	2.17255
Absorption	264.106	0.83134
Scattering	426.082	1.34121

Table C.38: Direct DDA

Res	C_{sca} (conv.)	Q_{sca}
4	369.193 (0.00273)	1.16213
5	431.686 (0.00056)	1.35885
6	424.478 (1.66261e-05)	1.33616
7	425.388 (5.22605e-07)	1.33902
8	425.732 (4.93887e-08)	1.3401

Res	$-F_{sca,x}$ (conv.)	$-F_{sca,y}$ (conv.)
4	9.62081 (0.01125)	5.70742e-05 (0.00789)
5	6.12646 (0.00085)	7.53558e-05 (0.00063)
6	3.05794 (7.48262e-07)	7.25221e-05 (1.20014e-05)
7	1.53809 (1.49939e-06)	7.49466e-05 (2.35742e-06)
8	0.77133 (1.80624e-07)	7.43216e-05 (9.0996e-08)

Res	$-F_{sca,z}$ (conv.)
4	295.496 (0.00455)
5	345.523 (0.00056)
6	337.572 (2.29938e-05)
7	337.781 (1.50939e-07)
8	337.779 (1e-09)

Table C.39: Integrated DDA

C.2.13 m = 1.7 + 0.156i
x = 2.52546

Quantity	Mie-value
Q_{ext}	3.47295
Q_{sca}	2.29734
g_z	0.733504
Q_{pr}	1.78784

Table C.40: Mie-values

	Cross-section	Efficiency
Extinction	70.8992	3.53844
Absorption	23.6167	1.17866
Scattering	47.2825	2.35978

Table C.41: Direct DDA

Res	C_{sca} (conv.)	Q_{sca}
4	46.8396 (0.00024)	2.33767
5	47.0824 (2.00135e-05)	2.34979
6	47.1824 (2.06958e-06)	2.35478
7	47.2325 (2.58863e-07)	2.35728
8	47.2575 (3.23154e-08)	2.35853

Res	$-F_{sca,x}$ (conv.)	$-F_{sca,y}$ (conv.)
4	1.90524 (0.00036)	2.4868e-06 (0.00473)
5	0.95261 (1.5267e-05)	2.04895e-06 (0.0004)
6	0.47676 (1.8804e-06)	1.87604e-06 (1.60904e-05)
7	0.23855 (2.34936e-07)	1.84633e-06 (2.17093e-05)
8	0.11933 (2.93358e-08)	1.78732e-06 (5.46393e-06)

Res	$-F_{sca,z}$ (conv.)
4	34.9824 (0.00075)
5	35.0422 (6.57816e-06)
6	35.0417 (1.42029e-08)
7	35.0417 (1e-09)
8	35.0417 (1e-09)

Table C.42: Integrated DDA

C.2.14 m = 1.7 + 0.156i
x = 5.03617

Quantity	Mie-value
Q_{ext}	2.5156
Q_{sca}	1.1526
g_z	0.796435
Q_{pr}	1.59763

Table C.43: Mie-values

	Cross-section	Efficiency
Extinction	201.36	2.5271
Absorption	108.444	1.361
Scattering	92.9154	1.1661

Table C.44: Direct DDA

Res	C_{sca} (conv.)	Q_{sca}
4	94.369 (0.00268)	1.18435
5	92.227 (9.11848e-05)	1.15746
6	92.6131 (4.07428e-06)	1.16231
7	92.7641 (3.97424e-07)	1.1642
8	92.8398 (4.98162e-08)	1.16516

Res	$-F_{sca,x}$ (conv.)	$-F_{sca,y}$ (conv.)
4	2.65228 (0.00079)	2.24297e-06 (0.0097)
5	1.35879 (0.00011)	1.83108e-06 (0.00023)
6	0.68798 (1.31231e-05)	1.63193e-06 (5.70268e-05)
7	0.34621 (1.62533e-06)	1.71741e-06 (3.06832e-05)
8	0.17367 (2.02422e-07)	1.39613e-06 (4.34135e-06)

Res	$-F_{sca,z}$ (conv.)
4	76.57 (0.00329)
5	73.5733 (0.00016)
6	73.6669 (1.24189e-06)
7	73.6662 (2.42027e-09)
8	73.6662 (1e-09)

Table C.45: Integrated DDA

C.2.15 m = 1.7 + 0.156i
x = 10.056

Quantity	Mie-value
Q_{ext}	2.38667
Q_{sca}	1.19189
g_z	0.90293
Q_{pr}	1.31047

Table C.46: Mie-values

	Cross-section	Efficiency
Extinction	760.926	2.39522
Absorption	381.271	1.20015
Scattering	379.655	1.19507

Table C.47: Direct DDA

Res	C_{sca} (conv.)	Q_{sca}
4	382.513 (0.01207)	1.20406
5	383.687 (1.37413e-05)	1.20776
6	379.076 (1.19137e-05)	1.19324
7	379.446 (2.38165e-07)	1.19441
8	379.549 (1.6605e-08)	1.19473

Res	$-F_{sca,x}$ (conv.)	$-F_{sca,y}$ (conv.)
4	9.04827 (0.0061)	5.64316e-06 (0.0006)
5	4.0334 (0.00046)	2.73334e-06 (0.00208)
6	2.04573 (1.47984e-05)	4.02304e-06 (5.25643e-05)
7	1.02585 (7.70024e-07)	4.14139e-06 (6.80991e-06)
8	0.51374 (1.00104e-07)	3.85614e-06 (6.92359e-06)

Res	$-F_{sca,z}$ (conv.)
4	347.174 (0.01315)
5	348.4 (1.35379e-05)
6	343.204 (1.47821e-05)
7	343.372 (1.19359e-07)
8	343.371 (1e-09)

Table C.48: Integrated DDA

C.2.16 m = 1.81 + 0.48i
x = 2.52546

Quantity	Mie-value
Q_{ext}	2.9729
Q_{sca}	1.43051
g_z	0.730612
Q_{pr}	1.92775

Table C.49: Mie-values

	Cross-section	Efficiency
Extinction	61.1721	3.05298
Absorption	31.641	1.57914
Scattering	29.5312	1.47384

Table C.50: Direct DDA

Res	C_{sca} (conv.)	Q_{sca}
4	29.2552 (0.00044)	1.46007
5	29.414 (2.07571e-05)	1.46799
6	29.4724 (1.93763e-06)	1.47091
7	29.5018 (2.42944e-07)	1.47237
8	29.5164 (3.03455e-08)	1.47311

Res	$-F_{sca,x}$ (conv.)	$-F_{sca,y}$ (conv.)
4	1.25044 (0.00034)	1.14162e-06 (0.00362)
5	0.62668 (2.44055e-05)	8.40309e-07 (0.00017)
6	0.31395 (2.85324e-06)	7.43893e-07 (0.00022)
7	0.15717 (3.5657e-07)	8.62613e-07 (2.15323e-05)
8	0.07864 (4.45181e-08)	8.29497e-07 (3.9682e-06)

Res	$-F_{sca,z}$ (conv.)
4	21.8122 (0.00104)
5	21.8657 (9.34724e-06)
6	21.8652 (2.0855e-08)
7	21.8652 (1e-09)
8	21.8652 (1e-09)

Table C.51: Integrated DDA

C.2.17 m = 1.81 + 0.48i
x = 5.03617

Quantity	Mie-value
Q_{ext}	2.58971
Q_{sca}	1.24205
g_z	0.841157
Q_{pr}	1.54496

Table C.52: Mie-values

	Cross-section	Efficiency
Extinction	208.387	2.61529
Absorption	108.91	1.36683
Scattering	99.4775	1.24846

Table C.53: Direct DDA

Res	C_{sca} (conv.)	Q_{sca}
4	100.834 (0.00103)	1.26548
5	99.0799 (6.95983e-05)	1.24347
6	99.3129 (2.29437e-06)	1.24639
7	99.3949 (2.0133e-07)	1.24742
8	99.4361 (2.5292e-08)	1.24794

Res	$-F_{sca,x}$ (conv.)	$-F_{sca,y}$ (conv.)
4	3.0379 (0.00297)	8.16726e-07 (0.00472)
5	1.56034 (0.00012)	3.98198e-07 (0.0035)
6	0.78547 (7.54184e-06)	8.64815e-08 (0.00074)
7	0.3942 (9.6307e-07)	-2.92383e-07 (0.00015)
8	0.19748 (1.20108e-07)	-1.77086e-07 (1.58335e-05)

Res	$-F_{sca,z}$ (conv.)
4	86.5772 (0.00155)
5	84.1272 (0.00011)
6	84.209 (9.48517e-07)
7	84.2083 (1.84809e-09)
8	84.2083 (1e-09)

Table C.54: Integrated DDA

C.2.18 m = 1.81 + 0.48i
x = 10.056

Quantity	Mie-value
Q_{ext}	2.39239
Q_{sca}	1.24785
g_z	0.877034
Q_{pr}	1.29798

Table C.55: Mie-values

	Cross-section	Efficiency
Extinction	762.668	2.4007
Absorption	366.298	1.15302
Scattering	396.37	1.24768

Table C.56: Direct DDA

Res	C_{sca} (conv.)	Q_{sca}
4	405.574 (0.01233)	1.27665
5	399.507 (5.68715e-05)	1.25755
6	395.624 (9.63558e-06)	1.24533
7	396.073 (2.77405e-07)	1.24675
8	396.222 (2.28281e-08)	1.24721

Res	$-F_{sca,x}$ (conv.)	$-F_{sca,y}$ (conv.)
4	10.862 (0.00726)	4.53917e-06 (0.03386)
5	4.72345 (0.00056)	-2.12709e-07 (0.03944)
6	2.40295 (1.76921e-05)	-2.04671e-07 (0.00148)
7	1.20556 (8.87077e-07)	-7.80734e-07 (0.00022)
8	0.60389 (1.1569e-07)	-3.41398e-07 (3.79167e-05)

Res	$-F_{sca,z}$ (conv.)
4	359.015 (0.01365)
5	353.57 (6.04061e-05)
6	348.86 (1.31842e-05)
7	349.018 (1.10907e-07)
8	349.017 (1e-09)

Table C.57: Integrated DDA

C.2.19 m = 2.5 + 1.4i
x = 2.50977

Quantity	Mie-value
Q_{ext}	2.90351
Q_{sca}	1.523
g_z	0.629343
Q_{pr}	1.94502

Table C.58: Mie-values

	Cross-section	Efficiency
Extinction	60.0031	3.03218
Absorption	29.4528	1.48836
Scattering	30.5503	1.54382

Table C.59: Direct DDA

Res	C_{sca} (conv.)	Q_{sca}
4	30.0987 (0.00043)	1.521
5	30.3529 (3.17659e-05)	1.53385
6	30.4514 (3.16121e-06)	1.53883
7	30.5008 (3.95691e-07)	1.54132
8	30.5255 (4.94097e-08)	1.54257

Res	$-F_{sca,x}$ (conv.)	$-F_{sca,y}$ (conv.)
4	1.45392 (0.00045)	1.211e-06 (0.00318)
5	0.73259 (4.51901e-05)	9.19595e-07 (8.24679e-05)
6	0.36796 (5.36511e-06)	7.79416e-07 (3.72099e-06)
7	0.18444 (6.68877e-07)	8.37289e-07 (6.7231e-07)
8	0.09234 (8.34745e-08)	8.55396e-07 (9.71756e-07)

Res	$-F_{sca,z}$ (conv.)
4	20.0756 (0.0012)
5	20.1337 (1.09469e-05)
6	20.1332 (2.38344e-08)
7	20.1332 (1e-09)
8	20.1332 (1e-09)

Table C.60: Integrated DDA

C.2.20 m = 2.5 + 1.4i
x = 5.02511

Quantity	Mie-value
Q_{ext}	2.6371
Q_{sca}	1.5076
g_z	0.731954
Q_{pr}	1.53361

Table C.61: Mie-values

	Cross-section	Efficiency
Extinction	212.58	2.67967
Absorption	93.3199	1.17634
Scattering	119.26	1.50333

Table C.62: Direct DDA

Res	C_{sca} (conv.)	Q_{sca}
4	119.985 (0.00088)	1.51246
5	118.515 (4.93093e-05)	1.49394
6	118.924 (3.36429e-06)	1.4991
7	119.092 (3.43185e-07)	1.50121
8	119.176 (4.29714e-08)	1.50227

Res	$-F_{sca,x}$ (conv.)	$-F_{sca,y}$ (conv.)
4	4.40775 (0.00205)	8.76254e-07 (0.00471)
5	2.26902 (0.00013)	-6.30351e-07 (0.00331)
6	1.1452 (1.0068e-05)	-1.06153e-07 (0.00278)
7	0.57545 (1.26999e-06)	-3.35503e-07 (0.00011)
8	0.28846 (1.5827e-07)	-1.9099e-07 (2.52723e-05)

Res	$-F_{sca,z}$ (conv.)
4	91.3955 (0.00154)
5	88.7973 (0.00012)
6	88.8863 (9.80852e-07)
7	88.8856 (1.96488e-09)
8	88.8856 (1e-09)

Table C.63: Integrated DDA

C.2.21 m = 2.5 + 1.4i
x = 10.0542

Quantity	Mie-value
Q_{ext}	2.43333
Q_{sca}	1.46995
g_z	0.766244
Q_{pr}	1.30699

Table C.64: Mie-values

	Cross-section	Efficiency
Extinction	776.231	2.44425
Absorption	314.427	0.99009
Scattering	461.805	1.45416

Table C.65: Direct DDA

Res	C_{sca} (conv.)	Q_{sca}
4	465.149 (0.0109)	1.46469
5	463.615 (1.24455e-05)	1.45986
6	460.165 (7.32886e-06)	1.449
7	461.065 (4.76357e-07)	1.45183
8	461.431 (4.84642e-08)	1.45299

Res	$-F_{sca,x}$ (conv.)	$-F_{sca,y}$ (conv.)
4	15.8539 (0.00555)	-5.18443e-06 (0.00034)
5	7.26463 (0.00034)	-7.34697e-06 (0.00025)
6	3.69614 (1.7803e-05)	-8.2178e-06 (1.92731e-05)
7	1.85763 (1.31623e-06)	-9.41714e-06 (1.28402e-05)
8	0.93131 (1.67507e-07)	-9.49512e-06 (2.57578e-06)

Res	$-F_{sca,z}$ (conv.)
4	366.585 (0.01348)
5	363.106 (3.76633e-05)
6	358.008 (1.39121e-05)
7	358.179 (1.16791e-07)
8	358.178 (1e-09)

Table C.66: Integrated DDA

C.2.22 m = 3.05 + 0.33i
x = 2.51808

Quantity	Mie-value
Q_{ext}	2.96033
Q_{sca}	1.62098
g_z	0.661626
Q_{pr}	1.88785

Table C.67: Mie-values

	Cross-section	Efficiency
Extinction	61.3713	3.08088
Absorption	28.4049	1.42594
Scattering	32.9664	1.65494

Table C.68: Direct DDA

Res	C_{sca} (conv.)	Q_{sca}
4	32.6305 (0.00037)	1.63807
5	32.8219 (2.21372e-05)	1.64768
6	32.8939 (2.13979e-06)	1.6513
7	32.9301 (2.68068e-07)	1.65311
8	32.9482 (3.34868e-08)	1.65402

Res	$-F_{sca,x}$ (conv.)	$-F_{sca,y}$ (conv.)
4	1.51576 (0.0002)	6.04848e-07 (0.00312)
5	0.75902 (2.11736e-05)	1.91759e-07 (0.00244)
6	0.38001 (2.2455e-06)	2.286e-07 (8.01217e-05)
7	0.19018 (2.81749e-07)	3.18726e-07 (7.80373e-05)
8	0.09514 (3.51995)	3.14334e-07 (5.93582e-06)

Res	$-F_{sca,z}$ (conv.)
4	22.9817 (0.00092)
5	23.0299 (8.04735e-06)
6	23.0296 (1.58757e-08)
7	23.0296 (1e-09)
8	23.0296 (1e-09)

Table C.69: Integrated DDA

C.2.23 m = 3.05 + 0.33i
x = 5.02798

Quantity	Mie-value
Q_{ext}	2.54196
Q_{sca}	1.4047
g_z	0.740107
Q_{pr}	1.50233

Table C.70: Mie-values

	Cross-section	Efficiency
Extinction	205.253	2.58436
Absorption	93.0056	1.17104
Scattering	112.248	1.41332

Table C.71: Direct DDA

Res	C_{sca} (conv.)	Q_{sca}
4	112.84 (0.00083)	1.4207
5	111.531 (4.67011e-05)	1.40429
6	111.923 (3.42667e-06)	1.40923
7	112.085 (3.52944e-07)	1.41127
8	112.166 (4.41919e-08)	1.41229

Res	$-F_{sca,x}$ (conv.)	$-F_{sca,y}$ (conv.)
4	3.88531 (0.00119)	2.09538e-06 (0.00016)
5	1.99714 (0.00012)	1.51476e-06 (0.00115)
6	1.00905 (1.10929e-05)	1.81699e-06 (7.68474e-05)
7	0.50729 (1.38803e-06)	1.62076e-06 (3.96822e-06)
8	0.25435 (1.72927e-07)	1.46507e-06 (4.06829e-06)

Res	$-F_{sca,z}$ (conv.)
4	86.3769 (0.00149)
5	83.9724 (0.00011)
6	84.0549 (9.5635e-07)
7	84.0542 (1.88975e-09)
8	84.0542 (1e-09)

Table C.72: Integrated DDA

Appendix D

Graphs : aggregate particles

D.1 Scale-factor=1

D.2 Scale-factor=0.5

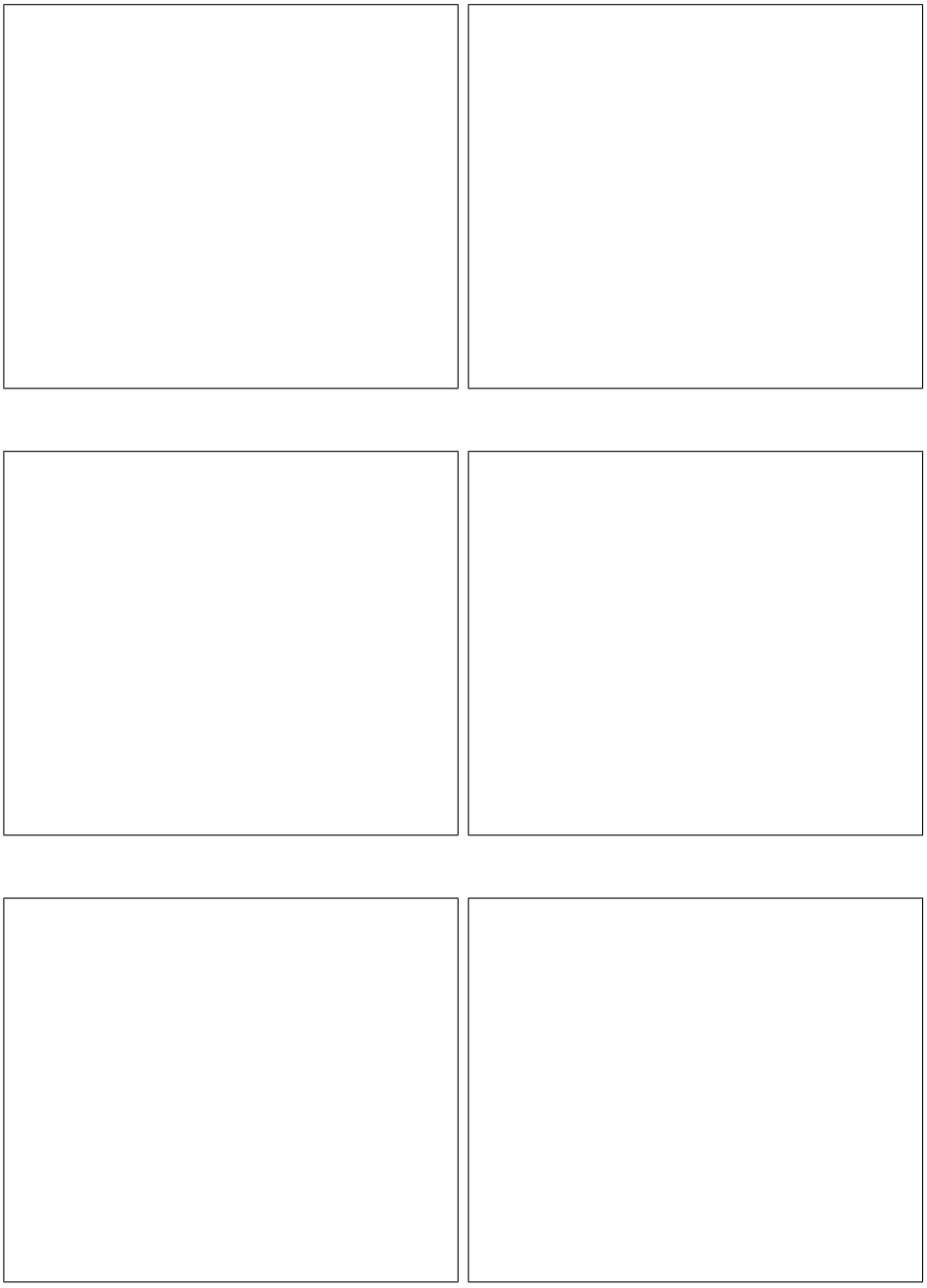

D.3 Scale-factor=0.25

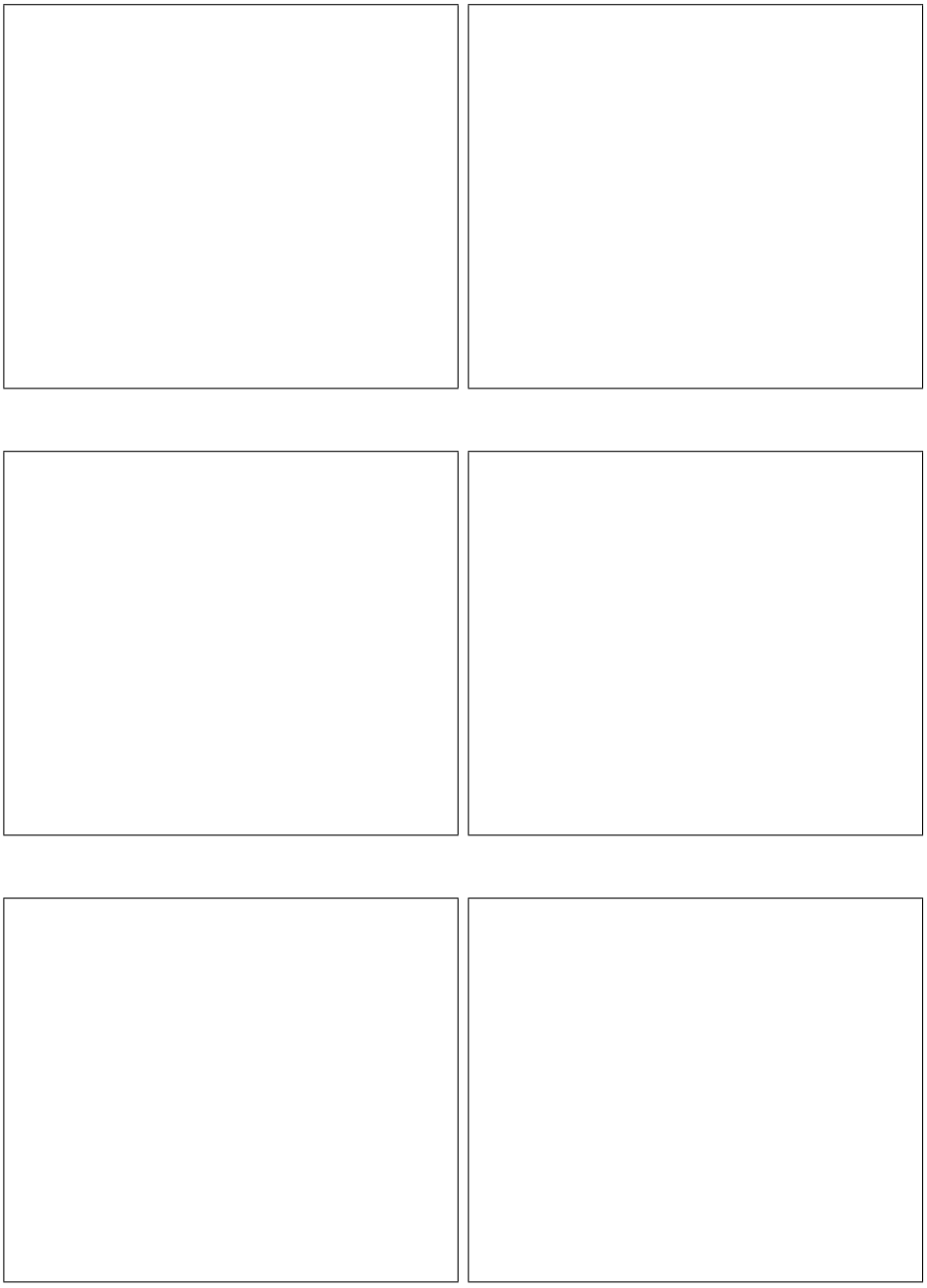

Appendix E

Tables : aggregate particles

In each section of this appendix the values of

- extinction cross section C_{ext},
- absorption cross section C_{abs},
- integrated scattering cross section $C_{sca,i}$, integrated to various levels of accuracy ($Res = 4, 5, 6, 7, 8$),
- integrated scattering force $\vec{F}_{sca,i}$, idem $C_{sca,i}$,
- direct scattering cross section $C_{sca,d} = C_{ext} - C_{abs}$ (listed with the integrated scattering cross section as $Res = 0$),
- direct scattering force $\vec{F}_{sca,d}$, idem $C_{sca,d}$,

are tabulated for one simulation, together with the list of residue-norms. The fraction $\frac{\#dip}{\lambda}$ printed below the table should be divided by $Re(m)$ to obtain D_λ. The entry `epsilon-b` at beginning of each of these lists, is the convergence-criterium. In the cases where this convergence-criterium is not met, only the list of residue-norms is printed. The convergence lists of simulations that did not converge, have been reduced by removing all entries, accept the first for each decade, the smallest of the entire list, and the last one before breaking the iteration procedure.

E.1 Scale-factor=1

E.1.1 m=1.14+0.38i aggregate 1

C_{ext}	1.61788e-09
C_{abs}	1.58645e-09

Res	C_{sca}	$g_x C_{sca}$	$g_y C_{sca}$	$g_z C_{sca}$
Direct	3.143e-11	-4.97346e-12	-1.18572e-12	4.93266e-11
4	6.97495e-11	-1.83191e-12	-1.11682e-12	4.91268e-11
5	6.96956e-11	-3.12986e-12	-1.20939e-12	4.90062e-11
6	7.01021e-11	-4.06325e-12	-1.19549e-12	4.91739e-11
7	7.02865e-11	-4.5165e-12	-1.19056e-12	4.92502e-11
8	7.03796e-11	-4.74459e-12	-1.18814e-12	4.92884e-11

Table E.1: $\frac{\#dip}{\lambda} = 3.67$, Y-polarized, scale-factor=1

```
epsilon*b = 5.0999999344e-11
r0        = 1.3989786648e+00
r01       = 2.5345050e-02
r02       = 3.539146326430e-04
r03       = 5.950194973757e-06
r04       = 9.490999942734e-08
r05       = 1.237968659334e-09
r06       = 2.258893617741e-11
```

E.1.2 m=1.7+0.03i aggregate 1

C_{ext}	2.74247e-10
C_{abs}	1.35098e-10

Res	C_{sca}	$g_x C_{sca}$	$g_y C_{sca}$	$g_z C_{sca}$
Direct	1.39149e-10	-1.65008e-11	-2.41869e-12	1.6831e-10
4	2.5674e-10	-3.57879e-12	-1.77075e-12	1.68057e-10
5	2.56029e-10	-9.15849e-12	-2.46121e-12	1.67755e-10
6	2.57189e-10	-1.28714e-11	-2.4199e-12	1.68039e-10
7	2.57701e-10	-1.46808e-11	-2.41942e-12	1.68175e-10
8	2.5796e-10	-1.55897e-11	-2.41906e-12	1.68242e-10

Table E.2: $\frac{\#dip}{\lambda} = 2.46$, Y-polarized, scale-factor=1

```
epsilon*b = 5.0999999344e-11
r0        = 3.1209305310e+00
r01       = 8.8256599e-01
r02       = 1.335122803221e-01
r03       = 3.096676099105e-02
r04       = 6.165507852188e-03
r05       = 1.249561194707e-03
r06       = 2.510717302584e-04
r07       = 5.984819602303e-05
r08       = 1.216753913280e-05
r09       = 1.899363928129e-06
r10       = 3.473279067347e-07
r11       = 5.308646503288e-08
r12       = 6.431987362399e-09
r13       = 1.046042918829e-09
r14       = 1.641644602493e-10
r15       = 2.114554148891e-11
```

E.1.3 m=1.14+0.38i aggregate 2

```
epsilon*b = 1.0099999893e-10
r0        = 1.6588472856e+00
r01       = 4.0541729e-02
r02       = 1.295207226715e-03
r03       = 1.109511213887e-04
r04       = 1.515907259518e-05
r05       = 3.151829491045e-06
r06       = 9.113787693000e-07
r07       = 3.322655459828e-07
r08       = 1.484807837816e-07
r09       = 7.761775169460e-08
r16       = 8.935475410193e-09
r26       = 5.534462621541e-09
r47       = 9.877107655772e-09
```

E.1.4 m=1.7+0.03i aggregate 2

```
epsilon*b = 1.0099999893e-10
r0        = 3.7006620609e+00
r01       = 6.5071597e-01
r02       = 1.021557692532e-01
r03       = 1.822531742284e-02
```

```
r04       = 3.226423829426e-03
r05       = 6.706763483086e-04
r06       = 1.310360938556e-04
r07       = 3.284151843767e-05
r08       = 9.279390475601e-06
r09       = 3.006387382112e-06
r10       = 1.160057730259e-06
r11       = 5.173424750184e-07
r12       = 2.470090823658e-07
r13       = 1.208626996956e-07
r14       = 6.458613316005e-08
r18       = 7.184735885106e-09
r24       = 9.417046565950e-10
r62       = 1.316780300709e-10
r83       = 2.360200661663e-10
```

E.2 Scale-factor=0.5

E.2.1 m=1.14+0.38i aggregate 1

C_{ext}	1.4804e-09
C_{abs}	1.32834e-09

Res	C_{sca}	$g_x C_{sca}$	$g_y C_{sca}$	$g_z C_{sca}$
Direct	1.5206e-10	-1.02795e-12	2.0189e-12	1.06419e-10
4	1.48998e-10	9.65076e-12	2.18215e-12	1.0612e-10
5	1.50182e-10	4.35252e-12	1.97198e-12	1.06302e-10
6	1.50775e-10	1.67913e-12	2.00401e-12	1.0636e-10
7	1.51071e-10	3.29613e-13	2.01132e-12	1.0639e-10
8	1.51219e-10	-3.48113e-13	2.01511e-12	1.06404e-10

Table E.3: $\frac{\#dip}{\lambda} = 8.7$, Y-polarized, scale-factor=0.5

```
epsilon*b = 5.0999998212e-11
r0        = 1.9374739169e+00
r01       = 6.4570154e-02
r02       = 8.328533992574e-04
r03       = 1.099472017468e-05
r04       = 1.714494313344e-07
r05       = 3.266324228924e-09
r06       = 5.834538918178e-11
r07       = 6.999463729543e-13
```

E.2.2 m=1.7+0.03i aggregate 1

C_{ext}	6.7543e-10
C_{abs}	1.20593e-10

Res	C_{sca}	$g_x C_{sca}$	$g_y C_{sca}$	$g_z C_{sca}$
Direct	5.54837e-10	2.94406e-12	9.91752e-12	3.87606e-10
4	5.46619e-10	4.13592e-11	1.02133e-11	3.87735e-10
5	5.49977e-10	2.21982e-11	9.7509e-12	3.87743e-10
6	5.51639e-10	1.26352e-11	9.8562e-12	3.87674e-10
7	5.5246e-10	7.80447e-12	9.88646e-12	3.8764e-10
8	5.52867e-10	5.37816e-12	9.90195e-12	3.87623e-10

Table E.4: $\frac{\#dip}{\lambda} = 5.8$, Y-polarized, scale-factor=0.5

```
epsilon*b = 5.0999998212e-11
r0        = 4.3222399052e+00
r01       = 1.1835147e+00
r02       = 2.036420329269e-01
r03       = 4.562863170179e-02
r04       = 1.020680199621e-02
r05       = 2.172126182518e-03
r06       = 3.971544392488e-04
r07       = 7.610316946197e-05
r08       = 1.691313511831e-05
r09       = 2.811671513663e-06
r10       = 4.980304675147e-07
r11       = 9.263532967270e-08
r12       = 1.320085424477e-08
r13       = 2.153429053838e-09
r14       = 2.953411407300e-10
r15       = 3.656725060823e-11
```

E.2.3 m=1.14+0.38i aggregate 2

```
epsilon*b = 1.0099999911e-10
r0        = 2.9878565672e+00
r01       = 7.6831177e-02
r02       = 3.702837508207e-03
r03       = 2.801502607551e-04
r04       = 3.861994090414e-05
r05       = 7.315866097051e-06
r06       = 1.806378834812e-06
r07       = 5.619952018190e-07
r08       = 2.084745603525e-07
r09       = 8.948871791942e-08
r13       = 8.317286128134e-09
r21       = 8.899730347394e-10
r50       = 2.156824394982e-10
r71       = 2.526121702283e-10
```

E.2.4 m=1.7+0.03i aggregate 2

C_{ext}	1.10575e-09
C_{abs}	2.00306e-10

Res	C_{sca}	$g_x C_{sca}$	$g_y C_{sca}$	$g_z C_{sca}$
Direct	9.05444e-10	1.56501e-10	7.4594e-11	1.02723e-09
4	1.40567e-09	2.18242e-10	7.27434e-11	1.04871e-09
5	1.39364e-09	1.86974e-10	7.37448e-11	1.03921e-09
6	1.38629e-09	1.71788e-10	7.41605e-11	1.0332e-09
7	1.3826e-09	1.64158e-10	7.43774e-11	1.03022e-09
8	1.38074e-09	1.60333e-10	7.44857e-11	1.02872e-09

Table E.5: $\frac{\#dip}{\lambda} = 5.8$, Y-polarized, scale-factor=0.5

```
epsilon*b = 1.0099999911e-10
r0        = 6.6655006540e+00
r01       = 9.2107831e-01
r02       = 1.417535690650e-01
r03       = 2.368181899570e-02
r04       = 3.859185644004e-03
r05       = 7.614934051506e-04
r06       = 1.691984071170e-04
r07       = 4.109684568530e-05
r08       = 1.147915607035e-05
r09       = 3.608868280471e-06
r10       = 1.262424874060e-06
r11       = 4.684318028704e-07
r12       = 1.756921266605e-07
r13       = 6.918031067297e-08
r14       = 2.744993924933e-08
r15       = 1.087870686370e-08
r16       = 4.475661076032e-09
r17       = 1.918983209565e-09
r18       = 8.570631879541e-10
r19       = 4.056070121182e-10
r20       = 1.997588934693e-10
r21       = 1.035217468926e-10
r22       = 5.662904066792e-11
```

E.3 Scale-factor=0.25

E.3.1 m=1.14+0.38i aggregate 1

C_{ext}	1.38845e-09
C_{abs}	1.21547e-09

Res	C_{sca}	$g_x C_{sca}$	$g_y C_{sca}$	$g_z C_{sca}$
Direct	1.7298e-10	1.8396e-12	5.02819e-12	1.05345e-10
4	3.68437e-10	3.45393e-11	4.59948e-12	1.05038e-10
5	3.76214e-10	1.87898e-11	4.84884e-12	1.052e-10
6	3.80163e-10	1.04672e-11	4.93853e-12	1.05273e-10
7	3.82133e-10	6.19246e-12	4.98354e-12	1.05309e-10
8	3.83117e-10	4.02588e-12	5.00605e-12	1.05327e-10

Table E.6: $\frac{\#dip}{\lambda} = 17.4$, Y-polarized, scale-factor=0.25

```
epsilon*b = 5.1000000179e-11
r0        = 2.0311202805e+00
r01       = 6.2757357e-02
r02       = 6.186748000641e-04
r03       = 8.413555822644e-06
r04       = 1.494094150514e-07
r05       = 3.143997969574e-09
r06       = 4.211338076390e-11
```

E.3.2 m=1.7+0.03i aggregate 1

C_{ext}	6.66041e-10
C_{abs}	9.43095e-11

Res	C_{sca}	$g_x C_{sca}$	$g_y C_{sca}$	$g_z C_{sca}$
Direct	5.71732e-10	1.56204e-11	1.74117e-11	3.29356e-10
4	1.03531e-09	1.05843e-10	1.59193e-11	3.28523e-10
5	1.05599e-09	6.23703e-11	1.67944e-11	3.28957e-10
6	1.06646e-09	3.94195e-11	1.71019e-11	3.29157e-10
7	1.07168e-09	2.76286e-11	1.72568e-11	3.29257e-10
8	1.07428e-09	2.1652e-11	1.73342e-11	3.29306e-10

Table E.7: $\frac{\#dip}{\lambda} = 11.7$, Y-polarized, scale-factor=0.25

```
epsilon*b = 5.1000000179e-11
r0        = 4.5311515276e+00
r01       = 9.6943698e-01
r02       = 2.066140401764e-01
r03       = 4.488373397686e-02
r04       = 9.554615881839e-03
r05       = 2.106894547975e-03
r06       = 3.898128499342e-04
r07       = 7.706273718533e-05
r08       = 1.577852319098e-05
r09       = 2.634935817106e-06
r10       = 4.753922713029e-07
r11       = 9.260070120377e-08
r12       = 1.391540643731e-08
r13       = 2.156460280842e-09
r14       = 3.114401719425e-10
r15       = 3.657389779717e-11
```

E.3.3 m=1.14+0.38i aggregate 2

In this case the the stop-criterium was set to $\epsilon_0 = 10^{-24}$ instead of $\epsilon_0 = 10^{-12}$. In this case the convergence rate for Y- and X-polarization was slowing down, but for the Y-polarization $\epsilon_0 = 10^{-12}$ could just be reached while the X-polarization just could not, it started diverging just before $\epsilon_0 = 10^{-12}$. Instead of increasing ϵ_0 for the convergence of the X-polarization to be accepted, ϵ_0 was decreased in order to see when it would start to diverge. Based on the clearly divergent behavior for both polarizations, it was decided both were to be discarded.

```
epsilon*b = 1.0099999827e-22
r0        = 2.7676454618e+00
r01       = 6.9511520e-02
r02       = 4.763508654762e-03
r03       = 3.610146425035e-04
r04       = 4.609791269519e-05
r05       = 8.972398055627e-06
r06       = 2.174529100429e-06
r07       = 6.261421091410e-07
r08       = 2.156482136375e-07
r09       = 8.632447200459e-08
r13       = 5.761711234988e-09
r18       = 7.460370726365e-10
r28       = 9.266533682699e-11
```

```
r73        = 1.727052469354e-11
r94        = 1.902537065418e-11
```

E.3.4 m=1.7+0.03i aggregate 2

C_{ext}	7.43483e-10
C_{abs}	1.57168e-10

Res	C_{sca}	$g_x C_{sca}$	$g_y C_{sca}$	$g_z C_{sca}$
Direct	5.86315e-10	2.22736e-10	1.34996e-10	1.29158e-09
4	2.65799e-09	4.03766e-10	1.23579e-10	1.28826e-09
5	2.68357e-09	3.15397e-10	1.30353e-10	1.29023e-09
6	2.6948e-09	2.69885e-10	1.32657e-10	1.2909e-09
7	2.70017e-09	2.46516e-10	1.33828e-10	1.29124e-09
8	2.70279e-09	2.34678e-10	1.34412e-10	1.29141e-09

Table E.8: $\frac{\#dip}{\lambda} = 11.7$, Y-polarized, scale-factor=0.25

```
epsilon*b = 1.0099999827e-10
r0        = 6.1742393946e+00
r01       = 6.9470854e-01
r02       = 1.232153567486e-01
r03       = 2.242373906691e-02
r04       = 4.412929987473e-03
r05       = 1.082635345238e-03
r06       = 3.190131175188e-04
r07       = 1.067411406627e-04
r08       = 4.127924178637e-05
r09       = 1.760251322679e-05
r10       = 8.425251985480e-06
r14       = 9.918838888658e-07
r20       = 9.274586711757e-08
r27       = 7.574545999740e-09
r35       = 8.928030947031e-10
r47       = 9.271399680329e-11
```